

สำนักหอสมุดกลาง พระจอมเกล้าลาดกระบัง

ANALYSIS OF IONOSPHERIC THICKNESS PARAMETERS AND SATELLITE
DELAY PROFILES AT EQUATORIAL LATITUDE STATION,
CHUMPHON, THAILAND



E078449



เลขหมู่.....
เลขทะเบียน **078449**
รับเดือนปี **27 พ.ย. 2560**



A THESIS SUBMITTED IN PARTIAL FULFILLMENT
OF THE REQUIREMENT FOR THE DEGREE OF
DOCTOR OF ENGINEERING IN ELECTRICAL ENGINEERING
FACULTY OF ENGINEERING
KING MONGKUT'S INSTITUTE OF TECHNOLOGY LADKRABANG
2017
KMITL-2017-EN-D-018-087

This material is reserved for educational use only, not allowed for commercial use.

Forbidden to modify the content, and cite the document when use.



COPYRIGHT 2017

FACULTY OF ENGINEERING

KING MONGKUT'S INSTITUTE OF TECHNOLOGY LADKRABANG

This material is reserved for educational use only, not allowed for commercial use.

Forbidden to modify the content, and cite the document when use.

หัวข้อวิทยานิพนธ์	การวิเคราะห์พารามิเตอร์ความหนาของชั้นไอโอโนสเฟียร์และ โพรไฟล์เวลาประวิงของสัญญาณดาวเทียมที่สถานีละติจูด แนวเส้นศูนย์สูตร จังหวัดชุมพร ประเทศไทย
นักศึกษา	นายบุญยวีร์ จามจรกุลกาญจน์
รหัสประจำตัว	57601020
ปริญญา	วิศวกรรมศาสตรดุษฎีบัณฑิต
สาขาวิชา	วิศวกรรมไฟฟ้า
พ.ศ.	2560
อาจารย์ที่ปรึกษาวิทยานิพนธ์	ศาสตราจารย์ ดร. พรชัย ทรัพย์นิธิ

บทคัดย่อ

พารามิเตอร์ความหนาของชั้นไอโอโนสเฟียร์ถูกใช้เพื่อศึกษาและหาค่าปริมาณความหนาแน่นอิเล็กตรอนและปริมาณอิเล็กตรอนสุทธิ ส่วนเวลาประวิงในชั้นไอโอโนสเฟียร์ของสัญญาณดาวเทียมก็เป็นค่าที่ทำได้จากปริมาณอิเล็กตรอนสุทธิ แล้วนำไปปรับแก้ตำแหน่งของเครื่องรับ เนื่องจากเครื่องไอโอโนซอนเด FMCW ที่สถานีละติจูดในแนวเส้นศูนย์สูตร จังหวัดชุมพร ประเทศไทย (10.72°E, 99.37°W) ไม่มีพารามิเตอร์ความหนาและแบบรูปความหนาแน่นอิเล็กตรอนของชั้นไอโอโนสเฟียร์ด้านบนและด้านล่าง ดังนั้น วิทยานิพนธ์ฉบับนี้จึงนำเสนอสมการใหม่ที่ใช้ในการหาค่าพารามิเตอร์ความหนาด้านล่างของชั้นไอโอโนสเฟียร์โดยอาศัยพารามิเตอร์ของเครื่องไอโอโนซอนเด FMCW ค่าปริมาณอิเล็กตรอนสุทธิจากเครื่องรับ GPS สองความถี่และสมการของแบบจำลอง NeQuick 2 การเปลี่ยนแปลงรายวันของค่าพารามิเตอร์ความหนาด้านล่างที่นำเสนอใหม่ (B2bot_Pro) ได้ถูกนำไปเปรียบเทียบกับค่าเดิมของ NeQuick 2 (B2bot_NeQ) ค่า B0 ที่ได้จากแบบจำลอง IRI-2012 และค่า B0 ที่วัดได้จากเครื่องดิจิซอนเด ค่าผลต่างสัมบูรณ์เชิงสถิติ ได้แก่ ค่าเฉลี่ย ค่าต่ำสุดและค่าสูงสุด ก็ถูกหาค่าและวิเคราะห์ที่วิทยานิพนธ์ฉบับนี้ด้วย นอกจากนี้ โพรไฟล์ความหนาแน่นอิเล็กตรอนของชั้นไอโอโนสเฟียร์ด้านบนก็ได้ถูกศึกษาเสมือนเป็นการประยุกต์ใช้งานพารามิเตอร์ความหนาด้านล่าง โพรไฟล์เวลาประวิงของสัญญาณดาวเทียมก็ถูกนำเสนอด้วยเช่นกันเสมือนเป็นการประยุกต์ใช้งานค่า TEC สำหรับการปรับแก้ตำแหน่งของเครื่องรับในอนาคต ผลจากการศึกษา พบว่า โดยทั่วไป การเปลี่ยนแปลงรายวันของพารามิเตอร์ความหนาด้านล่างใหม่ที่นำเสนอมีแนวโน้มที่คล้ายกับค่า B0 ที่วัดได้จากเครื่องดิจิซอนเดเมื่อเปรียบเทียบกับค่าอื่น ส่วนโพรไฟล์ความหนาแน่นอิเล็กตรอนด้านบนที่ได้จาก NeQuick ที่สถานีชุมพรมีความคล้ายคลึงกับโพรไฟล์ความหนาแน่นอิเล็กตรอนด้านบนที่ได้จากตัวเลือก IRI01-corr ในฤดูหนาวและตัวเลือก NeQuick ในฤดูอควินอกซ์และฤดูร้อน นอกจากนี้ ค่าเวลาประวิงในชั้นไอโอโนสเฟียร์ที่สังเกตได้ในฤดูหนาวและฤดูอควินอกซ์มีค่าที่ใกล้เคียงกับค่า IGS TECs ในตอนกลางวันและค่า IRI TECs ในตอนกลางคืน

This material is reserved for educational use only, not allowed for commercial use.

Thesis Title	Analysis of ionospheric thickness parameters and satellite delay profiles at equatorial latitude station, Chumphon, Thailand
Student	Mr. Punyawit Jamjareegulgarn
Student ID.	57601020
Degree	Doctor of Engineering
Program	Electrical Engineering
Year	2017
Thesis Advisor	Prof. Dr. Pornchai Supnithi

ABSTRACT

Ionospheric thickness parameter is used for studying and computing the electron density and the total electron content (TEC). Meanwhile, satellite delay is obtained from the TECs so as to be used for correcting the receiver position. Since the thickness parameters and electron density profiles for bottomside and topside ionospheres are not available on FMCW ionosonde at equatorial latitude station, Chumphon, Thailand (10.72°E, 99.37°W), hence, this thesis proposes a new expression for computing the bottomside thickness parameter based on the FMCW ionosonde parameters, TECs of dual-frequency GPS receiver, and some expressions of NeQuick 2 model. The diurnal variations of a new proposed bottomside thickness parameter (B2bot_Pro) are then compared with those of an original NeQuick B2bot (B2bot_NeQ), the IRI-2012 B0 values, and the observed B0. The statistical absolute differences, including averages, minima and maxima, are also determined and analyzed in this thesis. Moreover, the electron density profile of topside ionosphere is also studied as an application of the bottomside thickness parameter. Satellite delay profile is also presented as an application of the TECs for correcting the receiver position. The results show that the diurnal variations of the B2bot_Pro generally show the same trends as those of the observed B0 from digisonde, compared with other parameters. NeQuick-derived topside EDPs at Chumphon are generally closer to those of IRI01-corr in the winter and those of NeQuick in the equinox and summer. The observed ionospheric delays are only close to the IGS TECs during daytime and the IRI TECs during nighttime in the winter and equinox.

This material is reserved for educational use only, not allowed for commercial use.

ACKNOWLEDGEMENTS

I would like to express my deepest gratitude to my supervisor, Prof. Dr. Pornchai Supnithi, for suggesting me into the field of ionospheric research and supporting me several issues during my doctoral study, especially his instructive guidance.

Also, I am very grateful to Space Environment Laboratory, National Institute of Information and Communications Technology (NICT), Japan, for essential equipment, technical support and data, NeQuick 2 model (<http://t-ict4d.ictp.it/nequick2/nequick-2-web-model>) for the electron density and the TEC values, the IRI-2012 model (http://omniweb.gsfc.nasa.gov/vitmo/iri2012_vitmo.html) for giving a lot of ionospheric parameters, and Global Ionospheric Radio Observatory or GIRO (<http://giro.uml.edu>) for providing the digisonde data.

Moreover, I would also like to thank to Prof. Dr. Man-Lian Zhang, Prof. Dr. Dieter Bilitza, Asst. Prof. Dr. Prasert Kenpankho, and Asst. Prof. Somjai Klin-Ngam for giving a number of useful knowledge and suggestion.

Furthermore, I would also like to thank all the members of Communication, Signal Processing and Storage Research Group (CSSRG) Laboratory for their technical discussions, friendships, activities, and socializations during my study period, especially 3 members (Jumpon Udomchaibanjerd, Athiwat Chiablaem, and Jirapoom Budtho) who help and advise me about MATLAB programming. This research is financially supported by King Mongkut's Institute of Technology Ladkrabang Research fund under grant no. KREF 045906.

Finally, I would also like to thank my parents, Kimseng Jamjareekul and Bak-Aeng Sae-Lee, my wife (Usa Lheegarnjana), my daughter (Siragarn Jamjareegulgarn) and every members in my family for supporting, helping and encouraging me all the times.

Punyawi Jamjareegulgarn

TABLE OF CONTENTS

	Page
Abstract (Thai).....	I
Abstract (English).....	II
Acknowledgements.....	III
Table of Contents.....	IV
List of Tables.....	VI
List of Figures.....	VIII
Chapter 1 INTRODUCTION.....	1
1.1 Background and motivation.....	1
1.2 Objectives of thesis.....	5
1.3 Scope of thesis.....	6
1.4 Benefits of thesis.....	7
1.5 Contributions of thesis.....	7
1.6 Thesis outline.....	8
Chapter 2 IONOSPHERE FEATURES AND MODELS.....	9
2.1 Vertical structure of ionosphere.....	9
2.2 Ionospheric variations.....	12
2.2.1 Diurnal variation.....	13
2.2.2 Seasonal variation.....	13
2.2.3 Latitudinal variation.....	13
2.3 FMCW ionosonde.....	17
2.4 Ionogram and ionosonde parameters.....	20
2.5 International Reference Ionosphere (IRI) model.....	22
2.6 NeQuick 2 model.....	26
2.7 Chumphon station.....	29
Chapter 3 GPS SYSTEM.....	33
3.1 Principles of GPS.....	33
3.1.1 Background of GPS system.....	33
3.1.2 Structure of GPS code.....	39
3.2 GPS receiver and RINEX format.....	41
3.2.1 GPS receiver.....	41
3.2.2 RINEX format.....	42

TABLE OF CONTENTS (cont.)

	Page
3.3 Computations of TEC and slab thickness.....	43
3.3.1 Ionosphere delay computation.....	43
3.3.2 TEC computation.....	46
3.3.3 Slab thickness computation.....	50
 Chapter 4 COMPUTATIONS OF BOTTOMSIDE THICKNESS.....	 54
4.1 Original bottomside thickness of NeQuick 2 model.....	54
4.2 New proposed bottomside thickness of NeQuick 2 model.....	55
4.3 Bottomside thickness of IRI model.....	58
4.4 Comparison results of the B2bot_Pro.....	59
4.4.1 Comparisons between the B2bot_Pro and the B2bot_NeQ.....	59
4.4.2 Comparisons between the B2bot_Pro and the B0_ABT.....	64
4.4.3 Comparisons between the B2bot_Pro and the B0_Bil.....	66
4.4.4 Comparisons between the B2bot_Pro and the B0_obs.....	70
4.5 Physical explanations and discussions.....	73
 Chapter 5 BOTTOMSIDE THICKNESS FOR TOPSIDE IONOSPHERE.....	 77
5.1 NeQuick topside formulation.....	77
5.2 IRI-2012 model with topside density option.....	80
5.3 Comparison results of topside EDPs and topside TECs.....	81
5.4 Comparison results of topside TEC values.....	87
5.5 Comparison results between IGS TECs and topside TECs.....	90
 Chapter 6 SATELLITE DELAY PROFILES.....	 93
6.1 Comparison results of TECs.....	94
6.2 Comparison results of ionospheric delays.....	96
 Chapter 7 CONCLUSIONS.....	 99
7.1 Summary.....	99
7.2 Suggestions for future works.....	103
 List of References.....	 104
Appendices.....	112
Appendix A List of Publications.....	113
Author Biography.....	114

This material is reserved for educational use only, not allowed for commercial use.

LIST OF TABLES

Table	Page
2.1 Operating parameters of a FMCW Ionosonde.....	18
3.1 GPS frequencies and code usages.....	40
4.1 Transition points, local times, and heights of diurnal variations of the B2bot_Pro and B2bot_NeQ during the equinoxes from 2004 to 2006.....	60
4.2 Transition points, local times, and heights of diurnal variations of the B2bot_Pro and B2bot_NeQ during the summers from 2004 to 2006.....	62
4.3 Transition points, local times, and heights of diurnal variations of the B2bot_Pro and B2bot_NeQ during the winters from 2004 to 2006.....	62
4.4 Averaged PD_B2bot during daytime and nighttime from 2004 to 2006.....	62
4.5 Minima and Maxima in PD_B2bot during daytime from 2004-2006.....	62
4.6 Minima and Maxima in PD_B2bot during nighttime from 2004-2006.....	64
4.7 Transition points, local times and heights of diurnal variations of the B0_ABT from 2004 to 2006.....	65
4.8 Averaged PD_B2B0ABT during daytime and nighttime from 2004 to 2006.....	66
4.9 Minima and Maxima in PD_B2B0ABT during daytime from 2004-2006.....	66
4.10 Minima and Maxima in PD_B2B0ABT during nighttime from 2004-2006.....	66
4.11 Averaged PD_B2B0Bil during daytime and nighttime from 2004 to 2006.....	69
4.12 Minima and Maxima in PD_B2B0Bil during daytime from 2004-2006.....	69
4.13 Minima and Maxima in PD_B2B0Bil during nighttime from 2004-2006.....	69
5.1 The results of IAD_IRI values at different local times on January 15th, 2007.....	86
5.2 The results of IAD_IRI values at different local times on March 21st, 2007.....	86
5.3 The results of IAD_IRI values at different local times on June 21st, 2007.....	87
5.4 Topside TEC and AD_NeQ values on January 15th, 2007.....	89
5.5 Topside TEC and AD_NeQ values on March 21st, 2007.....	90
5.6 Topside TEC and AD_NeQ values on June 21st, 2007.....	90
5.7 IGS TEC, some topside TEC, and D _t T values on January 15th, 2007.....	92
5.8 IGS TEC, some topside TEC, and D _t T values on March 21st, 2007.....	92
5.9 IGS TEC, some topside TEC, and D _t T values on June 21st, 2007.....	92

This material is reserved for educational use only, not allowed for commercial use.

LIST OF TABLES (cont.)

Table	Page
6.1 Minima and Maxima of TEC values in winter season, 2015.....	94
6.2 Minima and Maxima of TEC values in equinox season, 2015.....	96
6.3 Minima and Maxima of TEC values in summer season, 2015.....	96
6.4 Minima and Maxima of ionospheric delays in winter season, 2015.....	98
6.5 Minima and Maxima of ionospheric delays in equinox season, 2015.....	98
6.6 Minima and Maxima of ionospheric delays in summer season, 2015.....	98



LIST OF FIGURES

Figure	Page
2.1 The structure of neutral (left panel) and ionized (right panel) atmosphere.....	10
2.2 Geomagnetic latitudes and geographic latitudes	14
2.3 (a) Equatorial Ionization Anomaly (EIA) (b) the variations of electron density values and electric fields.....	15
2.4 Block diagram of a FMCW ionosonde system.....	17
2.5 Ionospheric observation with a FMCW ionosonde.....	18
2.6 Global map of digisonde locations.....	19
2.7 A graphical illustration of Ionogram with ionospheric parameters.....	19
2.8 An example of setting model inputs on a web page of the IRI-2012 model....	24
2.9 An example of setting optional inputs on a web page of the IRI-2012 model.	25
2.10 A result of the IRI-2012 model after submitting the model inputs.....	25
2.11 An example of selecting the studied parameters of the IRI-2012 model.....	26
2.12 An example of inserting the model inputs into the NeQuick 2 model.....	28
2.13 A result of the NeQuick 2 model after submitting the model inputs.....	29
2.14 The equipment implemented at Chumphon station.....	30
3.1 Three segments of GPS system.....	34
3.2 GPS Constellation including GPS satellites and 6 orbital planes.....	35
3.3 An idea for finding the user position in one dimensional representation.....	37
3.4 Two dimensional trilateration for finding the user position on the Earth.....	37
3.5 Computing one unknown position with the use of three known positions.....	38
3.6 Block diagram of a JAVAD GPS receiver used at Chumphon station.....	42
3.7 STEC to VTEC conversion at Ionospheric Pierce Point (IPP).....	48
3.8 The diurnal variations in IRI TEC values at Chumphon station in 2016.....	49
3.9 The yearly variations in IRI TEC values at Chumphon station in each day from 2004 to 2016.....	50
3.10 Equivalent slab thickness and its relations to B0 as well as H0.....	51

LIST OF FIGURES

Figure	Page
3.11 Diurnal variations of the slab thickness during three seasons from 2004-2006.	52
4.1 Diurnal variations of the B2bot_Pro and the B2bot_NeQ as well as the percentage deviations (in %) between three seasons from 2004 to 2006.....	61
4.2 Diurnal variations of the B2bot_Pro and the B0_AB T as well as the percentage deviations (in %) during three seasons from 2004 to 2006.....	63
4.3 Diurnal variations of the B2bot_Pro and the B0_Bil as well as the percentage deviations (in %) during three seasons from 2004 to 2006.....	67
4.4 Diurnal variations of the B0_AB T, the B2bot_Pro_obs and the B0_obs at Kwajalein station on March 20th 2006.....	71
4.5 Diurnal variations of the B0_AB T, the B2bot_Pro_obs and the B0_obs at Jicamarca station on March 20th, 2006.....	72
5.1 Topside Electron density profiles at different local times on January 15th, 2007.....	82
5.2 Topside Electron density profiles at different local times on March 21st, 2007.....	83
5.3 Topside Electron density profiles at different local times on June 21st, 2007.....	84
6.1 Vertical TECs and their absolute differences during three seasons.....	95
6.2 Ionospheric delays and their absolute differences for winter, equinox, and summer 2015.....	97

CHAPTER 1

INTRODUCTION

1.1 Background and motivation

The ionosphere is a layer of the Earth's atmosphere that is ionized by cosmic and solar radiations. It lies from 50 km to 1,000 km above the Earth's surface. The sun is a main cause of ionization in ionosphere which is called as photoionization process. Therefore, there are a lot of ions and free electrons in ionosphere which not only benefit surface waves resulting in longer distance communication, but also refract satellite signals leading to ionospheric delays. The variations in electron density and total electron content (TEC) values in ionosphere always are investigated, analyzed, and predicted so as to know the ionospheric characteristics, to propose the exact TEC model, and to correct the desired position coordinates. Several equipment have been invented to study several ionospheric parameters and to monitor space weather, for example, FMCW (frequency modulated-continuous wave) ionosonde, digisonde, incoherent scattering radar (ISR), and FORMOSAT-3/COSMIC satellite, etc. A peak height of F2 layer ($hmF2$) is a height where the peak electron density in F2 layer takes place and is used to divide the ionosphere into 2 parts, i.e., bottomside ionosphere and topside ionosphere. Bottomside ionosphere ranges from Earth's surface to the $hmF2$ whereas topside ionosphere ranges from the $hmF2$ to 1,500 km. Three main parameters studied in this thesis include bottomside thickness parameter, topside thickness parameter, and ionospheric delays. The benefits of these thickness parameters are to investigate electron density, TEC, and electron density profiles (EDPs) in bottomside and topside ionospheres, respectively. Meanwhile, TEC values are also used to compute ionospheric delays which are used subsequently to correct the receiver positions for GPS-based navigation systems. Moreover, the bottomside thickness parameter can also be used to compute the vertical TEC using the analytical expressions of NeQuick 2 model.

This material is reserved for educational use only, not allowed for commercial use.

Forbidden to modify the content, and cite the document when use.

The bottomside thickness parameter is an important parameter for ionospheric observation because its measurements offer substantial information on the bottomside electron density profile, the neutral as well as ionospheric temperatures, the ionospheric composition, and the ionospheric dynamics (Adeniyi et al., 1998). Moreover, it is related to ionospheric slab thickness directly, since the slab thickness covers total electron content (TEC) inside both bottomside and topside of the ionosphere. There are two empirical models for ionosphere, i.e., International Reference Ionosphere (IRI) model and NeQuick 2 model. The IRI model is a well-known empirical model to describe any phenomena and parameters in ionosphere and plasmaphere which provides monthly average values of electron density, electron temperatures, ion temperatures, and ion compositions, etc. for given location and time (Bilitza, 2001). The committee on Space Research (COSPAR) and International Union of Radio Science (URSI) have developed and enhanced a series of IRI models. Several improvements have been made for the IRI-2012 model, the latest version of the IRI model such as the new models for the thickness parameter (B0), the shape parameter (B1), and the electron density, etc. in the bottomside ionosphere (Bilitza et al., 2014). The electron density profile of bottomside ionosphere is described using an analytical expression of the IRI model (Ramakrishnan and Rawer, 1972), i.e.,

$$Ne_{\text{bot_IRI}}(h) = NmF2 \times \frac{\exp(-x^{B1})}{\cosh(x)}, \quad (1.1)$$

where $Ne_{\text{bot_IRI}}(h)$ is the bottomside electron density at height h , $NmF2$ is the peak electron density in F2 layer (eV/m^3), $hmF2$ is the peak height of $NmF2$ (km), $\cosh(x)$ is the hyperbolic cosine function of the variable x in (1.2), B0 and B1 are the bottomside thickness and the shape parameters, and h is the varying height in ionosphere.

Here, a variable x is defined as

$$x = \frac{hmF2 - h}{B0}. \quad (1.2)$$

This material is reserved for educational use only, not allowed for commercial use.

Forbidden to modify the content, and cite the document when use.

The B_0 is defined to be the difference between the hmF_2 and the height where the bottomside electron density in (1.1) drops down to 24% of the NmF_2 (namely, $h_{0.24}$) and the x value in (1.2) is equal to 1 if F1 layer does not exist, or the F1 peak height (hmF_1) if F1 layer occurs.

The IRI-2012 model offers three options for bottomside thickness parameter. The first option is “Gul-1987” (Gulyaeva, 1987; 2007) which comprises a functional description of the observed correlation between the hmF_2 and the height whose bottomside electron density is at half of NmF_2 (namely, $h_{0.5}$) at middle latitude stations and the relationship is converted into a model for calculating her B_0 values. The second option is “Bil-2000” (Bilitza, 2001) which relies on a table of B_0 values retrieved from the ionogram inversion at equatorial, low, and middle latitude stations. The last option is “ABT-2009” (Altadill et al., 2009). They use a spherical harmonics analysis (SHA) and describe the B_0 and B_1 variations with respect to modified dip latitude, month, local time, and sunspot number. They reveal that their modelled B_0 values are more accurate than the B_0 values of Bil-2000 and Gul-1987 about 32% and about 40%, respectively, whereas their modelled B_1 values are improved by about 20% over the B_1 values of Bil-2000 and Gul-1987. Note that the Gul-1987 B_1 is equal to the Bil-2000 B_1 in the IRI-2012 model.

Historically, Pandey and Sethi (1996) compared the electron density values from incoherent scatter measurements with those from the IRI-95 model and revealed that the Gul-1987 B_0 overestimates the observed B_0 during daytime. Sethi and Mahajan (2002) disclosed that the observed B_0 in the summer are more similar to the Bil-2000 B_0 than those in the winter and the equinox. Zhang et al. (2008) also addressed that the diurnal variations in Gul-1987 B_0 are generally more similar to the observed B_0 than those in Bil-2000 B_0 . Moreover, several studies have investigated the variability in (B_0 , B_1) parameters, e.g., Adeniyi and Radicella (1998), Lei et al. (2004), Zhang et al. (2008), Chuo et al. (2010), Chuo (2012). Their studies indicated that the diurnal, seasonal, and solar activity variations in B_0 significantly depend on the location of ionospheric monitoring station, whereas those in B_1 change slightly with seasons. The lower B_0 occur during nighttime whereas the higher B_0 occur

This material is reserved for educational use only, not allowed for commercial use.

during daytime, particularly, during the summer. The B0 values have the highest diurnal peaks around local noontime, and sometimes have the secondary peaks during pre-sunrise. The B0 collapses can also be observed during sunrise. Jamjareegulgarn et al. (2015) reported that the secondary peaks can sometimes be found in the B0 with Gul-1987 and ABT-2009 options, except the B0 with Bil-2000 option.

Another ionospheric electron density model is the NeQuick model (Hochegger et al., 2000; Radicella and Leitinger, 2001) which is developed by Aeronomy and Radio propagation Laboratory of Abdus Salam International Centre for Theoretical Physics (ICTP), Trieste, Italy and the Institute for Geophysics, Astrophysics and Meteorology of University of Graz, Austria. The NeQuick model is an evolution of the analytical model of Di Giovanni and Radicella (1990). Because of the availability of increased data sources, the model formulations have been updated so as to enhance the NeQuick performance and provide better global ionospheric representations. Those improvements resulted in the NeQuick version 2 (namely, NeQuick 2) model (Nava et al., 2008). Historically, Mosert de Gonzalez and Radicella (1990) relied on some data sources obtained from Argentinean ionosondes in order to propose some novel empirical equations for computing the bottomside thickness parameter of the NeQuick model (namely, B2bot). This B2bot is an original bottomside thickness of the NeQuick 2 model which is computed using (4.2) and (4.3) in Chapter 4.

Afterwards, Zhang et al. (1991) proposed a novel variable coupling between topside and bottomside ionospheres and addressed that the shape of topside ionosphere was emulated feasibly using their proposed topside shape parameter (k) which was computed using the observed total electron content (TEC) values and the measured ionosonde data. It is worthy to note that the B2bot of the NeQuick model is analogous to the B0 of the IRI model (Coïsson et al., 2008) as though they are defined similarly as the bottomside thickness parameters, however, the derivations and the definitions of these two parameters are different. In contrast to worldwide digisondes, the (B0, B1) parameters are not available on FMCW ionosonde at Chumphon station, hence, computing those parameters using available instruments

at Chumphon is an interesting task and has never been studied nor analyzed in the previous literatures. Moreover, at Chumphon station, there exist one FMCW ionosonde for basic ionospheric parameters and a JAVAD GPS receiver for the processed vertical TEC (VTEC) values. A novel equation proposed by Zhang et al. (1991) being in a form of TEC values and ionospheric parameters can be rearranged to give an alternative for the B2bot instead of the original B2bot equations of Mosert de Gonzalez and Radicella (1990).

Moreover, the topside shape parameter (k) proposed by Zhang et al. (1991) can also be used to compute the topside electron density profiles (EDPs) over Chumphon station as if the topside EDPs are an application of the B2bot computation. Likewise, in contrast to digisondes, the ionospheric EDPs are also not available on FMCW ionosonde at Chumphon, therefore, computing and depicting the EDPs using available devices at Chumphon is another interesting work and has also never investigated nor analyzed in the previous literatures.

Finally, another topic in this thesis is the study of time delays which affect significantly on GPS satellites. The satellite signals traveling through the ionosphere suffer refraction and retardation which result in the time delay, this kind of time delay is called ionospheric delay. The ionospheric delay is closely related to total electron content (TEC) in ionosphere and should be corrected for global navigation satellite system (GNSS). It is thus a crucial task to be studied in this thesis. However, the studied ionospheric delays are only the preliminary results of satellite delay profiles. Exact TEC model construction and ionospheric delay correction are not the objectives of this thesis, however, additional details can be read in many publications, e.g., Kakinami et al. (2009) and Lean et al. (2011).

1.2 Objectives of thesis

1. To propose a new expression for computing the B2bot of the NeQuick 2 model instead of the original B2bot equations and compare its diurnal variations over Chumphon with the IRI-2012 model and the original B2bot of the NeQuick 2 model.

2. To compute topside electron density over Chumphon using NeQuick topside formulation and compare topside EDPs with three options of the IRI-2012 model.

3. To compute TEC and ionospheric delays over Chumphon and compare these values with the IRI-2012 model and International GNSS service (IGS).

1.3 Scope of thesis

For the first contribution, the period of study for a new B2bot (B2bot_Pro) expression is during 2004-2006. The reasons are as follows. Although FMCW ionosonde-based ionospheric monitoring has operated over Chumphon (10.72°N, 99.37°E, GMT+7 hours) since 2003, only a few studies about TEC values over Chumphon was conducted and published in literatures. One of those studies is Kenpankho et al. (2011) in which they revealed the results of TEC and slab thickness over Chumphon during 2004-2006. I think that their results are reliable and are well-known by several researchers. Hence, the period of year 2004-2006 is a suitable duration to propose and study preliminarily a new proposed expression of the B2bot_Pro and its diurnal variations.

For the second contribution, the study period for depicting topside EDPs and topside TEC values are only in 2007. Since year 2007 is a year which has nearly minimum solar activity among 24 solar cycles, the ionospheric values predicted by any models or observed by any instruments might yield a great discrepancy one another unexpectedly. Hence, it is very interesting to study the topside ionosphere in these minimum periods. Moreover, there are very large data sources for depicting topside EDPs by several hours, dates, and months, and years, hence, some equinoxes and solstice dates in 2007 are only chosen to study in this contribution of this thesis.

For the last contribution, the study period for computing the TEC values and ionospheric delays are only in 2015, since the TEC values are not available in several days and months in 2016, and year 2017 does not reach the end of year. Moreover, the observed data are grouped into three seasons, i.e., winter, equinox, and summer.

1.4 Benefits of thesis

The new expression for computing the bottomside thickness parameter for FMCW ionosonde in this thesis can be used to compute electron density values in ionosphere, draw electron density profiles (EDPs) in ionosphere using NeQuick topside formulation, and compute other ionospheric parameters such as topside scale height, approximated TEC values and others.

1.5 Contributions of thesis

The first contribution of this thesis is to propose a new expression for computing the B2bot of the NeQuick 2 model instead of the original B2bot equations of Mosert de Gonzalez and Radicella (1990) as described in Chapter 4. Afterwards, the diurnal variations of the computed B2bot_Pro are compared with those of the original B2bot of the NeQuick model and the predicted B0 with ABT-2009 and Bil-2000 of the IRI-2012 model (namely, B0_ABT and B0_Bil, respectively, in this thesis). Note that the B2bot computed by the new proposed expressions in this thesis are designated as the B2bot_Pro which are computed using (4.13).

The second contribution of this thesis is to compute and analyze the topside electron density over Chumphon station using NeQuick topside formulation as described in Chapter 5. The topside EDPs are depicted and compared with those of the IRI-2012 model. Afterwards, the topside TEC values, the integrations of absolute difference, the absolute differences, and the difference values are also computed and analyzed in Chapter 5.

The last study of this thesis aims to investigate and analyze the satellite delay profiles over Chumphon using ionospheric delays of GPS signals as described in Chapter 6. Since the TEC values are directly related to the ionospheric delays, hence, the diurnal variations in TEC values and ionospheric delays are also shown simultaneously. Three data sources for studying and comparing TEC values and ionospheric delays in Chapter 6 are obtained from the observation, the IRI model, and the IGS. Furthermore, the absolute differences of TEC and ionospheric delays are also computed in this Chapter.

This material is reserved for educational use only, not allowed for commercial use.

Forbidden to modify the content, and cite the document when use.

1.6 Thesis outline

This thesis is divided into 6 chapters as follows.

Chapter 1 describes the background and motivation, the objectives, the scope, the benefits, and the contributions for composing this thesis.

Chapter 2 presents the features and the models for ionosphere. Ionospheric vertical structure, Ionospheric variations (e.g. diurnal, seasonal, and latitude variations), frequency modulated-continuous wave (FMCW) ionosonde, ionogram and ionospheric parameters, the IRI model, the NeQuick 2 model, and Chumphon station.

Chapter 3 addresses GPS technology. Principle of GPS system, GPS code, GPS receiver, RINEX format, as well as computations of TEC and slab thickness.

Chapter 4 describes the computations and the comparisons of bottomside thickness parameters. The major issues include an original bottomside thickness of NeQuick 2 model, a new proposed bottomside thickness of NeQuick 2 model, the IRI B0 values, comparison results of the B2bot_Pro, physical explanations and discussions.

Chapter 5 presents an application of bottomside thickness parameter for topside ionosphere using some expressions of the NeQuick 2 model. The related topics include NeQuick topside formulation, the IRI model with topside density options, as well as comparison results of topside EDPs and topside TEC values.

Chapter 6 introduces satellite delay profiles. Ionosphere delay as well as comparison results of TECs and Ionospheric delays are described in this chapter.

Finally, the conclusions are drawn in Chapter 7. Conclusions, suggestions, and future works are expressed in this chapter.

CHAPTER 2

IONOSPHERE FEATURES AND MODELS

This chapter describes the basic details about ionosphere, frequency modulated-continuous wave (FMCW) ionosonde, ionosphere models, and Chumphon station, Thailand. Ionosphere is divided into two sections, i.e., the structure of ionosphere and the variations in ionosphere. For FMCW ionosonde, FMCW ionogram, and ionosonde-based ionospheric parameters are explained. For ionosphere models, two well-known ionospheric models are described such as International Reference Ionosphere (IRI) model and NeQuick 2 model. The last section is devoted to Chumphon station. The details of each section are described as follows.

2.1 Vertical structure of ionosphere

The ionosphere is an ionized layer of the Earth's atmosphere ranging from 50 km up to 1,500 km above the Earth's surface. It consists of neutral particles, free electrons, and ions where the latter are called as plasma. In Figure 2.1, the structure of neutral atmosphere consists of troposphere, stratosphere, mesosphere, thermosphere, and exosphere. The neutral atmosphere is classified in any layers using temperature profiles. For the structure of ionized atmosphere, there are troposphere, stratosphere, ionosphere, and protonosphere (or plasmasphere). The ionized atmosphere is classified in any layers based on the number of ionized gases. In ionosphere, the plasma is removed from neutral atoms or molecules to leave protons (positive ions) and electrons (negative ions) by the extreme ultraviolet (EUV) and X-ray radiation which are radiated from the sun. This process is called photoionization. The net amount of these several free electrons and ions is determined by the rate specifying the types of ions recombined with electrons to form neutral atoms. This mentioned process is called recombination. Details about the ionosphere can be read on a web site <https://en.wikipedia.org/wiki/Ionosphere>.

This material is reserved for educational use only, not allowed for commercial use.

Forbidden to modify the content, and cite the document when use.

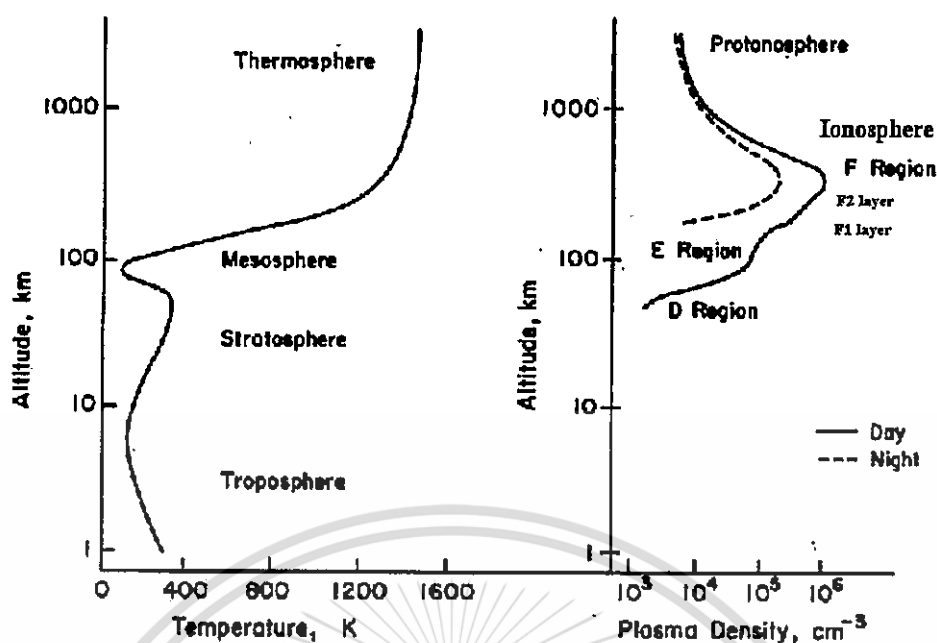


Figure 2.1 The structure of neutral (left panel) and ionized (right panel) atmosphere. (<http://utd500.utdallas.edu/ionosphere.htm>)

On the right panel of Figure 2.1, there are four layers in the ionosphere during daytime including D layer, E layer, F1 layer, and F2 layer. During nighttime, F1 and F2 layers combine together to form a single F layer. The lower boundary of the ionosphere is the region where the most penetrating radiations produce free ions and ion pairs that are sufficient to affect the propagation of radio waves in the D region. Meanwhile, the upper boundary of ionosphere is affected by the situation of solar wind. Moreover, the ionosphere can also extend to greater distances representing the solar wind shadow in the nighttime.

The D layer ranges from 50 km to 90 km above the Earth surface. Ionization exists due to hydrogen radiation at a wavelength of 121.5 nanometers (nm) ionizing nitric oxide (NO). In addition, the hard X-rays (wavelength < 1 nm) during high solar activity might ionize N₂ and O₂ molecules. During nighttime, cosmic rays produce a residual amount of ionization. In the D layer, the recombination is high and the net ionization is low, but loss of wave energy is great due to frequent electron collisions. As a result, high frequency (HF) radio waves are not reflected by D layer but suffer a loss of energy. This is a main reason for the absorption of HF radio waves, particularly

This material is reserved for educational use only, not allowed for commercial use.

at 10 MHz and lower. The absorption is lower progressively whereas the signal frequency gets higher. The absorption is small at night, but it is large around the noontime. The thickness of D layer reduces greatly after sunset, but a small height remains because of cosmic rays. An example of D layer in action is the disappearance of distant AM broadcast during daytime (Aggson et al., 1995). During solar proton event, ionization can reach abnormally high levels in the D region over high and polar latitudes. Such very rare event is known as polar cap absorption (or PAC) events, because the extreme ionization enhances significantly the absorption of radio signals passing through these regions. In fact, the level of absorption can increase by many tens of dB during intense event and it is enough to absorb mostly HF radio signal propagation. Such event typically last during 24 to 48 hours.

The E layer is the middle layer ranging from 90 km to 140 km above the Earth surface. Ionization exists due to soft X-ray (1-10 nm) and ultraviolet (UV) solar radiations of oxygen molecule (O_2). The average height of E layer is about 110 km and the maximum of electron density also exists at about 110 km. In general, E layer can slightly reflect radio wave having frequencies lower than 10 MHz and may also absorb slightly on higher frequencies. The abnormal ionization can sometimes occur in E layer, as it is called Sporadic E (E_s) event. This event is caused by violent interference in VHF band. It occurs just a moment in both daytime and nighttime as well as in any seasons. Normally, it looks like patchy clouds which spread out between 1 km and hundreds of km. The occurrence and the ionized intensity do not relate to the solar radiation. It is hard to predict the occurrence time of E_s event. During intense Sporadic E event, E layer can reflect frequencies up to 50 MHz and higher. The vertical structure of E layer is primarily determined by the effects of ionization and recombination. E layer rapidly disappears because primary source of ionization is no longer present during nighttime. The increment of height maximum increases the distance to which radio waves can travel by reflection from this layer after sunset.

The F layer is the highest layer ranging from 140 km to 500 km or more above the Earth surface. Ionization exists due to soft X-ray (1-10 nm) and extreme ultraviolet (EUV) (10-100 nm) radiations from the sun. The photoionization in this

layer is the strongest among any layers, therefore, the highest electron density occurs in this layer at about $10^5 - 10^6$ electron/cm⁻³ and long distance HF radio propagation can be fulfilled by F layer. During daytime, the F layer is divided into F1 and F2 layers.

The F1 layer ranges from 140 km to 240 km above the Earth surface. The average height of F1 layer is about 220 km. It disappears at nighttime since it combines with F2 layer to form a single F layer. The maximum of ionization occurs around local noontime. Ionizations of both oxygen atom by Helium emission and Nitrogen molecule disappear after sunset. The ionization is mostly in molecular form and disappears by the recombination.

The F2 layer begins at about 240 km and shows a peak electron density at about 500 km in the daytime. The electron density values always vary highly with respect to the height. Ionization occurs due to extreme ultraviolet (EUV) radiation (10-100 nm) on oxygen atom. The F2 peak electron density values ($NmF2$) are present in the F2 layer at about 400 km. Furthermore, the main features of ionosphere are to reflect the radio waves in the high frequency (HF) band from a transmitter to its receiver on the ground and also to impact the radio signal transmitted from a satellite to a ground receiver travelling through ionosphere. The effects on signal propagation depend on the frequency and the plasma density along those ray paths. The F2 layer is the most important layer for long distance HF transmission since it is the uppermost layer and the F2 peak electron density can well reflect the highest critical frequency in the HF band. Moreover, the variations in F2 layer near the magnetic equator are caused by a complex physical system which is called as a nonlinear dynamic process. Hence, there is a need to improve the understanding of the ionosphere and the accuracy of critical frequency maps which are used for computing HF communication links.

2.2 Ionospheric variations

The vertical structure of ionosphere and the distribution of electron density change obviously with time (diurnal and seasonal variations), solar activity (sunspot number), and space (geographic location). The details of ionospheric variations are

briefly described as follows. Details about season occurrence can be read on a web site <http://physics.weber.edu/schroeder/ua/sunandseasons.html>.

2.2.1 Diurnal variation

Diurnal variations are referred to the variations in daytime and nighttime in which they are affected mainly from the Earth's rotation. Electron density values in daytime reach their peaks around local noontime. Electron density values in nighttime are much lower than those in daytime because of higher recombination rates in the absence of solar radiation.

2.2.2 Seasonal variation

At different times of the year, the Sun is vertically above different geographic locations and the Earth's season can be divided into 4 seasons, i.e., March equinox, June solstice, September equinox and December solstice. When the Sun is crossing the equator and it locates with equal distances from the North Pole and the South Pole during March equinox (March and April) and September equinox (September and October). For June solstice (May – August), the Sun is nearer the North Pole than the South Pole and the period between sunrise and sunset is longer at the northern hemisphere (summer) and shorter at the southern hemisphere (winter). On the other hand, for December solstice (November – February), the Sun is nearer the South Pole than the North Pole and the period between sunrise and sunset is longer at the southern hemisphere (summer) and shorter at the northern hemisphere (winter). The photoionization during equinox season is larger than one during solstice season, therefore, the maximum electron density values frequently occur in the equinox season. Several investigations of ionosphere variation have been conducted so as to comprehend the impacts of seasons on local times. The data and the methodology for investigating in this thesis are grouped into 3 seasons, i.e., equinox season (March, April, September, and October), summer season (May – August), and winter season (January, February, November, and December) (Jamjareegulgarn et al., 2016; 2017).

2.2.3 Latitudinal variation

The variations of electron density in ionosphere rely on not only the height above the Earth's surface occurring the chemical processes, but also the different physical processes related to the configurations of geomagnetic field. These

phenomena lead to the latitude variations of ionosphere. Moreover, the sun's positions relative to the atmosphere also cause the latitudinal variations of ionospheric density values. An observer position with small zenith angles are associated with larger ionization rates. Note that the solar zenith angle is measured vertically from an observer's local position to the Sun and it can be used to determine the ionization intensity. The latitudinal variation can be divided into 3 latitudes relying on geomagnetic lines of the Earth such as low latitude, middle latitude, and high latitude. The geomagnetic latitudes differ from the geographic poles of the Earth. The geomagnetic poles and the geographic poles of the Earth are aligned in the opposite directions. The northern geomagnetic pole is at the southern geographic pole and vice versa. In Figure 2.2, the horizontal grey lines represent the geographic latitude lines, whereas the black curved lines represent the geomagnetic latitude and geomagnetic equator (or magnetic equator) lines. It can be seen that the magnetic equator is above the geographic equator and passes through many continents excluding North-America continent.

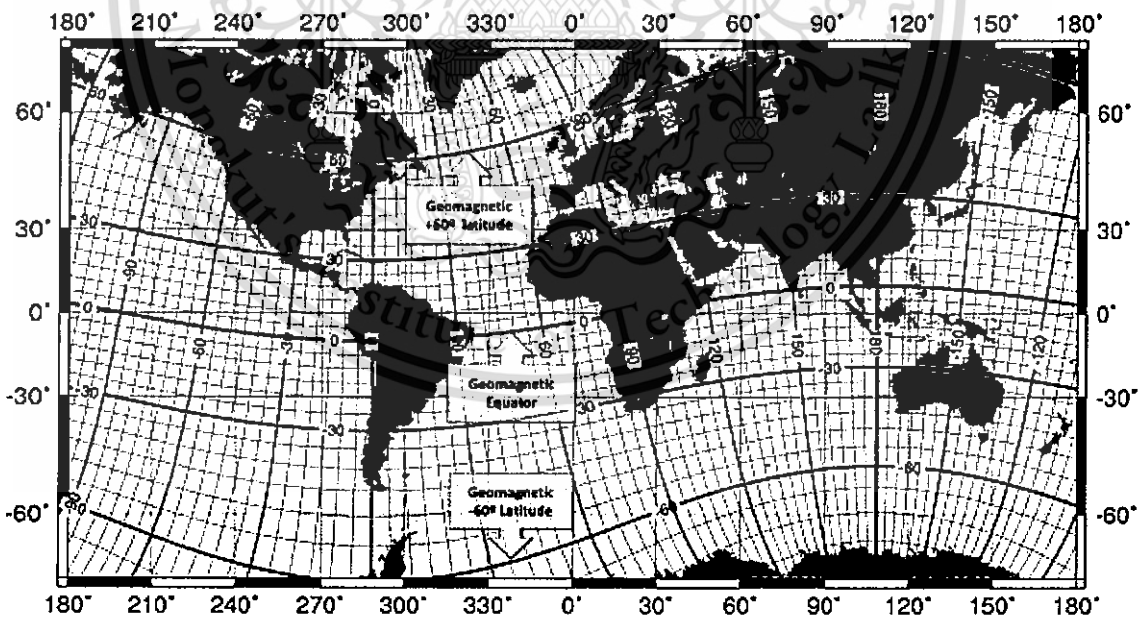


Figure 2.2 Geomagnetic latitudes and geographic latitudes. (Sajedi and Abdollahi, 2012)

At low latitude, the plasma always flows up to higher altitude by the $E \times B$ drift and $E \times B$ drift is perpendicular to the geomagnetic field. Zonal wind and geomagnetic field lines are responsible for producing electric fields (E) and magnetic fields (B) for $E \times B$ plasma drift directly, respectively. The zonal wind moves westward during daytime and eastward during nighttime leading to eastward and westward electric fields (E) in the daytime and nighttime, respectively. During daytime, the eastward electric field leads to a decrement of peak electron density values at magnetic equator (plasma depletion) and an increment of peak electron density values at EIA crests. On the other hand, the westward electric field during nighttime leads to peak electron density at middle latitude region. Moreover, B is the geomagnetic field lines which is nearly horizontal leading to unique transportation process on the plasma in this region. The plasma can move either east-west or up-down direction.

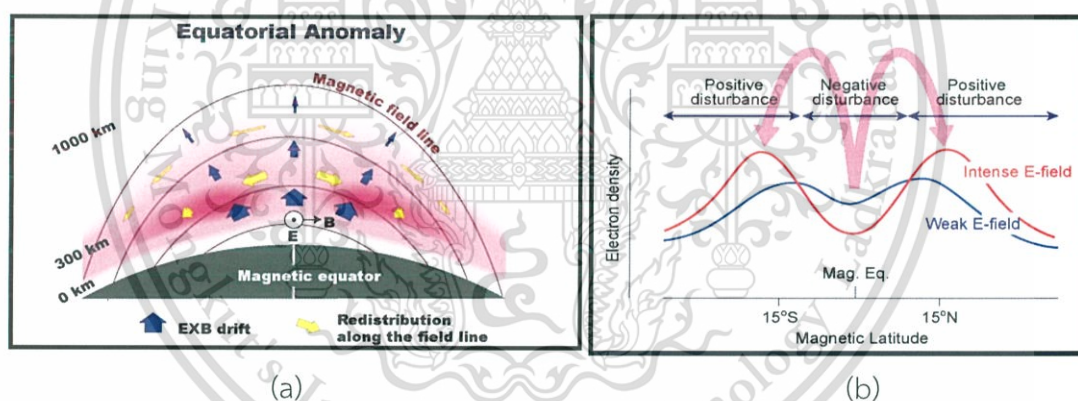


Figure 2.3 (a) Equatorial Ionization Anomaly (EIA) (b) the variations of electron density values and electric fields. (Maruyama, 2012)

During daytime, the $E \times B$ plasma drift is uplifted to higher altitude because of eastward electric field, and then diffuses along the geomagnetic field line toward higher latitudes due to the Earth's gravitational and pressure gradient forces, where it reverses during nighttime. At sunrise (dawn) and sunset (dusk) hours, a number of large east-west electric fields always occur due to sharp electron density gradient between daytime and nighttime, therefore the plasma moves up-down direction. The combination of electro-dynamics upward drift as well as downward diffusion

This material is reserved for educational use only, not allowed for commercial use.

causes a plasma motion like a fountain, it is thus designated as fountain effect as shown in Figure 2.3. Fountain effect causes two crests of electron density near $\pm 15^\circ$ geomagnetic latitudes around magnetic equator which is called as “Equatorial Ionization Anomaly” (EIA) or “Appleton Anomaly”. Interactions between transequatorial neutral winds and the strength of fountain effect play important roles to produce asymmetric EIA crests. Details about EIA phenomena and fountain effect can be read additionally from Maruyama, 2012. In this region, EIA is responsible for the largest ionospheric plasma density. Low latitude region spans between -30 and $+30$ degrees of magnetic equator and equatorial latitude is equal to 0 degree.

At middle latitude (or mid-latitude), it is well-known that the collisions between charged particles and the neutrals are an important process. The conditions in magnetosphere do not affect directly on the plasma in this region because of significant dip angles of geomagnetic fields. However, the plasma can flow quickly along the geomagnetic field lines and avoid the conjugate ionosphere. Pressure gradient, gravitational force, and neutral wind lead to the parallel drift of plasma. Mid-latitude is the least varying and disturbed region among three geographic latitudes. It is usually found that this region is not affected by the horizontal magnetic field compared with equatorial region. Mid-latitude region covers from 30 to 60 degrees.

For high latitude, magnetic field is nearly vertical, therefore, the ionosphere is connected to the magnetosphere via magnetic field lines. Since a lot of ions are charged within these regions, they are interactive to the magnetic field. Moreover, since the electric force causes the gravitational force and the pressure gradient force in these regions, the ionosphere is changed suddenly by the extreme enhancement of electric field in magnetosphere as well as the auroral precipitation during the periods of geomagnetic storm and sub-storm. The latter are examples of active geomagnetic conditions. Since the solar radiation strikes the atmosphere at more oblique angle in this region, electron density values are generally lower than those in lower latitude regions. Moreover, the plasma instabilities frequently occur because this region is susceptible to external influences of the Earth. The main causes of this susceptibility are twofold: a) the magnetic field runs nearly vertical and b) the

magnetic field lines connect to the outer part of magnetosphere. High latitude region locates between the northern and southern magnetic equator about 60 to 90 degrees.

2.3 FMCW ionosonde

FMCW ionosonde is a special kind of radar for monitoring the ionosphere. Figure 2.4 shows block diagram of a FMCW ionosonde system (Kenro, 2009) whose operating parameters are shown in Table 2.1. The ionosonde system consists of several modules as follows.

1. Two antennas: one antenna for a high frequency (HF) transmitter which can automatically tunable over a wide range 2-30 MHz and another antenna for a tracking HF receiver which can automatically track the frequency of the transmitter.
2. Low pass filter and power amplifier circuits with a suitable radiation pattern which transmits vertically upwards and is efficient over the whole frequency range.
3. Personal computer: it is used for data recording.
4. Connecting components such as coaxial cable, RS232, and 25-pin cable.

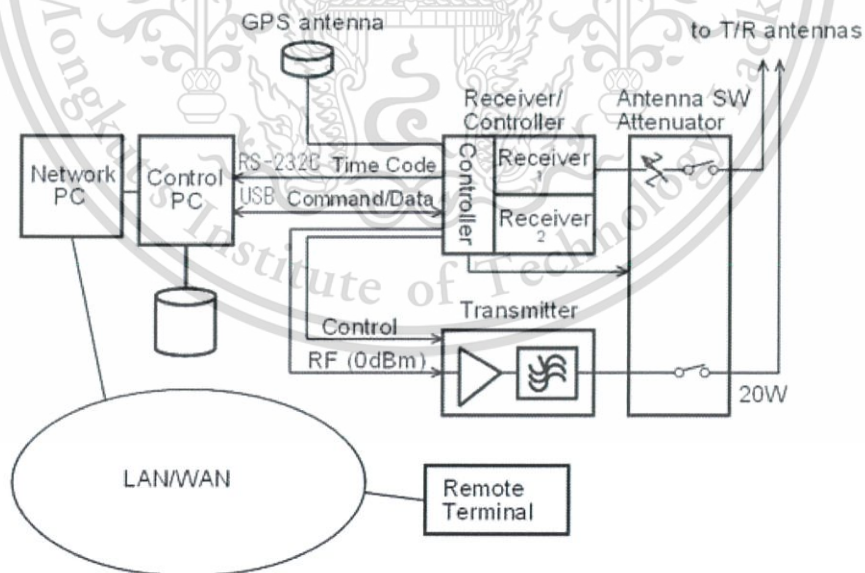


Figure 2.4 Block diagram of a FMCW ionosonde system. (Kenro N., 2009)

Table 2.1 Operating parameters of a FMCW Ionosonde.

Ionosonde parameters	FMCW with pseudo-random Tx/Rx switching
Peak Tx power	20 W
Average Tx power	10 W
Frequency range	2-30 MHz
Sweep rate	100 kHz/s
Sweep repetition period	5 minutes
Antenna	Folded dipole on Tower 27 meters

The FMCW ionosonde transmits radio waves continuously from 2-30 MHz into ionosphere for each round and then receives echoes. The transmission starts from 2 MHz and increases the frequency up to 30 MHz with the sweep rate of 100 kHz. Note that these radio waves are reflected at various layers of the ionosphere at heights of 80-500 km. These echoes are received by the receiver, analyzed by the control system, and recorded in a computer every 5 minutes. Their reflected trace is displayed as an ionogram which is a graph of reflection height (actually time between transmission and reception of pulse) versus carrier frequency as shown in Figure 2.5. These ionograms are manually scaled (Wakai et al., 1987) at every 15 minutes.

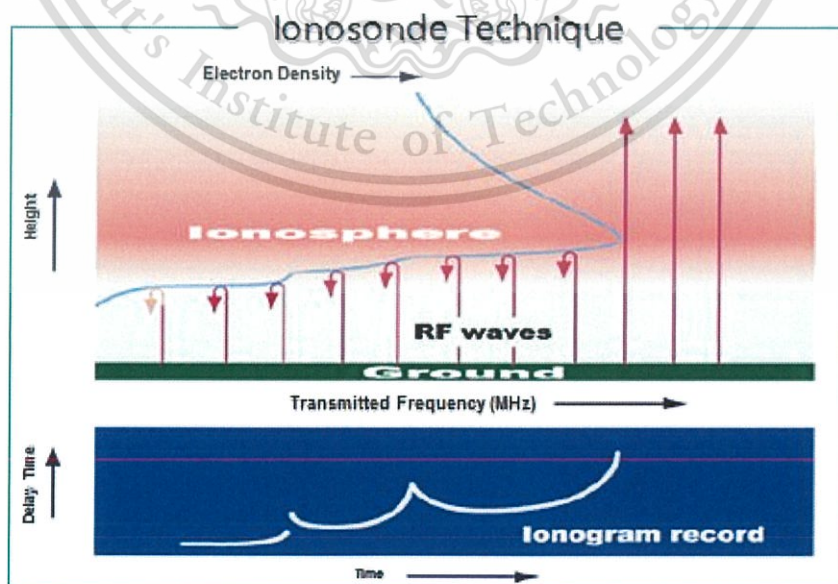


Figure 2.5 Ionospheric observation with a FMCW ionosonde. (Maruyama, 2010)



Figure 2.6 Global map of digisonde locations. (<http://digisonde.com/>)

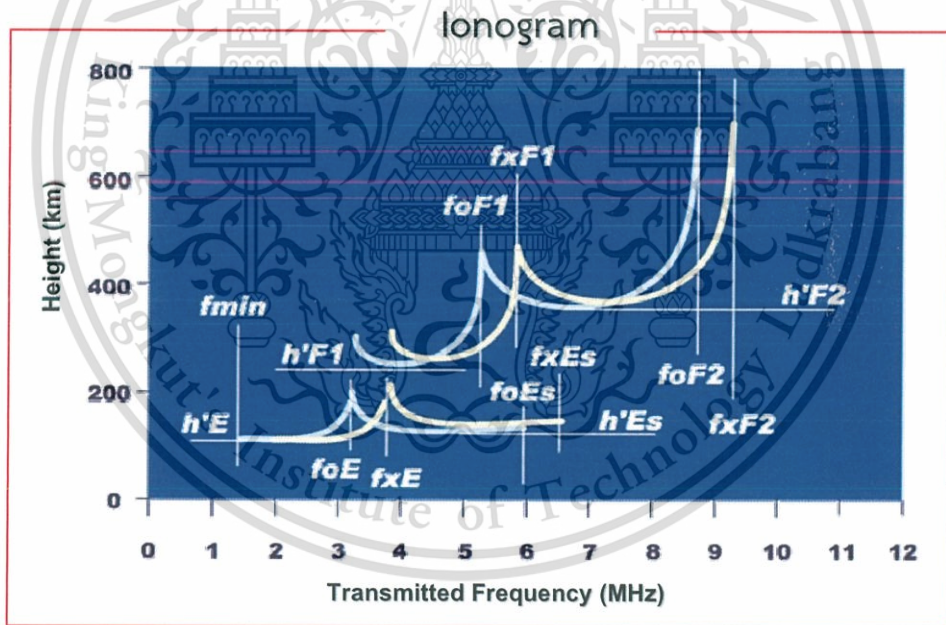


Figure 2.7 A graphical illustration of Ionogram with ionospheric parameters.

(http://wdc.nict.go.jp/IONO/contents/Ionogram_J.html)

Figure 2.6 illustrate a global map of digisonde locations in several countries. Lowell Digisonde International supporting these digisondes has manufactured and marketed the Digisonde-Portable-Sounder-4D (DPS4D), the commercially available This material is reserved for educational use only, not allowed for commercial use.

Forbidden to modify the content, and cite the document when use.

latest ionosonde system of the digisonde. Digisonde stands for “Digitally Integrating Goniometric IonoSONDE” which is an ionospheric radar. The DPS4D is the only instrument that measures all parameters of HF waves reflected from the ionosphere and calculates automatically the ionospheric electron density profile in real time. Further information can be read on a web site <http://digisonde.com/>.

2.4 Ionogram and ionospheric parameters

Ionogram is a graphical illustration of echo strength with ionospheric parameters where the x-axis is transmitted frequency of FMCW ionosonde (MHz) and the y-axis is virtual height (km) as illustrated in Figure 2.7. Radio wave from FMCW ionosonde is sent out toward the ionosphere with increased frequency every 100 kHz/sec and the echo turns back subsequently from a higher height. The maximum frequency of echo at each layer corresponding to the electron density peak of each layer is designated as critical or plasma frequency. Any signals with frequencies exceeding F2 layer plasma frequency (f_oF2) do not return to the ionosonde.

Ionogram is used to characterize the vertical structure of E and F layers and to forecast the transmitted signal strength for HF communications, excluding D layer with low electron density values. Here, the critical frequencies of ordinary waves (f_oX) and extraordinary waves (f_xX) of each layer are demonstrated in Figure 2.7, i.e., in E layer (f_oE and f_xE), in F1 layer (f_oF1 and f_xF1), and in F2 layer (f_oF2 and f_xF2). In Figure 2.7, the rightmost lines are the apparent height (h') of delayed echoes with respect to frequencies. The apparent heights are obtained from minimum heights of E layer ($h'E$), F1 layer ($h'F1$), and F2 layer ($h'F2$). Moreover, MUF(3000)F2 is another parameter which is the maximum usable frequency reflected from the F2 layer and received at a distance of 3,000 km. The MUF(3000)F2 can be read out directly from ionogram with logarithmic frequency scale. The ratio between MUF(3000)F2 and f_oF2 is equal to $M(3000)F2$ which is a propagation factor.

In this thesis, the f_oF2 , the f_oE , and the MUF(3000)F2 parameters are manually scaled from the ionograms recorded at Chumphon using special-10C-2000.exe program (Nakamura, 2003). The scaled f_oF2 is used to compute F2 layer

This material is reserved for educational use only, not allowed for commercial use.

Forbidden to modify the content, and cite the document when use.

electron density peak or $NmF2$ (unit: e/m^3) using an equation of Goodwin et al. (1995) as shown in (2.1).

$$NmF2 = 1.24 \times (foF2)^2 \times 10^{10} \quad (2.1)$$

Moreover, to investigate other ionospheric variations, those mentioned scaled parameters from FMCW ionosonde are not sufficient and some ionospheric parameters are not available on FMCW ionosonde. For example, to illustrate the bottomside electron density profiles, the F2 layer peak height ($hmF2$) and the bottomside thickness parameters are necessary following to the bottomside IRI model. Also, total electron content (TEC) being not available on FMCW ionosonde is very important for investigating the variations in electron density as well as computing the ionospheric delays for Global Navigation Satellite System (GNSS) or other communication systems. For instance, calculating the $hmF2$, the TEC, the bottomside thickness parameters are described in Section 2.5, Section 3.4, and Chapter 4, respectively.

The applicable examples of these ionospheric parameters are as follows.

1. Reflecting the HF signals for longer distance in navigation systems for airplane, ocean liner, etc.
2. Investigating the variations in electron density profiles and their impacts on TEC, satellite delays, etc.
3. Calculating the ionospheric delays for satellite-based navigation systems using total electron content (TEC) and constructing the exact ionospheric delay model.
4. Investigating the atmosphere temperatures and the space weather for supporting communication systems.
5. Predicting the occurrence times of disaster phenomena such as Tsunami, earthquake, etc.
6. Investigating the atmospheric phenomena due to the greenhouse effect or global warming.
7. Investigating the impacts of space fluctuation on irrigation and drought, etc.

2.5 International Reference Ionosphere (IRI) model

The International Reference Ionosphere (IRI) model, a famous empirical ionospheric model, provides the monthly median values of several ionospheric parameter such as peak height, plasma frequency, electron density, total electron content, electron and ion temperatures, and ion compositions, etc. for given location, time, and sunspot number (Bilitza, 2001). The committee on Space Research (COSPAR) and the International Union of Radio Science (URSI) who established the IRI models have developed and updated a series of IRI models. In the latest version, IRI-2012 model, more improvements have been made, for example, on the new models for the bottomside thickness parameter (B_0) and shape parameter (B_1), the electron density in the bottomside ionosphere (Bilitza et al., 2014). Many data sources are taken to account for improving and updating the IRI model such as digisonde/ionosonde networks, ISIS and Alouette topside sounder, incoherent scatter radars (ISRs), and in situ instruments using ground stations, rockets, or satellites.

Moreover, the IRI model has used two different sub-routines of computer programs to provide two different F peak models predicting any peak values of F layer, i.e., a model of the International Union of Radio Science (URSI) developed by Rush et al. (1989) and another model of the International Radio Consultative Committee (CCIR) developed by several researchers of CCIR. Two computational maps of URSI and CCIR models are based on spherical harmonics-based mapping techniques, the 12-month running mean relative sunspot numbers ($Rz12$), and the data sources from worldwide network of ionosondes. Hence, the maps of both models are enable to describe and forecast F2 layer characteristics, i.e., the monthly median of foF_2 and hmF_2 values. The CCIR option is suggested for continental areas, because it has the shortcomings above the oceans and the southern hemisphere. Therefore, the CCIR option is considered to predict the peak values of F layer in this thesis, because Chumphon province is located on the land of Thailand. On the other hand, the URSI option outperforms the CCIR option over the ocean areas since the aeronomic theory is used to complement the data gaps over the ocean before using the spherical harmonics mapping.

In the IRI model, four main ionospheric parameters in F2 layer are used to model the bottomside electron density profile using an analytical function (Ramakrishnan and Rawer, 1972). These four parameters include the F2 layer peak electron density ($NmF2$), the F2 layer peak height ($hmF2$), the bottomside thickness parameter ($B0$), and the bottomside shape parameter ($B1$). The analytical function of the IRI model for illustrating the bottomside F2 layer electron density profile $\langle Ne_{bot}(h) \rangle$ is shown in (2.2) where $\cosh(x)$ is a hyperbolic cosine function of x and h is a varying height.

$$Ne_{bot}(h) = NmF2 \times \frac{\exp(-x^{B1})}{\cosh(x)}, \quad (2.2a)$$

and

$$x = \frac{hmF2 - h}{B0} \quad (2.2b)$$

In the IRI-2012 model, the $B0$ is defined to be the subtraction between the $hmF2$ and a height where the bottomside electron density drops down to be 24% of the $NmF2$ (namely, $h0.24$) and the variable x is equal to 1. Hence, the knowledge of these four ionospheric parameters is very important. Furthermore, the $hmF2$ can be computed using a close correlation between the $hmF2$ and the propagation factor $\langle M(3000)F2 \rangle$ (Rawer et al., 1978). In general, the $hmF2$ can be obtained from the scaled ionograms of the experimental instruments, i.e., ionosondes or digisondes, using the polynomial analysis program (POLAN) (Titheridge, 1985). However, the $hmF2$ is not available from the FMCW ionosonde. Therefore, the $hmF2$ in this thesis is computed using the mentioned expressions of Rawer et al. (1978), i.e.,

$$hmF2 = \frac{1490}{M(3000)F2 + \Delta M} - 176. \quad (2.3a)$$

Here, the correction factor ΔM and its variables are computed by

$$\Delta M = f1 \times f2 / ((foF2/foE) - f3) + f4 \quad (2.3b)$$

$$f1 = 0.00232 \times Rz12 + 0.222 \quad (2.3c)$$

$$f2 = 1 - Rz12/150 \times \exp\left(-(\psi/40^\circ)^2\right) \quad (2.3d)$$

$$f3 = 1.2 - 0.0116 \times \exp(Rz12/41.84) \quad (2.3e)$$

$$f4 = 0.096 \times (Rz12 - 25)/150 \quad (2.3f)$$

where ψ is the magnetic dip latitude, f_oE is the E layer plasma frequency, and $Rz12$ is the 12-month running mean relative sunspot number.

The ionospheric parameters of the IRI-2012 model can be accessible at a web location http://omniweb.gsfc.nasa.gov/vitmo/iri2012_vitmo.html. The model inputs include a year, a day, a time (UTC or LT), a geographic location, and a height as illustrated in Figure 2.8. Here, one can select a profile type and its parameters for gathering a set of observed parameters. For example, one select and input some values: “Height, km [60 – 2000], Start “100”, Stop “500”, Stepsize “20”. All of these model inputs must be specified following to a user’s needs. Moreover, one can specify any parameters which are needed to study and analyze additionally on the same web page of the IRI-2012 model as shown in Figure 2.9. The mentioned parameters are considered as optional inputs such as the sunspot number, the $Rz12$, the F10.7 radio flux, the upper boundary of electron content, the Ne topside, the F peak model, the bottomside thickness, etc. Note that the geographic location of Chumphon, Thailand used to study in this thesis is 10.72°N , longitude 99.37°E , and magnetic dip latitude 3.00°N .

The screenshot shows the web interface for the IRI-2012 model. At the top, there is a browser address bar with the URL https://omniweb.gsfc.nasa.gov/vitmo/iri2012_vitmo.html. Below the address bar, there are several sections for inputting model parameters:

- Select Date and Time:**
 - Year(1958-2019):
 - Note: If date is outside the Ap index range (1958-2016/12), then STORM model will be turned off.
 - Month: Day(1-31):
 - Time: Hour of day (e.g. 1.5):
- Select Coordinates:**
 - Coordinates Type:
 - Latitude(deg., from -90. to 90.): Longitude(deg., from 0. to 360.)
 - Height (km, from 60. to 2000.):
- Select a Profile type and its parameters:**
 - Height, km [60. - 2000.]: Start Stop Stepsize

At the bottom of the form, there are two buttons: and .

Figure 2.8 An example of setting model inputs on a web page of the IRI-2012 model.

Optional Input:

Sunspot number, Rz12 (0. - 400.) Ionospheric index, IG12 (-50. - 400.)
 F10.7 radio flux, daily (0. - 400.) F10.7 radio flux, 81-day (0. - 400.)

Electron content: Upper boundary (km., from 50. - 2000.)

Ne Topside F peak model foF2 Storm model

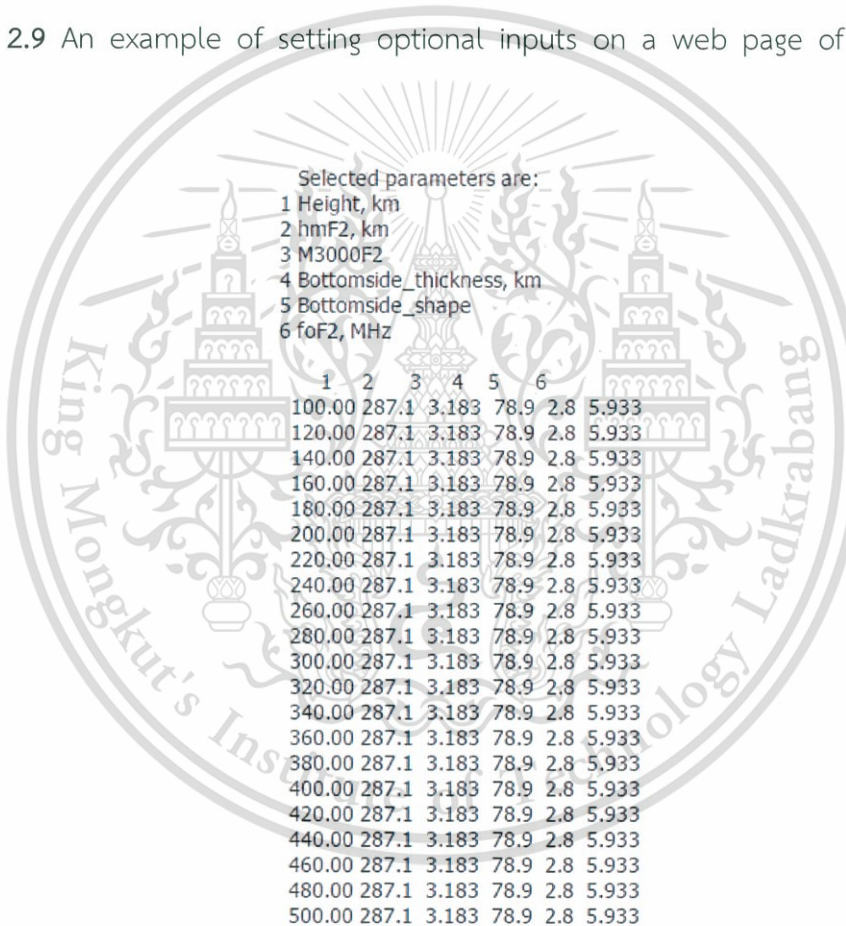
Bottomside Thickness F1 occurrence probability:

Auroral boundary foE auroral storm model Ne D-Region

Te Topside Ion Composition

Note: User may specify the following four parameters only for Profile type 'Height':

Figure 2.9 An example of setting optional inputs on a web page of the IRI-2012 model.



Selected parameters are:

- 1 Height, km
- 2 hmF2, km
- 3 M3000F2
- 4 Bottomside_thickness, km
- 5 Bottomside_shape
- 6 foF2, MHz

1	2	3	4	5	6
100.00	287.1	3.183	78.9	2.8	5.933
120.00	287.1	3.183	78.9	2.8	5.933
140.00	287.1	3.183	78.9	2.8	5.933
160.00	287.1	3.183	78.9	2.8	5.933
180.00	287.1	3.183	78.9	2.8	5.933
200.00	287.1	3.183	78.9	2.8	5.933
220.00	287.1	3.183	78.9	2.8	5.933
240.00	287.1	3.183	78.9	2.8	5.933
260.00	287.1	3.183	78.9	2.8	5.933
280.00	287.1	3.183	78.9	2.8	5.933
300.00	287.1	3.183	78.9	2.8	5.933
320.00	287.1	3.183	78.9	2.8	5.933
340.00	287.1	3.183	78.9	2.8	5.933
360.00	287.1	3.183	78.9	2.8	5.933
380.00	287.1	3.183	78.9	2.8	5.933
400.00	287.1	3.183	78.9	2.8	5.933
420.00	287.1	3.183	78.9	2.8	5.933
440.00	287.1	3.183	78.9	2.8	5.933
460.00	287.1	3.183	78.9	2.8	5.933
480.00	287.1	3.183	78.9	2.8	5.933
500.00	287.1	3.183	78.9	2.8	5.933

Figure 2.10 A result of the IRI-2012 model after submitting the model inputs.

IRI Model Parameters

- | | |
|--|---|
| <input type="checkbox"/> Electron_density (Ne), m^{-3} | <input type="checkbox"/> Atomic Helium (He^+), ions, percentage |
| <input type="checkbox"/> Ratio of Ne and F2 peak density($Ne/NmF2$)> | <input type="checkbox"/> Molecular Oxygen (O_2^+) ions, percentage |
| <input type="checkbox"/> Neutral Temperature Tn, K | <input type="checkbox"/> Nitric Oxide ions (NO^+), percentage |
| <input type="checkbox"/> Ion Temperature Ti, K | <input type="checkbox"/> Cluster ions, percentage |
| <input type="checkbox"/> Electron Temperature, Te, K | <input type="checkbox"/> Atomic Nitrogen (N^+) ions, percentage |
| <input type="checkbox"/> Atomic Oxygen ions (O^+), percentage | <input type="checkbox"/> Total Electron Content (TEC), $10^{16} m^{-2}$ |
| <input type="checkbox"/> Atomic Hydrogen (H^+), ions, percentage | <input type="checkbox"/> TEC top, percentage |
| <input checked="" type="checkbox"/> Height of F2 peak (hmF2), km | <input checked="" type="checkbox"/> Propagation factor M(3000)F2 |
| <input type="checkbox"/> Height of F1 peak (hmF1), km | <input checked="" type="checkbox"/> Bottomside thickness (B0), km |
| <input type="checkbox"/> Height of E peak (hmE), km | <input checked="" type="checkbox"/> Bottomside shape (B1) |
| <input type="checkbox"/> Height of D peak (hmD), km | <input type="checkbox"/> E-valley width, km |
| <input type="checkbox"/> Density of F2 peak (NmF2), m^{-3} | <input type="checkbox"/> E-valley depth (Nmin/NmE) |
| <input type="checkbox"/> Density of F1 peak (NmF1), m^{-3} | <input checked="" type="checkbox"/> F2 plasma frequency (foF2), MHz |

Figure 2.11 An example of selecting the studied parameters of the IRI-2012 model.

Figure 2.9 shows an example of setting optional inputs on a web page of the IRI-2012 model which is used in this thesis. The optional inputs for this thesis are specified as follows: the B0 is either Bil-2000 or ABT-2009 option, F peak model is only CCIR, foF2 Storm model is off, and the remaining parameters are default values. For the Rz12 values, one can enter one's own index value or one can rely on the internal index file of the IRI-2012 model. Figure 2.10 shows a result of the IRI-2012 model after specifying the parameters and their values. It can be seen that the height vary from 100-500 km with an increasing step of 20 km. At each altitude, the hmF2, the M(3000)F2, the bottomside thickness, and the bottomside shape, and the foF2 are also shown at each height regarding to the user's requirements. Furthermore, Figure 2.11 shows an example of selecting the studied parameters of the IRI-2012 model which can be retrieved by ticking the desired boxes.

2.6 NeQuick 2 model

Another well-known ionospheric model is the NeQuick model (Hochegger et al., 2000; Radicella and Leitinger, 2001) which is developed by the Aeronomy and Radio propagation Laboratory of the Abdus Salam International Centre for Theoretical Physics (ICTP), Trieste, Italy and at the Institute for Geophysics, This material is reserved for educational use only, not allowed for commercial use.

Astrophysics and Meteorology of the University of Graz, Austria. The NeQuick model is considered to be an evolution of the basis analytical model of Di Giovanni and Radicella (1990) and subsequently modified by Radicella and Zhang (1995). Due to the availability of increased data sources, the NeQuick's formulations are continuously updated to improve the model performance for providing the global ionospheric illustrations. These improvements resulted in the NeQuick model version 2 or NeQuick 2 model (Nava et al., 2008).

In Theory, the F2 layer electron density of the NeQuick model is described by the Epstein layer (Rawer, 1982) and represented by a following analytical equation

$$N_{e_{NeQ}}(h) = \frac{4NmF2}{\left(1 + \exp\left(\frac{h - hmF2}{B2bot}\right)\right)^2} \exp\left(\frac{h - hmF2}{B2bot}\right), \quad (2.4)$$

where $N_{e_{NeQ}}(h)$ is designated as the F2 layer electron density at a varying altitude h and the $B2bot$ is defined as bottomside thickness parameters of the NeQuick model (unit: km). Since a main contribution of this thesis is to propose a new expression of the $B2bot$, therefore, the details for computing the $B2bot$ values are described later in Chapter 4. Note that the $NmF2$ and the $hmF2$ are calculated using (2.1) and (2.3) as described earlier in Section 2.4.

The electron density and total electron content (TEC) of the NeQuick 2 model are conducted at a web model <http://t-ict4d.ictp.it/nequick2/nequick-2-web-model>. The model inputs include lower and higher endpoints, a year, a month, a time (UTC or LT), and 3 sources of solar activity (optional) as illustrated in Figure 2.12. Note that the computed electron density and TEC of the NeQuick 2 model are obtained using hourly monthly averages, hence, one cannot observe the NeQuick data in each day.

ปลอดภัย | <https://t-ict4d.ictp.it/nequick2/nequick-2-web-model>

You Are Here: [Home](#) / [NeQuick 2](#) / [NeQuick 2 Web Model](#)

NeQuick 2 Web Model

Computation and plotting of slant electron density profile and total electron content

Endpoints Coordinates

Map Lower endpoint: Latitude °N Longitude °E Height km

Higher endpoint: Latitude °N Longitude °E Height km

Satellite data: Azimuth °N Elevation ° Height km

Date and Time

Year(YYYY) Month Day(DD) Time

Solar Activity

R12 (source: NOAA-NGDC)

Daily Solar Radio Flux (source: NOAA-NGDC)

User Input Solar index type Value *

ITU-R compliant *

Figure 2.12 An example of inserting the model inputs into the NeQuick 2 model.

After inserting the model inputs and pressing a button “RUN NeQuick”, the model results appear on the web page as shown in Figure 2.13. The data in the first and second columns are the distances which are far from the Earth’s central point and range from 100-200 km with an increasing step of 10 km, respectively. The third and fourth columns are latitude 10.72 and longitude 99.37 unchangeably, respectively. The last column is the predicted electron density (electrons/m³) at an increased altitude. Meanwhile, a few lowest lines represent the TEC values during the distances of 100-200 km (unit: TECU or electrons/m²). Note that 1 TECU is equal to 1×10^{16} electrons/m².

Results

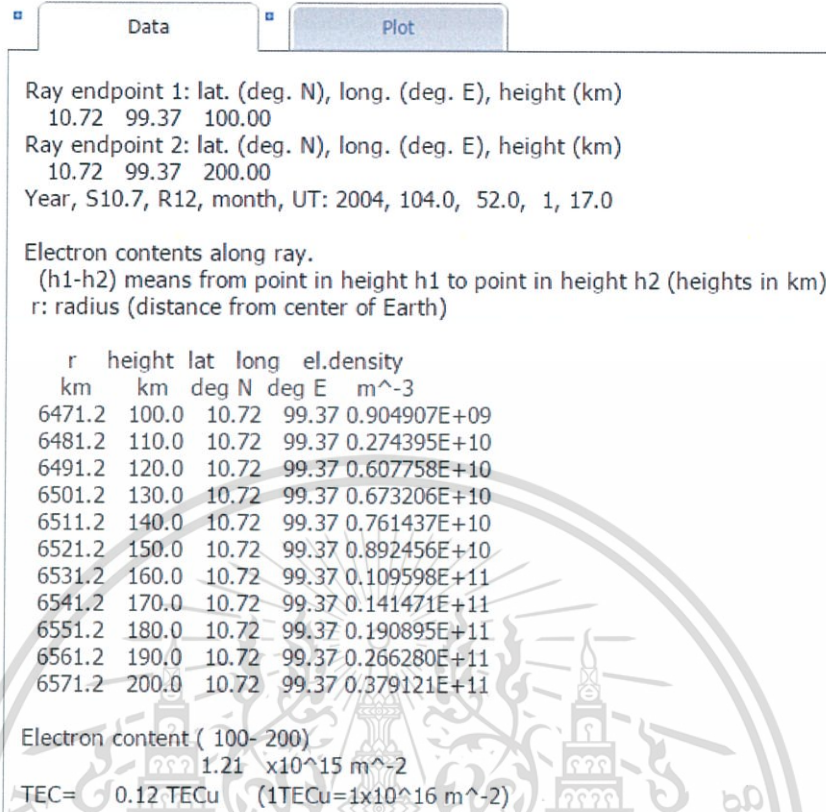
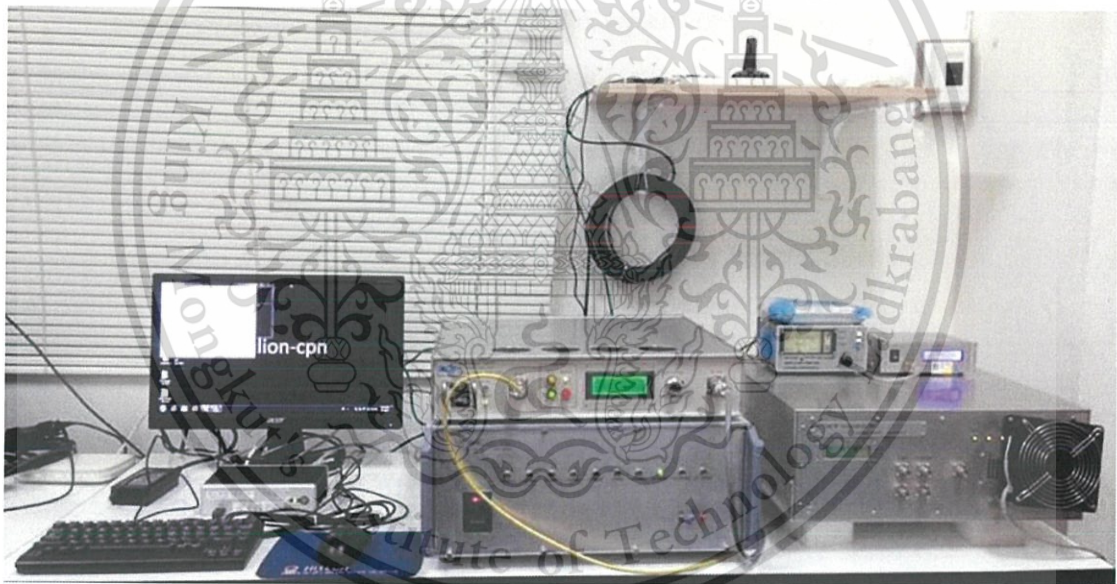


Figure 2.13 A result of the NeQuick 2 model after submitting the model inputs.

2.7 Chumphon station

Chumphon is a province in the south of Thailand. Since 2003, a frequency modulated-continuous wave (FMCW) ionosonde has been used to observe and monitor the ionospheric variations at Prince of Chumphon, King Mongkut's Institute of Technology Ladkrabang, Thailand (geographic latitude 10.72°N, longitude 99.37°E, and magnetic dip latitude 3.00°N) where it locates near to the equatorial latitude as well as magnetic equator. The FMCW ionosonde at Chumphon station is one of the 8 SEALION (South East Asia Low-Latitude Ionospheric Network) ionosondes (Maruyama et al., 2007) covering Asia Pacific region around meridional longitude 100°E near the magnetic equator. Note that SEALION is a joint project among the institutes and countries, for instance, National Institute of Information and Communications Technology (NICT), Japan, King Mongkut's Institute of Technology Ladkrabang (KMITL), Thailand, Chiang Mai University (CMU), Thailand, National Institute of Aeronautics and

Space (LAPAN), Indonesia, Hanoi Institute of Geophysics (HIG), Vietnam, Vietnamese Academy of Science and Technology, Vietnam, Center for Space Science and Applied Research, China, Chinese Academy of Sciences, China, and Kyoto University, Japan. These stations have monitored ionospheric variations in Asia-Pacific region near magnetic equator. The equipment implemented at Chumphon station include FMCW ionosonde, GNU Radio Beacon Receiver (GRBR) of Kyoto University, GPS receiver of JAXA (Japan Aerospace Exploration Agency), and JAVAD GPS receiver as shown in Figure 2.14 (a)-(d), respectively. Chumphon station is located within the EIA regions. EIA, discovered by Appleton (1954), is a phenomenon in F layer at low latitude which is caused by fountain effect. The EIA is identified by an electron density trough at the magnetic equator as well as two electron density peaks at around 15 degrees north and south as described previously in Section 2.2.3.

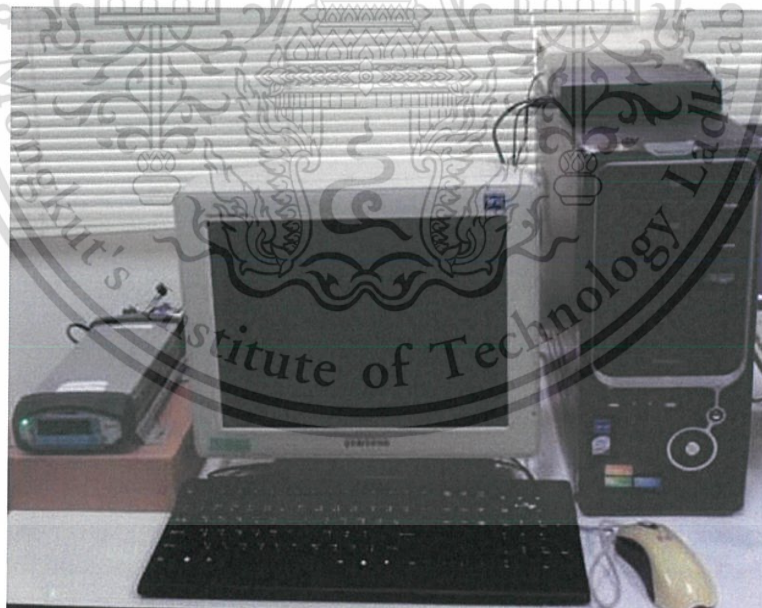


(a) FMCW Ionosonde

Figure 2.14 The equipment implemented at Chumphon station.



(b) GNU Radio Beacon Receiver (GRBR) supported by Kyoto University, Japan

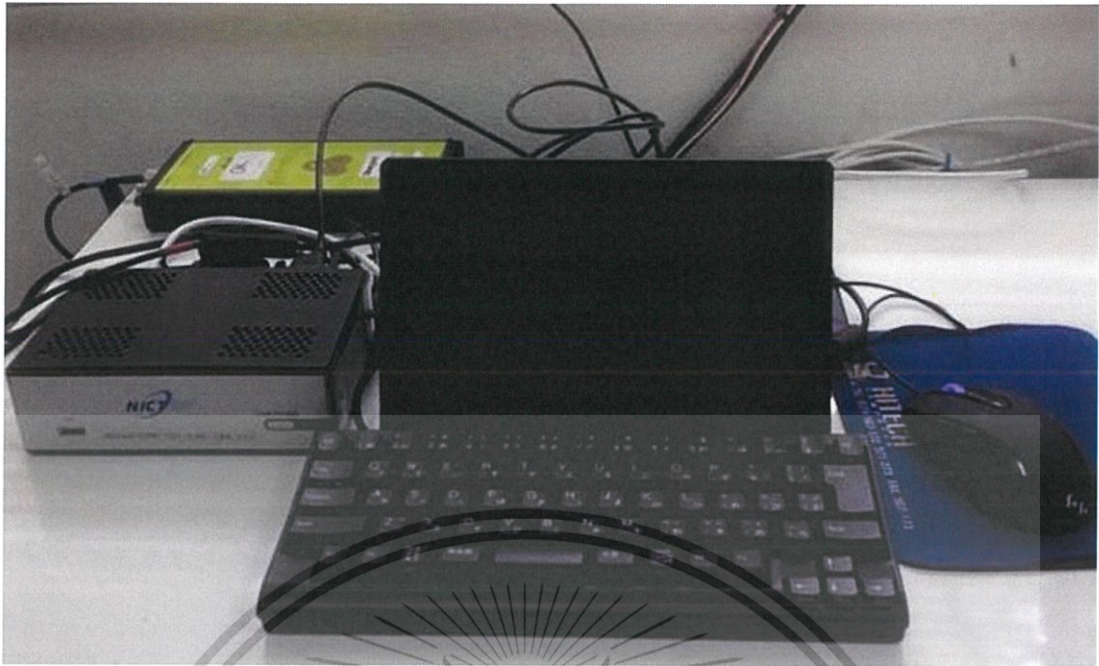


(c) GPS Receiver with Trimble supported by JAXA, Japan

Figure 2.14 The equipment implemented at Chumphon station (continue).

This material is reserved for educational use only, not allowed for commercial use.

Forbidden to modify the content, and cite the document when use.



(d) JAVAD GPS Receiver supported by NICT, Japan

Figure 2.14 The equipment implemented at Chumphon station (continue).

CHAPTER 3

GPS SYSTEM

This chapter describes about global positioning system (GPS) system. Principles of GPS system including the elements of GPS system and structure of GPS code are described in Section 3.1. GPS receiver and RINEX format are addressed in Section 3.2. Finally, ionospheric delay, TEC and slab thickness computations are described in Section 3.3. Note that the VTEC values from JAVAD GPS receiver at Chumphon station during 2004-2006 are used only in this thesis. However, the details of Global Navigation Satellite System (GNSS) should be explained shortly at this point. The GNSS is a satellite system which is extensively used for navigation systems. There exist several current GNSS systems such as the United States' Global Positioning System (GPS), the Russian Federation's Global Orbiting Navigation Satellite System (GLONASS), and the Europe's GALILEO. The GNSS has been used in various applications, for instance, land surveying, precision farming, vehicle tracking, and navigation systems. The details of GPS system are described as follows.

3.1 Principles of GPS

3.1.1 Background of GPS system

Global Positioning System (GPS) is a satellite-based positioning system that can provide people with their exact positions on Earth, tells them how to get to another location, how fast they are moving, and what time it is, etc. GPS system was originally designed to help the United States military under GPS project in 1973 for seeking the accurate locations of their soldiers, vehicles, planes and ships around the world. The GPS system is used in several applications for military, civilian and commercial users around the world, such as, cellular phones, emergency services, navigation, etc. It is also used in several scientific researches. For instance, the meteorologists use GPS system to forecast the space weather and the geologists use

This material is reserved for educational use only, not allowed for commercial use.

GPS system to measure earthquake motion. Operated by the U.S. Department of Defense (DoD), NAVSTAR (NAVigation Satellite Timing and Ranging) GPS provides continuously real-time and 3-dimensional positioning, navigation and timing. Any person with a GPS receiver can access the GPS system and provides location coordinates for any applications. GPS system consists of three segments, i.e., 1) the space segment: GPS satellites, 2) the user segment, including military and civilian users, and 3) the control segment, operated by the U.S. military, as shown in Figure 3.1.

1) Space Segment consists of 24 GPS satellites circling the earth every 12 hours at 20,200 km (12,600 miles) in altitude. The first GPS satellite was launched by the U.S. Air Force in early 1978. Nowadays, there are at least 24 GPS satellites orbiting the Earth at altitude about 11,000 nautical miles. There are at least 4 satellites in each of 6 orbital planes and each plane is inclined 55 degrees relative to the equator as illustrated in Figure 3.2. Hence, the GPS satellites cross the equator with tilted angle of 55 degrees. The orbits are separated by 60 degrees to cover the complete 360 degrees.

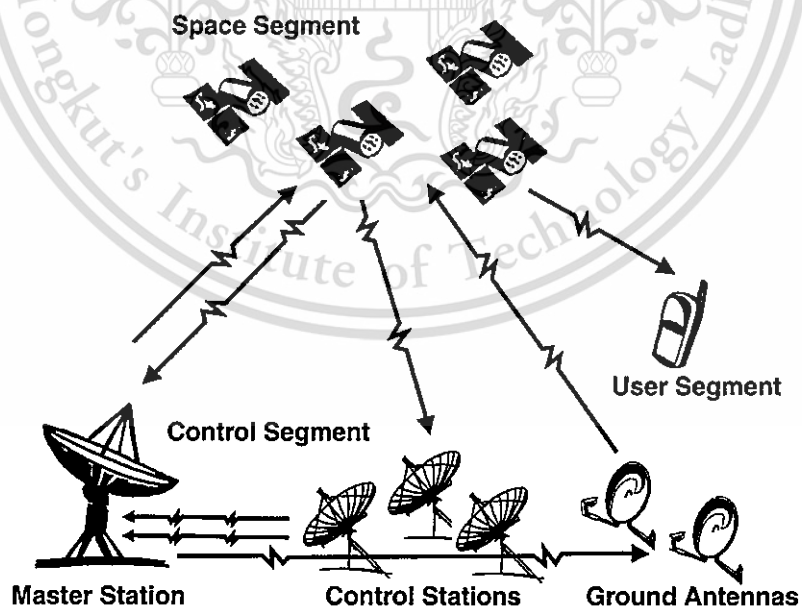


Figure 3.1 Three segments of GPS system.

(<https://shivkumardas.files.wordpress.com/2013/07/segments-of-gps.jpg>)

This material is reserved for educational use only, not allowed for commercial use.

Forbidden to modify the content, and cite the document when use.

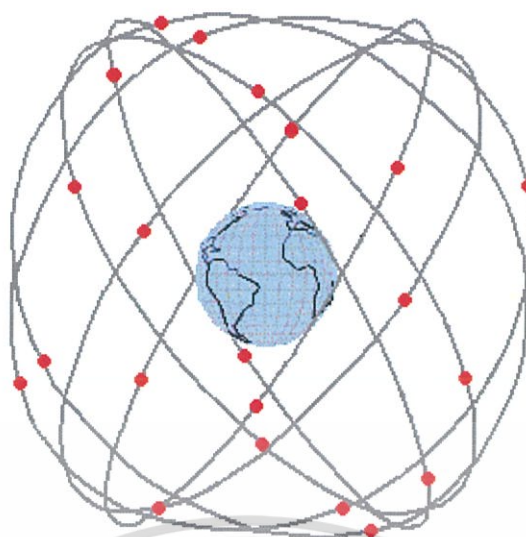


Figure 3.2 GPS Constellation including GPS satellites and 6 orbital planes.
 (<http://www.montana.edu/gps/understd.htm>)

The high altitude insures that the satellite orbits are stable, precise and predictable, and that the satellites' movements are not affected by atmospheric drag. GPS satellites take about 12 hours for completing an orbit, hence, they pass over any points on the Earth about twice a day. Note that the satellites rise (and set) about 4 minutes earlier each day. The GPS satellites are powered primarily by sun-seeking solar panels and use NiCad batteries as secondary power supplies. Each GPS satellite has 4 atomic clocks, but only one atomic clock is in use at a time. These highly accurate atomic clocks enable GPS to provide the most exact timing system.

2) User segment consists of military and civilian GPS users and their GPS receivers. The U.S. military division employs the GPS system for navigation, reconnaissance, and missile guidance systems. GPS applications for civilian users have been establishing and developed as military uses, and have been extended to apply in many tasks beyond original expectations. There are several civilian applications for GPS, such as, navigation, timing, mapping, agriculture, surveying, transportation, and natural resource management, etc.

3) Control segment is responsible for proper operations of the GPS system, such as, tracking the GPS satellites, providing the GPS satellites with the corrected orbit and time information. It is sometimes called as ground segment. The GPS

This material is reserved for educational use only, not allowed for commercial use.

Forbidden to modify the content, and cite the document when use.

Control Segment consists of a network of monitor station (MS), master control station (MCS), a backup of the MCS, and a network of four ground antenna (GA).

The MCS process the measurements received by the MSs, estimate satellite orbits (ephemerides) and clock errors, as well as generate the navigation message. The correction and navigation messages are uploaded to the satellites via the ground antennas. The MCS locates at Falcon Air Force Base in Colorado Springs, controlled and maintained by the U.S. Department of Defense. Meanwhile, there are 4 other monitor stations located in Hawaii, Ascension Island, Diego Garcia and Kwajalein. These stations need to measure the satellite orbits exactly. Any discrepancies between actual orbits and forecasted orbits are transmitted back to the satellites. The satellites can then broadcast these corrections along with position and timing data, hence, GPS receiver on the Earth can precisely know and track the location of each satellite.

The main tasks of the Control System are as follows. 1) Monitoring and controlling of satellite orbital parameters, 2) Monitoring health and status of the satellite subsystems, and 3) Updating several parameters, i.e., ephemeris, almanac and clock corrections, in the navigation message. Some applicable examples of GPS technology in agriculture and navigation are increasing rapidly as follows.

1. Soil Gathering: Gathering soil samples across vary large land are able to be organized using GPS and mapping software. The sample locations can be pointed in the farms and marked on the mapping software.

2. Tractor Guidance: If the farmers plough their farms with a recording GPS system, then the programmed tractor can follow the routes for cultivating and harvesting, etc.

3. Computing and Modeling of ionospheric TEC: Exact modeling of ionospheric TEC is an important task of positioning, navigation, and timing (PNT) services needed for Global Navigation Satellite System (GNSS), space weather prediction, Earth Observation System (EOS), and satellite-based communication systems.

Moreover, the position of any points can be found using the distances measured from this desired point to some known positions. A simple example for finding the desired position is illustrated as a one dimensional representation as

shown in Figure 3.3 where a user position is assumed on a line. If the satellite position (S_1) is known and the distance (x_1) from S_1 to the user position (U) is also known. However, the user positions might locate either on the left hand or on the right hand of S_1 . Therefore the distance from another satellite with known position to a user position must be measured and considered to calculate the user position. Here, another known position of S_2 and another distance of x_2 are specified additionally to calculate the user position U as shown in Figure 3.3.

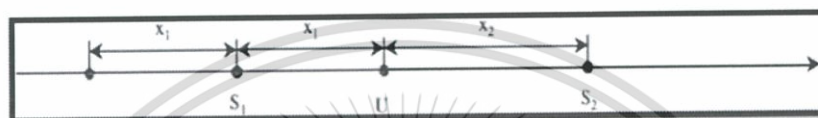


Figure 3.3 An idea for finding the user position in one dimensional representation.

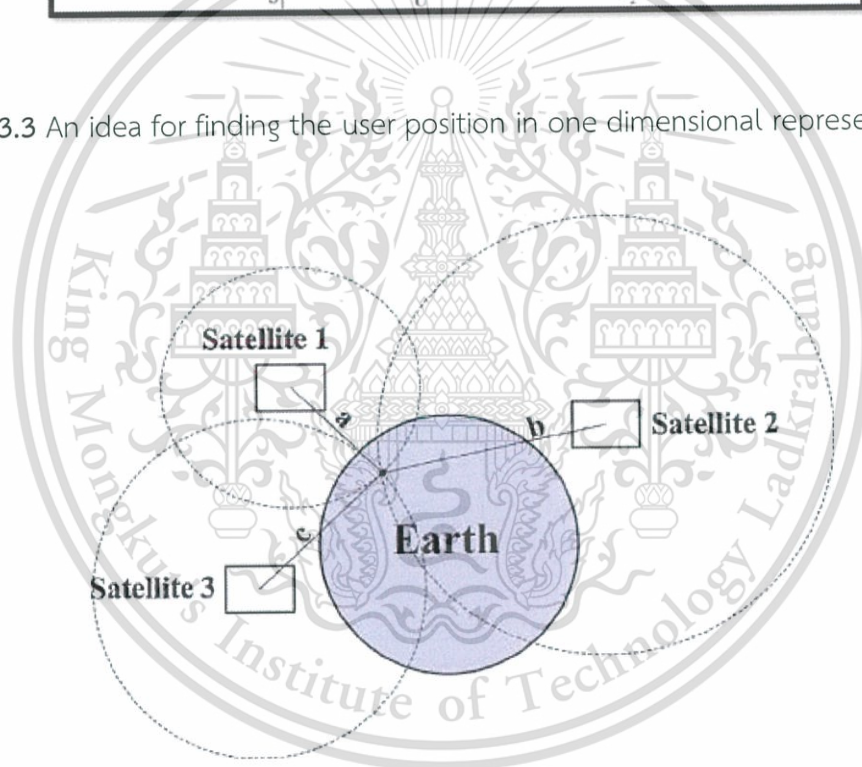


Figure 3.4 Two dimensional trilateration for finding the user position on the Earth. (Lowe and ÓLaighin, 2013)

Another example for finding the desired position is two dimensional trilateration as illustrated in Figure 3.4. Here, three satellites and three distances are needed to calculate a user position on the Earth. Two traces with constant distances to the user position are made two dependent circles. Here two satellites and two distances are needed to calculate a user position on the Earth. This material is reserved for educational use only, not allowed for commercial use.

distances provide 2 possible points due to the intersection of two circles. A third circle is needed additionally to compute the user position on the Earth. A trace with a constant distance of the third circle passing through a lower intersected point of the two satellites can triangulate the user position on the Earth as shown in Figure 3.4. In theory, the position of each GPS satellite can be known from the ephemeris data transmitted by that GPS satellite. The distances from any GPS receivers to a satellite can be measured, hence, the position of the desired GPS receiver can be computed. Although the measured distances have some errors inherently, at least three satellites can be used to calculate the desired user position.

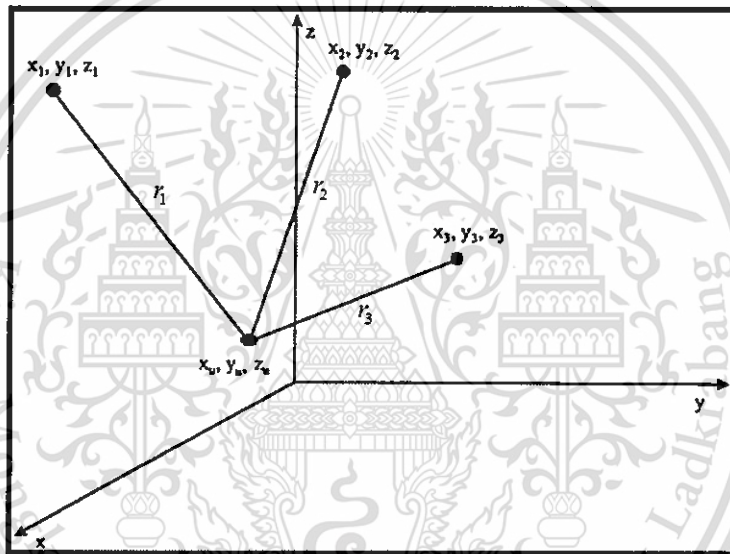


Figure 3.5 Computing one unknown position with the use of three known positions.

(<https://www.slideshare.net/wasim1akram000/>)

In Figure 3.5, there are three known points at locations (x_1, y_1, z_1) , (x_2, y_2, z_2) , and (x_3, y_3, z_3) , and an unknown point at (x_u, y_u, z_u) . If the distances between the three known points to the unknown point are specified as r_1 , r_2 , and r_3 , hence, these three distances can be computed as follows.

$$r_1 = \sqrt{(x_1 - x_u)^2 + (y_1 - y_u)^2 + (z_1 - z_u)^2} \quad (3.1)$$

$$r_2 = \sqrt{(x_2 - x_u)^2 + (y_2 - y_u)^2 + (z_2 - z_u)^2} \quad (3.2)$$

$$r_3 = \sqrt{(x_3 - x_u)^2 + (y_3 - y_u)^2 + (z_3 - z_u)^2} \quad (3.3)$$

This material is reserved for educational use only, not allowed for commercial use.

Forbidden to modify the content, and cite the document when use.

It is worthy to note here that at least four GPS satellites are used for computing the receiver bias for TEC computation.

3.1.2 Structure of GPS code

GPS satellites broadcast satellite position and timing data continuously using two radio signals on different frequencies: L1 and L2. Two radio signals travel at the speed of light and take about 0.0673 second to reach the Earth. The center frequencies of L1 and L2 are equal to 1575.42 MHz and 1227.6 MHz, respectively. These two frequencies are coherent with a GPS clock frequency of 10.23 MHz as follows.

$$L1: 1575.42 \text{ MHz} = 154 \times 10.23 \text{ MHz} \quad (3.4)$$

$$L2: 1227.6 \text{ MHz} = 120 \times 10.23 \text{ MHz} \quad (3.5)$$

Two kinds of code broadcast for each GPS satellite on the L1 frequency: C/A (Coarse Acquisition) code and P (Precision) code. C/A code is available to civilian GPS users and provides standard positioning service (SPS). For utilizing the SPS, one can fulfill 15 meter horizontal accuracy 95% of the time. The coordinates reading from a display unit of GPS receiver will be within 15 meters of the true position on the Earth during 95% of the time. Meanwhile, P code broadcasts on both L1 and L2 frequencies. P code is used for precise positioning service (PPS) and is available only to the military GPS users. For utilizing P code, a military GPS receiver can achieve better positioning accuracy than a civilian GPS receiver. Additional methods can be used to increase the positioning accuracy of both C/A code and P code for a GPS receiver. The C/A code for civilian user transmits data at 1.023 million chips per second, whereas the P(Y) code for U.S. military user transmits at 10.23 million chips per second. GPS frequencies and code usages are shown in Table 3.1. Moreover, some GPS receiver manufacturers have incorporated the capability to receive both GPS and GLONASS signals. This increases the availability of satellites and the integrity of combined system. However, the GPS satellite signals require a line-of-sight path

This material is reserved for educational use only, not allowed for commercial use.

Forbidden to modify the content, and cite the document when use.

toward GPS receivers and they cannot penetrate soil, walls, water, etc. The details of the coarse acquisition (C/A) code and the precision (P(Y)) code are as follows.

(1) C/A code - The C/A code is also a diphase signal which is modulated with a chip rate of 1.023 MHz. Each chip is about 977.5ns or 1/1.023 MHz. The transmitted C/A code contains a main lobe and several side lobes. The total period of C/A code contains 1,023 chips and a chip rate is equal to 1.023 MHz, hence, the C/A code is 1 ms long. The transmitting bandwidth of the GPS satellite in the L1 frequency is about 20 MHz so as to accommodate the P(Y) code signal.

Table 3.1 GPS frequencies and code usages.

Band	Frequency (MHz)	Phase	Original Usage	Modernized Usage
L1	1,575.42 (10.23 × 154)	In-Phase (I)	Encrypted Precision P(Y) code	
		Quadrature-Phase (Q)	Coarse-acquisition (C/A) code	L1 Civilian and Military code
L2	1,227.60 (10.23 × 120)	In-Phase (I)	Encrypted Precision P(Y) code	
		Quadrature-Phase (Q)	Unmodulated carrier	L2 Civilian code and Military code
L3	1381.05 MHz	Used for nuclear detonation (NUDET) detection.		
L4	1379.913 MHz	Being studied for additional ionospheric correction.		
L5	1176.45 MHz	Proposed for use as a civilian safety-of-life (SoL) signal.		

Source: <http://www.novatel.com/assets/Documents/papers/GLONASSOverview.pdf> and https://en.wikipedia.org/wiki/Global_Positioning_System

(2) P(Y) code - The P(Y) code is diphase signal which is modulated with a chip rate of 10.23 MHz. P(Y) code is encrypted particularly for using only in military applications. The chip length is equal to about 97.75 ns or 1/10.23 MHz. The P(Y) code is generated from two pseudorandom noise (PRN) codes with the same chip rate. This material is reserved for educational use only, not allowed for commercial use.

Forbidden to modify the content, and cite the document when use.

rate. One PRN sequence has 15,345,000 chips, which has a period of 1.5 seconds, and another one has 15,345,037 chips with a difference of 37 chips. These two numbers, 15,345,000 and 15,345,037, are used as some relative primes. Hence, the code length generated by these two codes is equal to 23,017,555.5 seconds ($1.5 \times 15,345,037$) in which it can be used longer than 38 weeks. However, the actual length of the P(Y) code is employed only one week, since the P(Y) code is reset every week. The 38-week code length is divided into 37 different P(Y) codes and each satellite can use a different portion of these different P(Y) codes. The 32 P(Y) codes are assigned for satellite identification numbers and the remains are reserved for general purposes. Further details of code structure for GPS system can be studied at a web site https://en.wikipedia.org/wiki/Global_Positioning_System.

3.2 GPS receiver and RINEX format

3.2.1 GPS receiver

Nowadays, there are lots of GPS receivers which are produced by many manufacturers. Most of modern GPS receivers are built as digital GPS receivers. They are designed with different models, functions and prizes, but they generally work in the same basic functions of GPS receiver. The GPS-TEC data studied in this thesis are obtained from a GPS receiver at Chumphon station, so the details of this GPS receiver are only described in this thesis.

A digital GPS receiver used at Chumphon station is manufactured by JAVAD GNSS Inc. whose block diagram is shown in Figure 3.6. The radio signals from all GPS satellites are received by an antenna and amplified by a pre-amplifier (Preamp). Then, the amplified RF signals are down-converted to an intermediate frequency (Analog IF) with local oscillators (LOs). Note that the LOs are produced from the local reference oscillator. The Analog IF is transmitted to A/D converter and then divided into 2 paths: the first path for using in automatic gain control (AGC) and the second path for converting it to be a digital IF and sent it to digital receivers. Each receiver channel is assigned to a single satellite and the multiple receiver channels can be processed simultaneously using a multiplexor (if any).

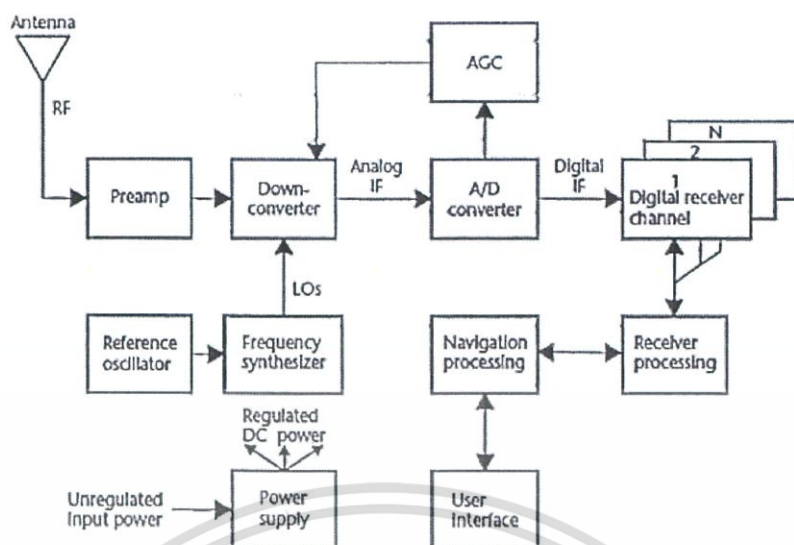


Figure 3.6 Block diagram of a JAVAD GPS receiver used at Chumphon station.

(http://www.javad.com/downloads/javadgnss/manuals/hardware/Delta_operators_Manual.pdf)

Moreover, the digital receivers consist of several channels from 1 to N, and these digital receiver channels are processed in GPS Receiver Processing module and Navigation processing module. Navigation processing is linked to user directly via User Interface module.

3.2.2 RINEX format

RINEX (Receiver Independent Exchange) format was developed by the Astronomical Institute of the University of Berne so as to exchange the GPS data. The original RINEX was presented by Gurtner et al. (1989) in the 5th International Geodetic Symposium on Satellite Positioning. The RINEX format version 2 is used in this thesis for acquiring the GPS data file at Chumphon station and consists of three ASCII file types, i.e., observation data file, navigation message file, and meteorological data file. All of these data files consist of a header section and a data section. The header section is placed at the beginning of the file and contains global information. The header section contains header labels in columns 61-80 for each line. The RINEX format has been improved so as to minimize the space requirements and be independent from the number of different observation types of a specific GPS receiver system. Here, both the types of observations stored in the GPS receiver and

the satellite systems observed are identified in the header section. In general, both the observation data file and the meteorological data file contain the data from one location and one session. If data from more than one GPS receiver must be exchanged, it would not be economical to collect the identical satellite messages from different GPS receivers in many times. Hence, the navigation message file from one GPS receiver might be exchanged. The RINEX navigation file generally broadcasts to any users as a part of the GPS signal in the navigation message, but the RINEX meteorological data file is not used at the Chumphon station. Also, the RINEX format version 2 can be accessed at <http://igsceb.jpl.nasa.gov/igsceb/data/format/rinex2.txt>.

3.3 Ionospheric delay, TEC and slab thickness computations

A main contribution of this thesis is to propose a new expression for computing the NeQuick bottomside thickness parameter (B2bot) in which the vertical TEC and the slab thickness are two main parameters for computing this new expression as described in Chapter 4. Therefore, computing ionospheric delay, TEC and the slab thickness are explained in this section.

3.3.1 Ionospheric delay computation

When considering the electromagnetic wave in space with a wavelength λ and a frequency f , the phase velocity is represented by

$$V_{ph} = \lambda f \quad (3.1)$$

Hence, the carrier frequencies of GPS satellite (L1 and L2) propagate with different phase velocities. Moreover, the group velocity is also taken to use for considering code pseudorange of GPS system (Hofmann-Wellenhof et al., 1994). The group velocity is computed by

$$V_{gr} = -\frac{df}{d\lambda} \lambda^2 = V_{ph} - \lambda \frac{dV_{ph}}{d\lambda} \quad (3.2)$$

Since the ionosphere layer is a dispersive medium, the refractive index of this layer is a function of frequency and the group velocity differ from the phase velocity. In contrast to a non-dispersive medium, the group velocity is equal to the phase velocity. Theoretically, these velocities depend on the refractive index η and the light velocity c . Hence, the group and phase velocities can also be computed by (3.3) and (3.4), respectively.

$$V_{ph} = \frac{c}{\eta_{ph}} \quad (3.3)$$

$$V_{gr} = \frac{c}{\eta_{gr}} \quad (3.4)$$

Hofmann-Wellenhof et al. (1994) revealed that the group and phase refractive indices of a GPS signal can be shown in forms of (3.5) and (3.6), respectively. Note that the equations of group and phase refractive indices are the same, but they have different signs.

$$\eta_{ph} = 1 - \frac{40.3N}{f^2} \quad (3.5)$$

$$\eta_{gr} = 1 + \frac{40.3N}{f^2} \quad (3.6)$$

From the above equations, the group refractive index is higher than the phase refractive index, hence, the group velocity is less than the phase velocity. The different velocities lead to group delay and phase advance in a GPS signal. Moreover, code pseudorange measurement of GPS system also causes the time delay and phase advance. Therefore, the measured code pseudorange is longer than the actual geographic distance between a satellite and a GPS receiver. Meanwhile, the measured carrier phase is shorter than the actual distance. The differences between the measured range and the actual range in a straight line (ΔL) can be calculated by

$$\Delta L_{ph} = \frac{-40.3}{f^2} \text{TEC} \quad (3.7)$$

$$\Delta L_{gr} = \frac{40.3}{f^2} \text{TEC} \quad (3.8)$$

where TEC is defined as the integration of electron density along a signal path from a satellite to a GPS receiver (electrons/m²) and f is the frequency. Here, the TEC value is defined as the electron in a column of 1 m² cross-section from a satellite to a GPS receiver.

Hofmann-Wellenhof et al., 1994 proposed that the propagation times of L1 and L2 toward a receiver are different because of different refractive indices as shown in (3.5) and (3.6). Considering (3.8) and applying a relationship among the distance, the velocity, and the time: $s = ut$, therefore, the ionospheric time delay (I) can be computed by

$$\frac{\Delta L_{gr}}{c} = I = \frac{40.3}{cf^2} \text{TEC} \quad (3.9)$$

$$I = \frac{1.345 \times \text{TEC} \times 10^{-7}}{f^2} \quad (3.10)$$

where ΔL_{gr} is a difference between the actual distance and the direct distance from a satellite to a GPS receiver and c is a light velocity.

The diurnal variations in the observed TEC, the IRI TEC, and the IGS TEC are shown again in this chapter. The aims are to show how the diurnal variations in these three TEC values correspond to those in their ionospheric delays and to illustrate the diurnal variations in absolute differences of TEC as well. Moreover, two absolute differences among the studied TEC values are also considered in this thesis. Firstly, the D_{A^*} (unit: TECU) is defined as the absolute differences between the observed TEC and the IRI TEC or the IGS TEC at Chumphon in 2015 for all three seasons, i.e., winter, equinox, and summer. The D_{A^*} can be computed by

$$D_T^* = |\text{TEC}^* - \text{TEC}_{\text{obs}}| \quad (3.11)$$

where the TEC^* denote IRI TEC or IGS TEC that make D_T^* represent D_IRI or D_IGS , respectively.

Secondly, the Delta_I^* (unit: ns) is defined as the absolute differences between the observed ionospheric delays and the IRI or IGS ionospheric delays at Chumphon in 2015 for all three seasons. The Delta_I^* can be expressed by

$$\text{DeltaI_I}^* = |I^*_I - \text{Obs_I}| \quad (3.12)$$

where the I^*_I denote IRI_I or IGS_I that make Delta_I^* represent Delta_IRI or Delta_IGS , respectively.

Here, the IRI TEC in 2015 are retrieved from the IRI-2012 model. The IRI-2012 web site can be accessed at http://omniweb.gsfc.nasa.gov/vitmo/iri2012_vitmo.html. Moreover, the IGS TEC in 2015 are retrieved from the International GNSS service via the IGS homepage at <ftp://cddis.gsfc.nasa.gov/gps/products/ionex>.

3.3.2 TEC Computation

As described in above section, the ionospheric time delay (I) can be computed using (3.10). Hofmann-Wellenhof et al., 1994 proposed that a difference in time delays of $L1 = 1.57542$ GHz and $L2 = 1.22760$ GHz passing through ionosphere can be used for computing TEC, i.e.,

$$\Delta I = I_{(f_1)} + I_{(f_2)} \quad (3.13)$$

Replacing ΔI in (3.13) with the I in (3.10), hence,

$$\Delta I = 134.5 \times \text{TEC} \left[\frac{1}{f_1^2} - \frac{1}{f_2^2} \right] \quad (3.14)$$

Rearranging (3.14) in a form of TEC, therefore, an equation of TEC (Unit: electrons/m²) is obtained as follows.

$$\text{TEC} = \frac{\Delta I}{134.5} \left[-\frac{(f_1 f_2)^2}{f_1^2 - f_2^2} \right] \quad (3.15)$$

Since the TEC can be computed by using several approaches, an algorithm used to compute TEC here is to use the difference between the pseudoranges (P_1 and P_2) and the difference between the phases (L_1 and L_2) of two frequencies of GPS system (Blewitt, 1990) as shown in (3.16) and (3.17), respectively.

$$\text{STEC}_P = \frac{2(f_1 f_2)^2}{k(f_1^2 - f_2^2)} (P_2 - P_1) \quad (3.16)$$

$$\text{STEC}_L = \frac{2(f_1 f_2)^2}{k(f_1^2 - f_2^2)} (L_1 \lambda_1 - L_2 \lambda_2) \quad (3.17)$$

where k is the refractive index of ionosphere of $80.62 \text{ m}^3/\text{s}^2$, λ_1 and λ_2 are the wavelengths relating to f_1 and f_2 , respectively. TEC is replaced with STEC (Slant TEC) since TEC is measured in the slant path (real path) from a GPS receiver and a satellite. Note that the STEC is defined as the line integral of the electron density from a GPS satellite to the GPS receiver above a user-defined elevation angle (usually 45°).

In fact, the TEC used by several researchers is a vertical TEC (VTEC). The VTEC is measured directly from a receiver to a satellite with zenith angle (χ) of 0. Figure 3.7 show a relationship between STEC to VTEC. A point which GPS signals pass through ionosphere is called ionospheric pierce point (IPP). IPP is used to identify an VTEC coordinate on map. However, when there exist a few GPS receivers, the number of IPP's cannot cover all desired regions. Hence, it is very important to apply a model to interpolate other coordinates in uncovered regions.

At Chumphon, Thailand, a dual-frequency GPS receiver is used with different frequencies, i.e., $f_1 = 1575.42$ MHz and $f_2 = 1227.60$ MHz. The GPS TEC measurement system at Chumphon is composed of an antenna, an amplifier, a JAVAD TEC meter with a GPS receiver, and a computer. The GPS receiver embedded in the JAVAD TEC meter receives the GPS signals continuously ranging from 4 to 12 signals and then computes the STEC values with (3.16) and (3.27), respectively. The VTEC (unit: eU/m^2) is based on some computational equations of Ma and Maruyama (2003) as shown in (3.18).

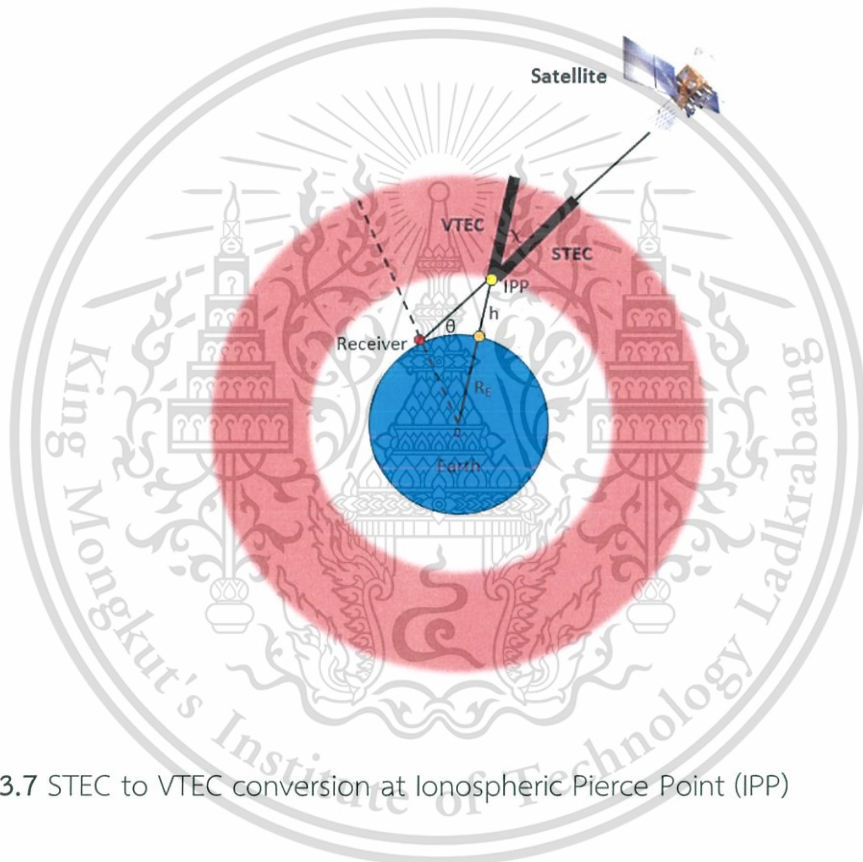


Figure 3.7 STEC to VTEC conversion at Ionospheric Pierce Point (IPP)

$$\text{VTEC} = \text{STEC} \times \cos \chi \quad (3.18)$$

Here, the zenith angle (χ) is computed by

$$\chi = \arcsin \left(\frac{R_E \cos \alpha}{R_E + h} \right), \quad (3.19)$$

This material is reserved for educational use only, not allowed for commercial use.

Forbidden to modify the content, and cite the document when use.

where R_E is the average radius of the Earth, α is the elevation angle of the satellite, and h is the height of ionosphere layer which is assumed to be equal to 400 km. Moreover, Ma and Maruyama (2003) proposed that both the satellite bias and the receiver bias should be included in (3.18) so as to calculate the absolute TEC. Hence, (3.18) can be rewritten as

$$\text{VTEC} = (\text{STEC} - b_s - b_r) \times \cos \chi, \quad (3.20)$$

where b_s is the estimated satellite bias and b_r is the estimated receiver bias.

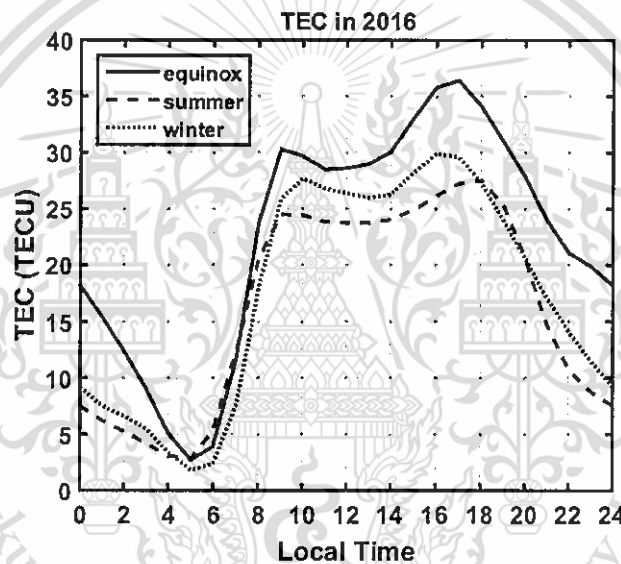


Figure 3.8 The diurnal variations in IRI TEC values at Chumphon station in 2016.

Figure 3.8 shows the diurnal and seasonal variations in IRI-2012 TEC values at Chumphon station in 2016. The diurnal variations in TEC for all seasons have the same trends; they start increasing at 05 LT and reach the minor peaks during 09 – 10 LT. Then, they decrease from 11 to 13 LT (bite-out phenomena) and increase again to reach the main peaks during 16 – 18 LT. Kenpankho et al. (2011) revealed The noon bite-out phenomenon are found obviously on the IRI-2007 TEC, but not on both the IGS TEC and GPS TEC values. The maximum value is found in equinox at 17 LT about 36.5 TECU, whereas the minimum value is found in winter at 05 LT about 2 TECU. This material is reserved for educational use only, not allowed for commercial use.

TECU. TEC values usually decrease sequentially in equinox, winter, and summer seasons, excluding during 05 – 08 LT. TEC values in daytime are higher than those in nighttime with the minimum values at 05 LT for all seasons in 2016. Figure 3.9 shows the yearly variations in IRI TEC values (unit: TECU) at Chumphon station in each day from 2014 to 2016. We can see that the TEC variations in each year always are minimum values in December solstice and June solstice. Meanwhile, they are maximum values in March equinox and September equinox. The TEC values decreases orderly from 2014 to 2016 regarding to the decreasing solar activities. Note that the average sunspot numbers (Rz12's) are 110, 69.9, and 43.5 for year 2014, 2015, and 2016, respectively.

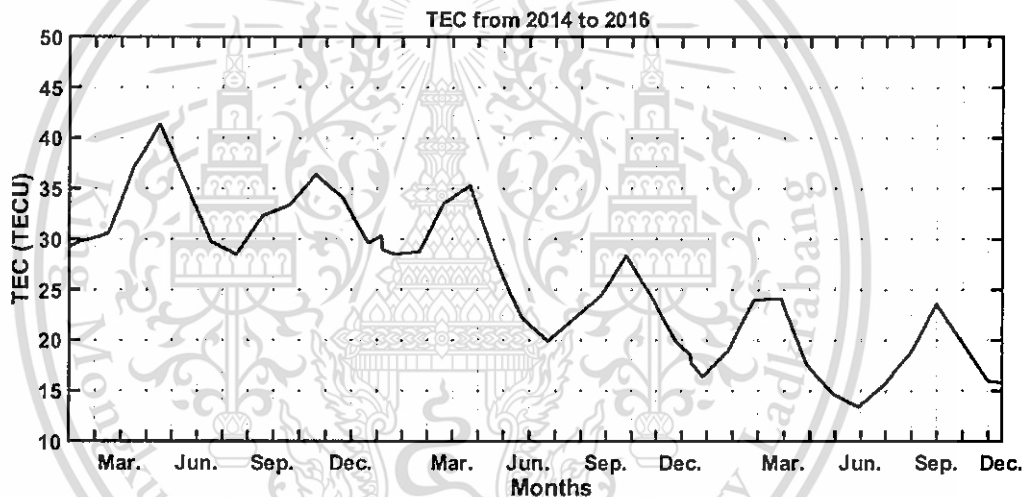


Figure 3.9 The yearly variations in IRI TEC values at Chumphon station in each day from 2004 to 2016.

3.3.3 Slab thickness computation

The equivalent slab thickness (τ) is a crucial parameter for ionospheric observation because it covers the TEC in both topside and bottomside ionospheres as depicted in Figure 3.10 (Stankov and Warnant, 2009). It is considered as the depth of an imaginary ionosphere whose TEC has the same value as the actual ionosphere and a uniform electron density is equal to the maximum electron density of the actual ionosphere (Chuo, 2007). It is used in the practical applications, for example,

time delay correction of radio wave propagation, neutral temperature measurement, and scale height estimation of ionization constituents etc. Note that in Figure 3.10, the B_0 and the H_0 are the bottomside and topside thickness parameters, respectively. It is defined as the ratio of the TEC to the NmF_2 as shown in (3.21).

$$\tau = \frac{\text{TEC}}{NmF_2} \quad (3.21)$$

The study of slab thickness has been investigated by many researchers (e.g., Gulyaeva et al., 2004; Jin et al., 2007). They have found that the diurnal, seasonal, and solar activity variations of slab thickness show significant dependence on the location of observing station. During 1996-1999, the average diurnal value of seasonal variations is higher in the summer and is lower in the equinox at the equatorial ionization anomaly (EIA) region. The slab thickness values are generally higher during daytime hours (08-16 LT) and nighttime hours (20 - 04 LT) in the summer and winter than other times.

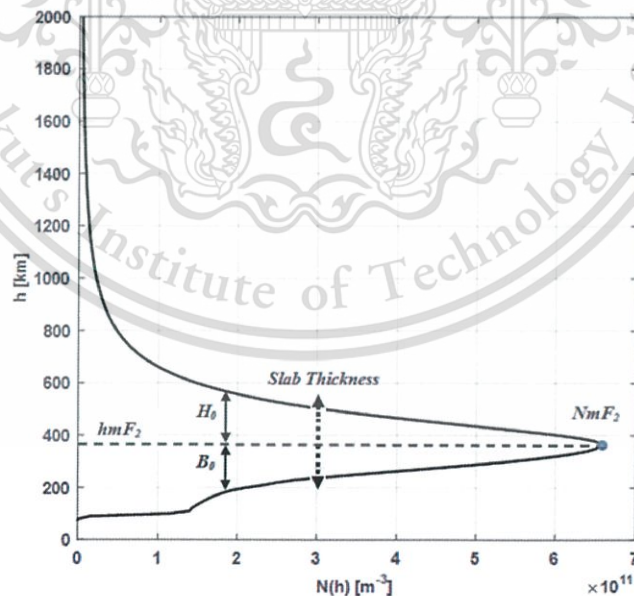


Figure 3.10 Equivalent slab thickness and its relations to B_0 as well as H_0 .

For example, at low latitude, it is about 239-344 km. At middle latitude, it is about 250-600 km and at high latitude, it can reach 1100 km during high solar activity (Iwamoto et al., 2002). Furthermore, Jayachandran et al. (2004) revealed that the variations of the slab thickness during the solar maximum and minimum phases of solar activity depend on their observation stations, including Hawaii (low latitude), Boulder (middle latitude), Goosebay (high latitude). In the mid-latitude, Minakoshi and Nishimuta (1994) show an apparent peak in during the pre-sunrise hours at the solar minimum phase as well as its disappearance while the sunspot number increases. This peak starts to exist again at the solar maximum phase, especially during winter. Moreover, the slab thickness is also higher at the post-sunset hours during different seasons in the low and middle latitudes. Kenpankho et al. (2011) studied about the diurnal and seasonal variations of TEC, NmF_2 , and slab thickness parameters at Chumphon during the low solar activity from 2004 to 2006. The experimental data used in their study are obtained from FMCW ionosonde and GPS-based TEC measurement at Chumphon station, a part of the South East Asia Low Latitude Ionosphere Observation Network (SEALION). The 12-month running mean relative sunspot numbers (Rz_{12} values) decrease orderly from 2004 to 2006.

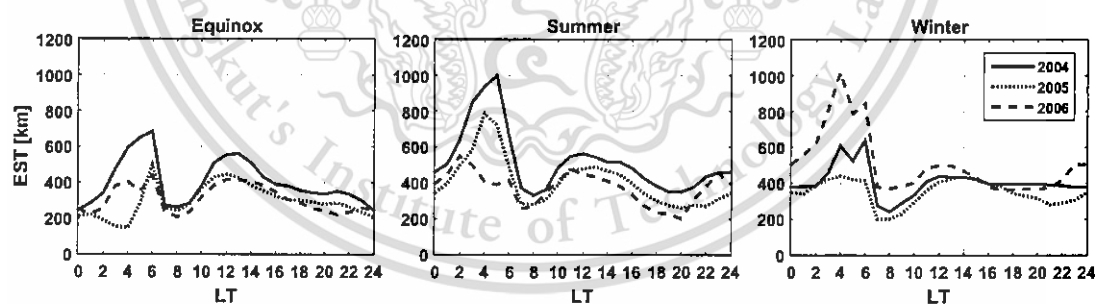


Figure 3.11 Diurnal variations of the slab thickness during three seasons from 2004 to 2006.

Figure 3.11 shows the diurnal and seasonal variations of the observed τ values during three seasons at Chumphon from 2004 to 2006. The variations in τ can be summarized as follows.

This material is reserved for educational use only, not allowed for commercial use.

Forbidden to modify the content, and cite the document when use.

1. The diurnal variations of slab thickness pattern have similar trends during these three years.
2. In the daytime, the τ values range from 200 km to 563 km for all seasons, while in the nighttime, they range from 145 km to 1,020 km.
3. The maximum value of slab thickness is 1,020 km for summer in 2004 with the maximum values occurring during pre-sunrise hours and the minimum values occurring during nighttime hours.
4. The pre-sunrise peaks can be seen when the F2 layer peak electron density is the lowest.
5. Two peaks during 03 – 06 LT (pre-sunrise hours) and around the local noon-time as well as two minima at around 08 LT and 21 LT (post-sunrise and sunset hours, respectively) can be seen.
6. The τ values are mostly greater during nighttime than those during daytime for all seasons.
7. For all three studied years, the average daily τ parameter is greater in the summer and lower in the equinox, the lowest values occur in the equinox of 2005.
8. Among all three years, the τ parameter is lower while the year increases, because of the higher solar activity in 2004 than 2005 and 2006, respectively.
9. Except for pre-sunrise hours of all three studied years, most of the slab thickness is generally lower as the year goes up, due to the higher solar activity in 2004 than 2005 and 2006, respectively. For all three seasons from 2004 to 2006, our study confirms the results of Jayachandran et al. (2004) for the slab thickness variation at low, middle, and high latitudes.

CHAPTER 4

COMPUTATIONS OF BOTTOMSIDE THICKNESS

It is well-known that four main ionospheric parameters which characterize the bottomside electron density profile (EDP) of the IRI model are $NmF2$, $hmF2$, $B0$, and $B1$. Both the $NmF2$ and the $hmF2$ can be computed by the empirical formula and the ionospheric data obtained from ground-based ionosonde measurement as described earlier in Chapter 2. On the other hand, the $B0$ and the $B1$ are not available from FMCW ionosonde at Chumphon station, therefore, computing ($B0$, $B1$) is an interesting task and should be computed so as to study the variations of the bottomside EDP over Chumphon station. The details for computing the bottomside thickness parameters of the NeQuick 2 model and the IRI model are explained in Section 4.1 – 4.3. Section 4.4 and Section 4.5 are devoted to describe the results and the discussions, respectively. The descriptions of each section are as follows.

4.1 Original bottomside thickness of the NeQuick 2 model

The NeQuick model, an evolution of Di Giovanni and Radicella (DGR) model, is based on the Epstein layer (Rawer, 1982) and represented by the following equation:

$$Ne_{NeQ}(h) = \frac{4NmF2}{\left(1 + \exp\left(\frac{h - hmF2}{B2bot}\right)\right)^2} \exp\left(\frac{h - hmF2}{B2bot}\right) \quad (4.1)$$

where $Ne_{NeQ}(h)$ is the F2 layer electron density at height h and the $B2bot$ (unit: km) can be computed by

$$B2bot = \frac{0.385 \times NmF2}{(dN/dh)_{max}} \quad (4.2)$$

This material is reserved for educational use only, not allowed for commercial use.

Forbidden to modify the content, and cite the document when use.

where the maximum of the electron density derivative with respect to height $(dN/dh)_{\max}$ (unit: $10^9 \text{ m}^{-3} \text{ km}^{-1}$) is computed using the empirical relation (Mosert de Gonzalez and Radicella, 1990)

$$\ln((dN/dh)_{\max}) = -3.467 + 1.714 \ln(foF2) + 2.02 \ln(M(3000)F2) \quad (4.3)$$

where $foF2$ is the F2 layer critical frequency (MHz) and $M(3000)F2$ is the propagation factor that is calculated by

$$M(3000)F2 = \frac{MUF(3000)F2}{foF2} \quad (4.4)$$

The $NmF2$ parameter can be computed using (Goodwin et al., 1995)

$$NmF2 = 1.24 \times (foF2)^2 \times 10^{10} \quad (4.5)$$

Finally, the $hmF2$ can generally be obtained from the scaled ionograms using the polynomial analysis program (POLAN) for ionosonde (Titheridge, 1985). In this thesis, the $hmF2$ is computed using the empirical formula of Bilitz et al. (1979) which is described previously in Chapter 2.

The $B2bot$ computed using (4.2) and (4.3) is the original bottomside thickness parameter of the NeQuick model, hence, it is designated as “ $B2bot_NeQ$ ” in this thesis. This $B2bot_NeQ$ has been calculated and analyzed by several researchers (e.g. Coisson et al., 2008; Wang et al., 2010; Jamjareegulgarn et al., 2015).

4.2 New proposed bottomside thickness of NeQuick 2 model

In fact, the $B2bot_NeQ$ equations in (4.2) and (4.3) were derived using data sources from Tucumán, San Juan, Buenos Aires and Ushuaia stations. Noontime profiles for various periods at high and medium solar activities are mostly considered. This material is reserved for educational use only, not allowed for commercial use.

Forbidden to modify the content, and cite the document when use.

San Juan data were only available on a bi-hourly basis and constituted the largest database for establishing this relation. The B2bot_NeQ equations in (4.2) and (4.3) have been accepted and used in the NeQuick 2 model (Nava et al., 2008), but a constant (0.385) for computing the B2bot_NeQ is needed to possibly update as revealed by Wang et al. (2010). Furthermore, these expressions are only based on the data from Argentinean stations, they might not be able to be used in Chumphon station, Thailand. Therefore, another new expression for computing the B2bot (namely, B2bot_Pro) is derived and described in this section as follows.

In the past, the median total electron content (TEC) data were obtained from radio signals of geostationary satellites at Florence and the median ionosonde data recorded at Rome were used to check and improve the capability of the DGR model so as to reproduce the electron density profile above the F2 peak. From Zhang et al. (1991), it was possible to simulate a topside shape parameter k which was computed from those ionosonde data and TEC values by the following analytical equation

$$\text{TEC} = 2(1+k)NmF2 \times \text{B2bot} \quad (4.6)$$

where only the F2 layer is considered, the B2bot is the bottomside thickness parameter of the NeQuick 2 model which is computed using (4.2), and the $NmF2$ are the F2 layer electron density peak that is computed using (4.5). The factor $2(1+k)$ where $k \neq 1$ is considered regarding to the asymmetry between the bottomside and the topside ionospheres of F2 layer. Moreover, the analytical equation (4.6) is derived from a numerical integration on the Epstein layer expression (4.1). The constant k has been improved as an empirical relation. The latest k is proposed by Coisson et al. (2006) and incorporated into the NeQuick 2 model. The latest k can be determined by

$$k = 3.22 - 0.0538foF2 - 0.00664hmF2 + 0.113 \frac{hmF2}{\text{B2bot}} + 0.00257Rz12 \quad (4.7)$$

Here, we set a new variable M to represent some terms in (4.7), except the $B2bot$, which is given by

$$M = 3.22 - 0.0538foF2 - 0.00664hmF2 + 0.00257Rz12 \quad (4.8)$$

Thus, the constant k can be rewritten to another form as

$$k = M + 0.113 \frac{hmF2}{B2bot} \quad (4.9)$$

The equivalent slab thickness (τ) can be computed using (Goodwin et al., 1995)

$$\tau = \frac{TEC}{NmF2} \quad (4.10)$$

It is worthy to note here that the τ is an important parameter for ionospheric observation and covers the TEC in the F2 layer at the height interval between the topside thickness ($H0$) and the bottomside thickness ($B2bot$) parameters of the NeQuick model. The $H0$ is computed by the multiplication between the k and the $B2bot$ as shown in Coisson et al. (2009). This means that the $B2bot$ is related to the τ and it might be determined from the τ if both the TEC and the $NmF2$ are known.

Substituting TEC from (4.6) in (4.10), then the τ can be written as

$$\begin{aligned} \tau &= \frac{TEC}{NmF2} = \frac{2(1+k)NmF2 \times B2bot}{NmF2} \\ &= 2B2bot + 2kB2bot \end{aligned} \quad (4.11)$$

Substituting k from (4.9) in (4.11) and rearranging the equation, we can obtain

$$\frac{\tau}{2} = B2bot + \left(M + 0.113 \frac{hmF2}{B2bot} \right) B2bot \quad (4.12)$$

Rearranging (4.12), a new equation of B2bot of the NeQuick 2 model, proposed in this thesis, is written as

$$B2bot = \frac{\tau/2 - 0.113hmF2}{1 + M}. \quad (4.13)$$

Note that the TEC used to compute the τ in (4.13) is the absolute vertical TEC (VTEC) which is described previously in Subsection 3.4.1. Moreover, the B2bot computed using (4.13) is the proposed bottomside thickness parameter in this thesis, hence, it is designated as “B2bot_Pro” in later.

Apart from the comparisons of the diurnal variations of bottomside thickness parameters, the percentage deviations among those bottomside thickness parameters are also studied in this thesis. The percentage deviations between the B2bot_Pro and other bottomside thickness parameters studied in this thesis are defined as

$$PD_{B^*} (\%) = \frac{|B^* - B2bot_Pro| \times 100}{B^*}. \quad (4.14)$$

where B^* are representatives of B2bot_NeQ, B0_ABT, and B0_Bil. PD_{B^*} are the percentage deviations corresponding to the replacement of B^* in (4.14) with B2bot_NeQ, B0_ABT, and B0_Bil which are designated by “PD_B2bot”, “PD_B2B0ABT” and “PD_B2B0Bil”, respectively.

4.3 Bottomside thickness of IRI model

The bottomside electron density profile of the IRI model is described by an analytical expression (Ramakrishnan and Rawer, 1972)

$$Ne_{bot_IRI}(h) = NmF2 \times \frac{\exp(-x^{B1})}{\cosh(x)} \quad (4.15)$$

and a variable x is defined as

$$x = \frac{hmF2 - h}{B0} \quad (4.16)$$

where $Ne_{bot_IRI}(h)$ is the bottomside electron density at height h , $NmF2$ is the F2 layer peak electron density (electron/m³), $hmF2$ is the F2 layer peak height of the peak electron density (km), $\cosh(x)$ is a hyperbolic cosine function of a variable x in (4.16), $B0$ and $B1$ are the thickness and the shape parameters of bottomside ionosphere, and h is the varying height. The $B0$ parameter in (4.16) is above zero (available) when the value of x in (4.16) is equal to 1. Here, $B0$ can be computed using either the difference between the $hmF2$ and the height where the electron density is equal to 0.24 times $NmF2$ ($h_{0.24}$) in an absence of the F1 layer or the difference between the $hmF2$ and the F1 peak height ($hmF1$) if the F1 layer exists. Meanwhile, $B0$ is equal to 0 where the height h in (4.16) is equal to the $hmF2$.

4.4 Comparison results of the B2bot_Pro

4.4.1 Comparisons between the B2bot_Pro and the B2bot_NeQ

Figures 4.1(a), (c) and (e) illustrate the diurnal variations of B2bot_Pro and B2bot_NeQ during three seasons from 2004 to 2006. The lines with circles show the B2bot_NeQ values from 2004 to 2006, designated by B2bot_NeQ04, B2bot_NeQ05, and B2bot_NeQ06, respectively. The lines without circles show the B2bot_Pro values from 2004 to 2006, designated by B2bot_Pro04, B2bot_Pro05, and B2bot_Pro06, respectively. For all seasons, both the B2bot_Pro and the B2bot_NeQ generally show similar diurnal variations, except pre-sunrise hours. The B2bot_Pro start increasing during 20-04 LT, reach the pre-sunrise peaks during 02-06 LT, and then decrease abruptly to minimum values at 07 LT. Afterwards, they increase again to reach the diurnal peaks during 11-13 LT, and then fall gradually to the period of 20-04 LT of a day. Meanwhile, the B2bot_NeQ begin increasing during pre-sunrise hours (03-06 LT), reach the diurnal peaks during 10-14 LT, and then decrease gradually until pre-sunrise hours. Tables 4.1 to 4.3 illustrate the transition points, local Times, and

This material is reserved for educational use only, not allowed for commercial use.

heights of diurnal variations of B2bot_Pro and B2bot_NeQ during three studied seasons from 2004 to 2006. The starting times of the B2bot_Pro are the same as those of the B2bot_NeQ during equinoxes. The diurnal peak times of B2bot_Pro and B2bot_NeQ are the same periods during 10-14 LT for all seasons. The pre-sunrise peaks followed by the collapses at 06-07 LT of the B2bot_NeQ can only be observed for all seasons of 2005. For all seasons from 2004 to 2006, the B2bot_NeQ values are often higher than the B2bot_Pro, except pre-sunrise hours.

Moreover, the percentage deviations between the B2bot_NeQ and the B2bot_Pro (namely, PD_B2bot) are also studied in this thesis. Here, a constant 30% of the percentage deviation is used for data clustering in this thesis, because it can divide clearly the percentage deviations into two groups, i.e., data group 1 and data group 2. The percentage deviations higher than 30 % are classified as a data group 1 whereas the ones lower than 30% are classified as a data group 2. In Figures 4.1(b), (d) and (f), we can observe that for all seasons of the studied years, the PD_B2bot are mainly distributed in data group 1 while the PD_B2bot are partially distributed in data group 2. At the diurnal peaks of the B2bot_Pro, the absolute differences between the B2bot_NeQ and the B2bot_Pro ($|B2bot_NeQ - B2bot_Pro|$) range from 24-73 km, from 22-64 km, from 40-82 km during the equinoxes, summers, and winters, respectively, for all studied years. The averages, the minima, and the maxima in PD_B2bot during daytime and nighttime are illustrated in Table 4.4 to 4.6, respectively.

Table 4.1 Transition points, local times, and heights of diurnal variations of the B2bot_Pro and B2bot_NeQ during the equinoxes from 2004 to 2006.

Parameters	B2bot_Pro				B2bot_NeQ	
	Start Points	First Peaks	Minimum Points	Second Peaks	Start Points	Diurnal Peaks
Local Times	00-04 LT	06 LT	07 LT	12-13 LT	03-06 LT	10 LT
Heights (km)	19-43	81-133	39-49	125-198	86-103	203-233

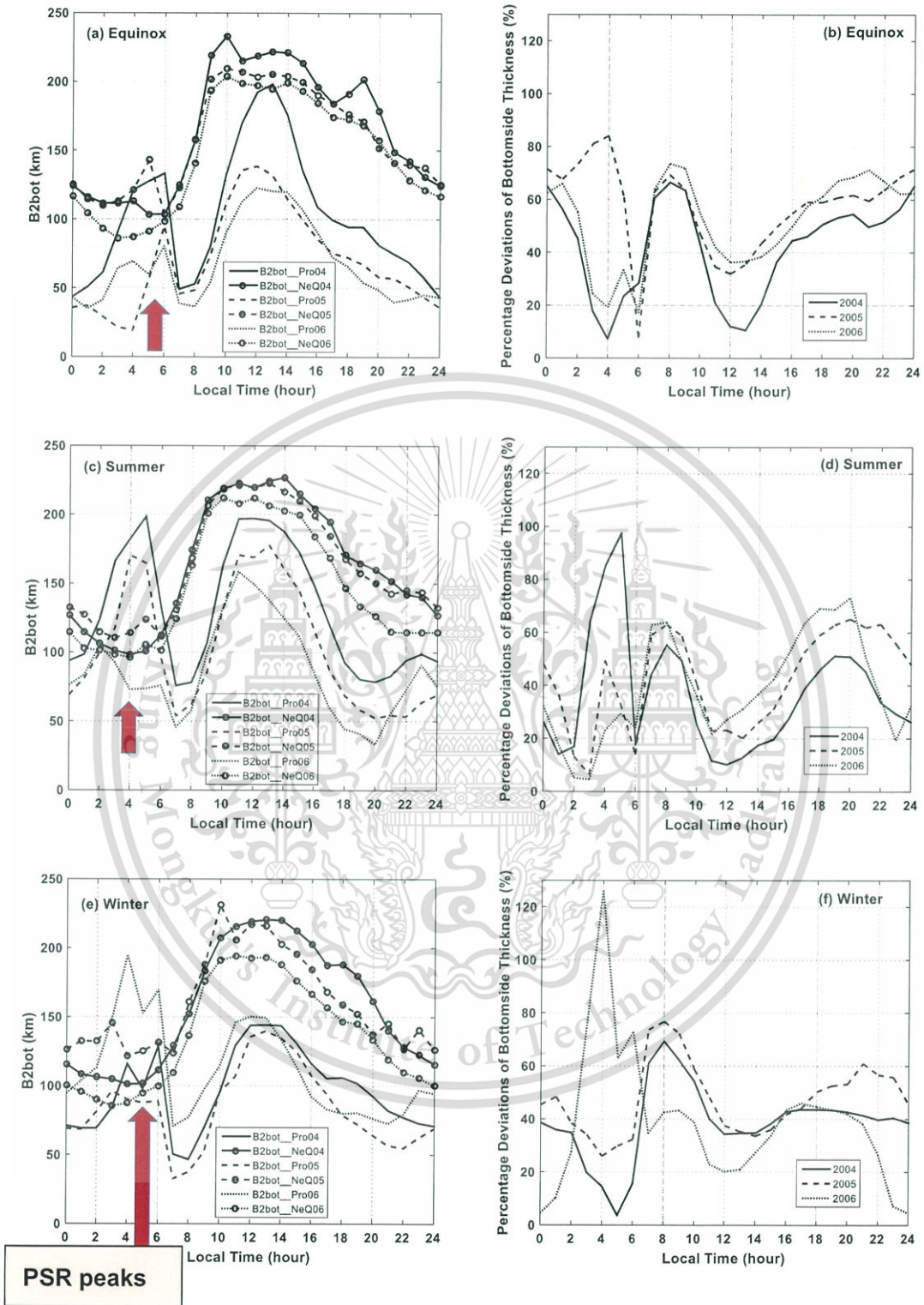


Figure 4.1 Diurnal variations of the B2bot_{Pro} and the B2bot_{NeQ} as well as the percentage deviations (in %) between three seasons from 2004 to 2006.

This material is reserved for educational use only, not allowed for commercial use.

Forbidden to modify the content, and cite the document when use.

Table 4.2 Transition points, local times, and heights of diurnal variations of the B2bot_Pro and B2bot_NeQ during the summers from 2004 to 2006.

Parameters	B2bot_Pro				B2bot_NeQ	
	Start Points	First Peaks	Minimum Points	Second Peaks	Start Points	Diurnal Peaks
Local Times	20 LT	02-05 LT	07 LT	11-13 LT	03-04 LT	10-14 LT
Heights (km)	33-78	106-198	46-75	163-197	96-110	211-227

Table 4.3 Transition points, local times, and heights of diurnal variations of the B2bot_Pro and B2bot_NeQ during the winters from 2004 to 2006.

Parameters	B2bot_Pro				B2bot_NeQ	
	Start Points	First Peaks	Minimum Points	Second Peaks	Start Points	Diurnal Peaks
Local Times	21-23 LT	03-04 LT	07 LT	12-13 LT	03-04 LT	11-13 LT
Heights (km)	54-73	96-197	32-71	139-153	85-121	194-220

Table 4.4 Averaged PD_B2bot during daytime and nighttime from 2004 to 2006.

Seasons	Equinoxes		Summers		Winters	
	Daytime	Nighttime	Daytime	Nighttime	Daytime	Nighttime
Data Group 1 (DG 1)	Majority > 30%	Majority > 30%	Majority > 30%	Majority > 30%	Majority > 30%	Majority > 30%
Averaged DG 1	52%	62%	50%	56%	47%	50%
Data Group 2 (DG 2)	Minority < 30%	Minority < 30%	Minority < 30%	Minority < 30%	Minority < 30%	Minority < 30%
Averaged DG 2	16%	18%	20%	17%	23%	17%

Table 4.5 Minima and maxima in PD_B2bot during daytime from 2004-2006.

Seasons	Equinoxes			Summers			Winters		
	2004	2005	2006	2004	2005	2006	2004	2005	2006
Minimum Times	13 LT	12 LT	12 LT	12 LT	13 LT	11 LT	12 LT	14 LT	12 LT
Minimum Values	11%	32%	36%	10%	20%	21%	34%	34%	20%
Maximum Times	08 LT	08 LT	08 LT	08 LT	08 LT	18 LT	08 LT	08 LT	17 LT
Maximum Values	66%	69%	74%	55%	63%	69%	69%	77%	46%

This material is reserved for educational use only, not allowed for commercial use.

Forbidden to modify the content, and cite the document when use.

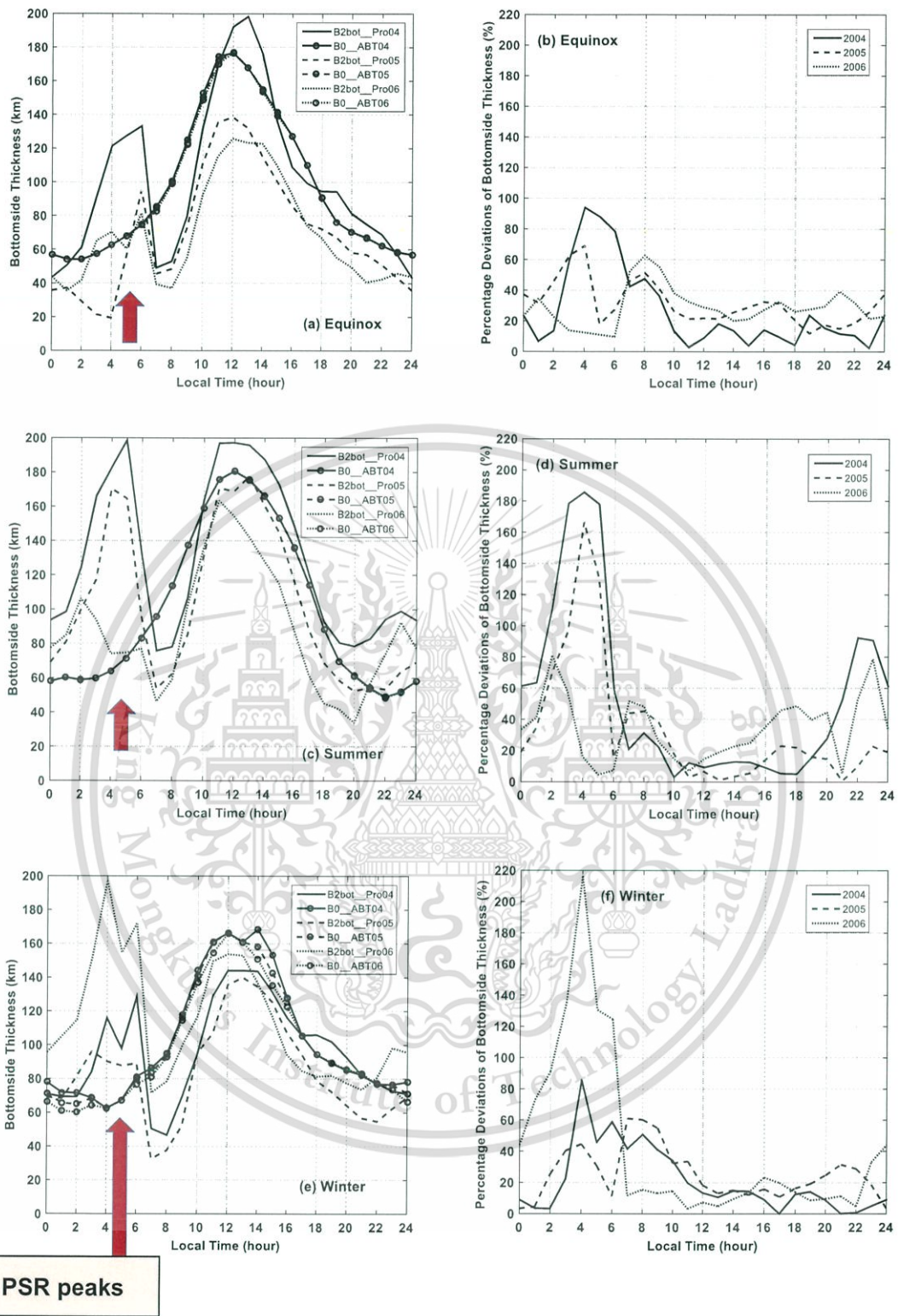


Figure 4.2 Diurnal variations of the B2bot_Pro and the B0_ABT as well as the percentage deviations (in %) during three seasons from 2004 to 2006.

Table 4.6 Minima and maxima in PD_B2bot during nighttime from 2004-2006.

Seasons	Equinoxes			Summers			Winters		
Years	2004	2005	2006	2004	2005	2006	2004	2005	2006
Minimum Times	04 LT	06 LT	06 LT	01 LT	03 LT	03 LT	05 LT	04 LT	00 LT
Minimum Values	7%	8%	17%	14%	6%	4%	4%	26%	4%
Maximum Times	00 LT	04 LT	21 LT	05 LT	20 LT	20 LT	19 LT	21 LT	04 LT
Maximum Values	65%	84%	71%	97%	65%	73%	43%	61%	126%

4.4.2 Comparisons between the B2bot_Pro and the B0_ABT

In this subsection, the comparisons between the B2bot_Pro and the B0 predicted with ABT-2009 option of the IRI-2012 model (B0_ABT) are depicted in conjunction with the percentage deviations. Figures 4.2(a), (c) and (e) demonstrate the diurnal variations in B2bot_Pro and B0_ABT during three studied seasons. The lines with circles show the B0_ABT values from 2004 to 2006, respectively (namely, B0_ABT04, B0_ABT05, and B0_ABT06). Besides, the lines without circles show the B2bot_Pro values from 2004 to 2006, respectively (namely, B2bot_Pro04, B2bot_Pro05, and B2bot_Pro06). Note that the B2bot_Pro04, B2bot_Pro05, and B2bot_Pro06 results in Figure 4.2 are the same as those in Figure 4.1, they are illustrated again in order to compare and analyze easily with the B0_ABT values.

In Figures 4.2(a), (c) and (e), both the B2bot_Pro and the B0_ABT generally illustrate similar diurnal variations, except pre-sunrise hours, for all seasons. The B0_ABT begin increasing during 22-04 LT, reach the diurnal peaks during 12-14 LT, and then decrease gradually to the period of 22-04 LT. Table 4.7 shows the transition points, local Times, and heights of diurnal variations of the B2_ABT during three studied seasons from 2004 to 2006. The starting times of the B2bot_Pro are only the same as those of the B0_ABT during pre-sunrise hours in the equinoxes and during sunset hours in the summers. The occurrence times of second peak in B2bot_Pro are the same as those of diurnal peak in B0_ABT, i.e., during 10-14 LT for all seasons. When the solar activities are lower such as 2005 and 2006 in this thesis, the B0_ABT have a tendency to be higher than the B2bot_Pro with a longer duration. For example, in 2005 and 2006, the B0_ABT are higher than the B2bot_Pro with durations of about 20 hours, 13 hours, and 14 hours during the equinoxes, summers, and

This material is reserved for educational use only, not allowed for commercial use.

winters, respectively. Meanwhile, in 2004, the B0_AB T are higher than the B2bot_Pro with shorter durations of about 14 hours, 2 hours, and 9 hours during the same seasons, respectively. Furthermore, the pre-sunrise peaks in B0_AB T disappear unlike the B2bot_Pro for all seasons of the studied years, except the winters in 2005 and 2006 (lower solar activities). The sunrise collapses also disappear for all seasons of the studied years. At the diurnal peaks of the B2bot_Pro, the absolute differences between the B0_AB T and the B2bot_Pro ($|B0_AB T - B2bot_Pro|$) range from 15-51 km, from 2-34 km, from 8-30 km during the equinoxes, summers, and winters, respectively, for all studied years.

Moreover, the percentage deviation of 30% is also used to divide the PD_B2B0AB T values into data group 1 and data group 2. The percentage deviations higher than 30% are classified as a data group 1 while the ones lower than 30% are classified as a data group 2. In Figures 4.2(b), (d) and (f), for all seasons, the PD_B2B0AB T are partially distributed in data group 1, while the PD_B2B0AB T are mainly distributed in data group 2. The PD_B2B0AB T are higher than 30% significantly during pre-sunrise hours for all seasons and during nighttime in the summers. Besides, the averages, the minima, and the maxima in PD_B2B0AB T during daytime and nighttime from 2004 to 2006 are also shown in Tables 4.8 to 4.10, respectively.

Table 4.7 Transition points, local times and heights of diurnal variations of the B0_AB T from 2004 to 2006.

Parameters	B2bot_Pro				B2bot_NeQ	
	Start Points	First Peaks	Minimum Points	Second Peaks	Start Points	Diurnal Peaks
Local Times	02 LT	12 LT	22 LT	12 LT	02-04 LT	12-14 LT
Heights (km)	54	177	49	181	67-69	157-179

Table 4.8 Averaged PD_B2B0ABT during daytime and nighttime from 2004 to 2006.

Seasons	Equinoxes		Summers		Winters	
Periods	Daytime	Nighttime	Daytime	Nighttime	Daytime	Nighttime
Data Group 1 (DG 1)	Minority > 30%	Minority > 30%	Minority > 30%	Minority > 30%	Minority > 30%	Minority > 30%
Averaged DG 1	43%	56%	43%	87%	46%	79%
Data Group 2 (DG 2)	Majority < 30%	Majority < 30%	Majority < 30%	Majority < 30%	Majority < 30%	Majority < 30%
Averaged DG 2	18%	17%	13%	13%	18%	11%

Table 4.9 Minima and maxima in PD_B2B0ABT during daytime from 2004-2006.

Seasons	Equinoxes			Summers			Winters		
Years	2004	2005	2006	2004	2005	2006	2004	2005	2006
Minimum Times	11 LT	11 LT	14 LT	10 LT	13 LT	11 LT	17 LT	17 LT	13 LT
Minimum Values	3%	21%	20%	3%	1%	7%	0%	11%	5%
Maximum Times	08 LT	08 LT	08 LT	08 LT	07 LT	18 LT	08 LT	07 LT	16 LT
Maximum Values	47%	51%	63%	31%	45%	52%	51%	61%	23%

Table 4.10 Minima and maxima in PD_B2B0ABT during nighttime from 2004-2006.

Seasons	Equinoxes			Summers			Winters		
Years	2004	2005	2006	2004	2005	2006	2004	2005	2006
Minimum Times	23 LT	19 LT	06 LT	19 LT	21 LT	05 LT	21 LT	00 LT	22 LT
Minimum Values	2%	12%	10%	16%	1%	5%	0%	3%	5%
Maximum Times	04 LT	04 LT	21 LT	04 LT	04 LT	02 LT	04 LT	04 LT	04 LT
Maximum Values	94%	69%	39%	186%	167%	81%	86%	45%	216%

4.4.3 Comparisons between the B2bot_Pro and the B0_Bil

Figures 4.3(a), (c), and (e) show the diurnal variations in B2bot_Pro and the B0 of Bil-2000 option during three seasons from 2004 to 2006. The lines with circles denote the B0 of Bil-2000 option (B0_Bil) from 2004 to 2006, designated by B0_Bil04, B0_Bil05, and B0_Bil06, respectively.

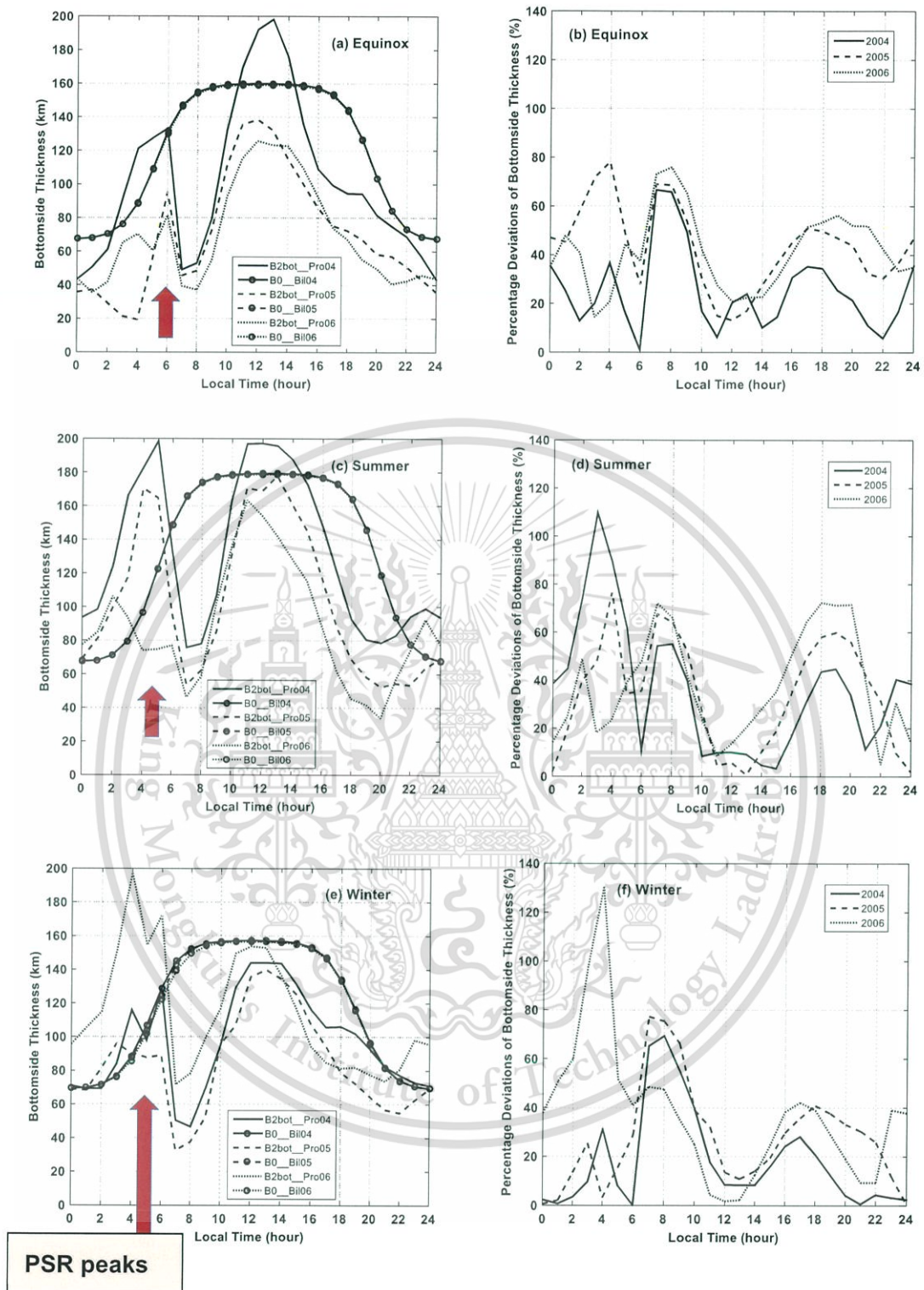


Figure 4.3 Diurnal variations of the B2bot_Pro and the B0_Bil as well as the percentage deviations (in %) during three seasons from 2004 to 2006.

Besides, the lines without circles denote the B2bot_Pro values from 2004 to 2006, designated by B2bot_Pro04, B2bot_Pro05, and B2bot_Pro06, respectively. Note

that the B2bot_Pro04, B2bot_Pro05, and B2bot_Pro06 results in Figure 4.3 are the same as those in Figure 4.1, they are demonstrated again in order to compare and analyze easily with the B0_Bil values. In Figures 4.3(a), (c) and (e), we find that the B0_Bil values start increasing about 67-69 km at the midnight, achieve to the diurnal peaks of about 157-179 km at the local noontime, and then decrease gradually toward the midnight for all seasons. The diurnal variations in B0_Bil differ from those in B2bot_Pro. Moreover, both the pre-sunrise peaks and the sunrise collapses in B0_Bil disappear unlike the B2bot_Pro, because the diurnal variation in B0_Bil is based on a day-night transition function between daytime and nighttime values (Bilitza, 1990; Bilitza et al., 2000).

The starting times of the B0_Bil differ from those of the B2bot_Pro for all seasons of the studied years. The occurrence times of second peak in B2bot_Pro are the same as those of diurnal peak in B0_Bil, i.e., during 11-13 LT for all seasons. When the solar activities are lower such as 2005 and 2006 in this thesis, the B0_Bil have a tendency to be higher than the B2bot_Pro with a longer duration in the equinox and summer seasons. For instance, the B0_Bil are higher than the B2bot_Pro in 2005 and 2006 with durations of about 24 hours and 15 hours during the equinoxes and summers, respectively. Besides the B0_Bil are higher than the B2bot_Pro in 2004 with shorter durations of about 19 hours and 13 hours during the same seasons, respectively. Note that the B0_Bil are higher than the B2bot_Pro with the same durations of about 14 hours during the winters for all the studied years. At the diurnal peaks of the B2bot_Pro during 11-13 LT, the absolute differences between the B0_Bil and the B2bot_Pro ($|B0_Bil - B2bot_Pro|$) range from 21-38 km, from 1-37 km, from 3-21 km during the equinoxes, summers, and winters, respectively.

Furthermore, for considering the PD_B2B0Bil values, the percentage deviation of 30% is also used to divide the PD_B2B0Bil values into data group 1 and data group 2. The percentage deviations higher than 30% are classified as a data group 1, while the ones lower than 30% are classified as a data group 2. In Figures 4.3(b), (d) and (f), we can observe that for all seasons, the PD_B2B0Bil are mostly distributed in data group 1 whereas the PD_B2B0Bil are partially distributed in data group 2. Note that

This material is reserved for educational use only, not allowed for commercial use.

the PD_B2B0Bil are higher than 30% significantly during pre-sunrise hours in the summer and winter seasons. Besides, the averages, the minima, and the maxima in PD_B2B0Bil during daytime and nighttime from 2004 to 2006 are also demonstrated in Tables 4.11 to 4.13.

Table 4.11 Averaged PD_B2B0Bil during daytime and nighttime from 2004-2006.

Seasons	Equinoxes		Summers		Winters	
	Daytime	Nighttime	Daytime	Nighttime	Daytime	Nighttime
Data Group 1 (DG 1)	Majority > 30%	Majority > 30%	Majority > 30%	Majority > 30%	Majority > 30%	Minority > 30%
Averaged DG 1	52%	44%	53%	52%	50%	53%
Data Group 2 (DG 2)	Minority < 30%	Minority < 30%	Minority < 30%	Minority < 30%	Minority < 30%	Majority < 30%
Averaged DG 2	19%	17%	12%	15%	15%	10%

Table 4.12 Minima and maxima in PD_B2B0Bil during daytime from 2004-2006.

Seasons	Equinoxes			Summers			Winters		
	2004	2005	2006	2004	2005	2006	2004	2005	2006
Minimum Times	11 LT	12 LT	12 LT	15 LT	13 LT	11 LT	14 LT	13 LT	12 LT
Minimum Values	6%	13%	21%	3%	1%	8%	8%	11%	2%
Maximum Times	07 LT	07 LT	08 LT	08 LT	07 LT	18 LT	08 LT	07 LT	07 LT
Maximum Values	67%	69%	76%	55%	68%	72%	69%	77%	49%

Table 4.13 Minima and maxima in PD_B2B0Bil during nighttime from 2004-2006.

Seasons	Equinoxes			Summers			Winters		
	2004	2005	2006	2004	2005	2006	2004	2005	2006
Minimum Times	06 LT	06 LT	03 LT	21 LT	00 LT	22 LT	06 LT	00 LT	22 LT
Minimum Values	1%	28%	14%	11%	2%	5%	0%	1%	9%
Maximum Times	00 LT	04 LT	19 LT	03 LT	04 LT	20 LT	04 LT	19 LT	04 LT
Maximum Values	36%	78%	56%	110%	77%	71%	31%	38%	130%

4.4.4 Comparisons between the B2bot_Pro and the B0_obs

A new expression for computing the B2bot of the NeQuick 2 model (namely, B2bot_Pro) is proposed in this thesis, therefore, it should be compared to the B0_ABT (the latest B0 prediction model of the IRI model) and the observed B0 from digisondes (namely, B0_obs) simultaneously so as to show how they have either similar or different trends one another. Comparing the diurnal variations among the B2bot_Pro, the B0_ABT and the B0_obs is conducted in this subsection and described as follows.

In the past, Altadill et al. (2009) studied and analyzed the electron density profiles as well as any ionospheric parameters from 27 ionosonde stations around the world. Afterwards, they proposed a new prediction model for the IRI B0 using spherical harmonic analysis (SHA). To compare between the B2bot_Pro and the B0_obs, only two out of 27 ionosonde stations located on the similar latitudes of Chumphon station for the northern and southern hemispheres, are selected to study and analyze in this thesis, i.e., Kwajalein (9.0°N, 167.2°E, GMT +12 hours) and Jicamarca (12.0°S, 76.8°W, GMT-5 hours). The studied date is on March 20th, 2006 (March equinox). Moreover, the percentage deviations between B2bot_Pro and B0_ABT or B0_obs are defined as

$$PD_{B^{**}} (\%) = \frac{|B^{**} - B2bot_Pro_obs| \times 100}{B^{**}} \quad (4.17)$$

where B^{**} denote the B0_ABT or the B0_obs, and the B2bot_Pro_obs represent the B2bot_Pro which are obtained by replacing the observed ionospheric parameters at these two stations into the proposed equation of B2bot_Pro in (4.13).

Figures 4.4 and 4.5 illustrate the diurnal variations of the B2bot_Pro_obs, the B0_ABT, and the B0_obs at Kwajalein and Jicamarca stations on March 20th, 2006, respectively. The dotted lines without circles denote the B0_ABT and the dotted lines with circles denote the B0_obs. Meanwhile, the solid lines with circles represent the B2bot_Pro_obs. From these figures, we can see that the diurnal variations of the B0_obs have the same trends as those of the B2bot_Pro_obs at these two stations,

This material is reserved for educational use only, not allowed for commercial use.

but the B0_obs are always higher than the B2bot_Pro_obs. The diurnal variations of the B2bot_Pro_obs generally have the same trends as those of the B0_AB T, except pre-sunrise hours. For Kwajalein station, the percentage deviations between B0_obs and B2bot_Pro_obs range from 7.80%-45.92%, while the ones between B0_obs and B0_AB T range from 1.35%-54.72%. The averaged percentage deviations between B0_obs and B2bot_Pro_obs (29.89%) are higher about 5.46% than those between B0_obs and B0_AB T (24.43%). The pre-sunrise peaks of both B2bot_Pro_obs and B0_obs can be observed clearly in which they are about 71 km and 51 km, respectively, while the pre-sunrise peak of B0_AB T cannot be seen well. For Jicamarca station, the percentage deviations between B0_obs and B2bot_Pro_obs range from 2.84%-32.50%, whereas the ones between B0_obs and B0_AB T range from 1.36%-46.60%. The averaged percentage deviations between B0_obs and B2bot_Pro_obs (21.70%) are higher about 7.77% than those between B0_obs and B0_AB T (13.93%). The pre-sunrise peaks of B0_obs and B2bot_Pro_obs can also be observed in which they are about 162 km and 190 km, respectively, while the pre-sunrise peak of B0_AB T disappears.

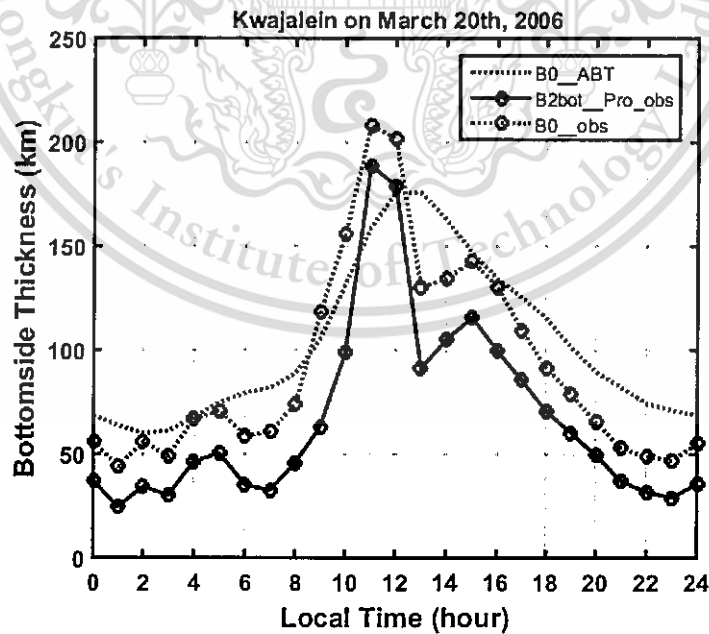


Figure 4.4 Diurnal variations of the B0_AB T, the B2bot_Pro_obs and the B0_obs at Kwajalein station on March 20th 2006.

This material is reserved for educational use only, not allowed for commercial use.

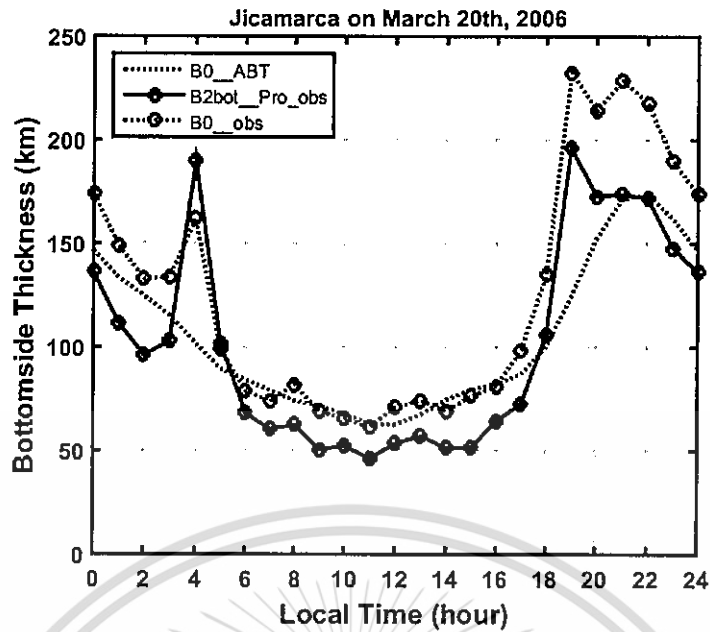


Figure 4.5 Diurnal variations of the B0_AB T, the B2bot_Pro_obs and the B0_obs at Jicamarca station on March 20th, 2006.

Moreover, we can see the great discrepancies between the B2bot_Pro and the B0_AB T during pre-sunrise hours in Figures 4.4 and 4.5 in which can be described as follows. Firstly, Altadill et al. (2009) use the time series of hourly electron density profiles from 27 ionosonde stations to obtain the monthly average electron density profiles and to extract the expected B0 and B1 parameters of the IRI model under quiet conditions. But we find that only three ionosonde stations located on the similar latitudes of Chumphon station, i.e., Kwajalein (9.0°N , 167.2°E), Ascension Is. (7.95°S , 14.4°W), and Jicamarca (12.0°S , 76.8°W), were selected to model the B0 and B1 parameters by their spherical harmonic analysis (SHA), hence, the pre-sunrise peaks at 0° - 20° dip latitudes seem to be small. Secondly, the B0_obs peaks can often be observed during pre-sunrise hours for all months in 2005 at Jicamarca station as shown in Altadill et al. (2009). On the other hand, their modeled B0 with SHA (B0_AB T) are often higher than the pre-sunrise peaks and do not reflect well for these peaks. Thirdly, the monthly averaged representative profile method (Huang and Reinisch, 1996) is applied in Altadill et al. (2009) in order to exclude 25% of the

This material is reserved for educational use only, not allowed for commercial use.

Forbidden to modify the content, and cite the document when use.

bottomside electron density profiles that have the largest deviations. Then, the averaged quiet ionospheric parameters are modeled and the experimental $B0_ABT$ are obtained from the best fit of (4.15) to the averaged bottomside electron density profiles (Reinisch and Huang, 1998). Meanwhile, the proposed $B2bot_Pro$ are computed using the monthly median values for all measured ionospheric parameters without any exclusion techniques. Hence, the great discrepancies between the $B2bot_Pro$ and the $B0_ABT$ during pre-sunrise hours can possibly be found. In Figures 4.4 and 4.5, the pre-sunrise peaks of both $B0_obs$ and $B2bot_Pro_obs$ at both Kwajalein and Jicamarca stations can be observed obviously while the pre-sunrise peak of $B0_ABT$ cannot be seen clearly. Moreover, Sethi and Mahajan (2002) find that the median $B0$ observed at Arecibo ($18.4^{\circ}N$, $66.7^{\circ}W$) with an incoherent scatter radar (ISR) during a solar maximum period (1989-1990) show another peaks during 02-05 LT, other than the diurnal peaks around local noontime. These pre-sunrise peaks at Arecibo range from 105-127 km.

4.5 Physical Explanations and Discussions

The studied results in this thesis illustrate that the proposed $B2bot_Pro$ at Chumphon station generally decrease following to the decreasing solar activity for all seasons from 2004 to 2006. The maximum $B2bot_Pro$ occur during daytime while the minimum ones occur during nighttime. In this subsection, the observed $B0$ during daytime, nighttime, and pre-sunrise hours at other stations are also addressed in conjunction with the studied bottomside thickness parameters in this thesis. The details are explained as follows.

During daytime, the diurnal variations of the bottomside thickness parameter at different stations are summarized as follows. The proposed $B2bot_Pro$ are about 33-198 km from 2004 to 2006 at equatorial latitude station, Chumphon. Compared to previous works at other equatorial latitude stations, the observed $B0$ are about 73-282 km during high solar activity at Ouagadougou, Burkina Faso (Adeniyi and Radicella, 1998) and about 80-280 km during solar minimum at Jicamarca, Peru (Lee et al., 2008). For other low latitude stations, the observed $B0$ during high solar

This material is reserved for educational use only, not allowed for commercial use.

Forbidden to modify the content, and cite the document when use.

activity are about 55-150 km at Wuhan, China (Chuo et al., 2010) and about 70-230 km at Chung-Li, Taiwan (Chuo, 2012). During 2004-2006, the B2bot_NeQ are about 109-233 km, whereas the B0_ABT and the B0_Bil are about 81-181 km and 133-179 km, respectively. These above details identify that the lower bounds of the proposed B2bot_Pro are the lowest among all B0_obs values at other stations, the B2bot_NeQ, the B0_ABT and the B0_Bil. In contrast, the upper bound of B2bot_Pro is approximately a medium value among the upper bounds of the B0_obs at other stations, the B2bot_NeQ, the B0_ABT, and the B0_Bil.

During nighttime, the diurnal variations of the bottomside thickness parameter at different stations are concluded as follows. The proposed B2bot_Pro are about 19-198 km from 2004 to 2006 at Chumphon station. For other equatorial latitude stations, the observed B0 are about 56-149 km during high solar activity at Ouagadougou, Burkina Faso (Adeniyi and Radicella, 1998) and about 55-150 km during solar minimum at Jicamarca, Peru (Lee et al., 2008). For other low latitude stations, the observed B0 during high solar activity are about 60-100 km at Wuhan, China (Chuo et al., 2010) and about 75-120 km at Chung-Li, Taiwan (Chuo, 2012). From 2004 to 2006, the B2bot_NeQ are about 85-202 km, whereas the B0_ABT and the B0_Bil are about 49-90 km and about 67-149 km, respectively. These mentioned details can be inferred that the lower bounds of the proposed B2bot_Pro are the lowest among those of the B0_obs at other stations, the B2bot_NeQ, the B0_ABT and the B0_Bil. On the other hand, the upper bounds of both B2bot_Pro and B2bot_NeQ are comparable and they are the highest among the upper bounds of the B0_obs at other stations, the B0_ABT and the B0_Bil.

For the studied results, we find that the B2bot_Pro show the highest peaks around local noontime during the summers and the lowest around midnight during the equinoxes. These results are in good agreement with the B0_obs from March 2002 to February 2005 at Hainan station, China (Zhang et al., 2008). The gradual increases in B2bot_Pro during 08-13 LT are caused by the vertical $\mathbf{E} \times \mathbf{B}$ plasma drift in which it moves the plasma up to the higher altitudes on the equatorial ionosphere. Afterwards, the plasma does not only diffuse along the magnetic lines

toward low latitudes, but also enhance the electron density in low latitudes (Fejer et al., 1995). Fejer et al. (1995) revealed that the vertical plasma drift play an important role in the Equatorial Ionization Anomaly (EIA) region in which the gradual increases of B2bot_Pro occur during sunrise hours in the equinoxes and summers, but they last until 13 LT during the winters. Likewise, Liu et al. (1999) also studied the horizontal eastward electric fields of the atmospheric dynamo in the E layer near the equator and disclosed that these eastward electric fields lift the vertical $\mathbf{E} \times \mathbf{B}$ plasma drift up to higher altitudes, then diffuse downward. These phenomena produce the enhanced electron density during daytime in the EIA region.

Furthermore, we find that the diurnal variations of the B2bot_Pro have the pre-sunrise peaks in which the peaks in the summers are larger than those in the other two seasons, and the pre-sunrise peaks of the B2bot_Pro are mostly larger than those of the B2bot_NeQ and the B0_ABT. The highest pre-sunrise peaks of the B2bot_Pro, the B2bot_NeQ, and the B0_ABT are about 198 km, 146 km, and 69 km, respectively. In addition, the pre-sunrise peaks in B0 can also be seen at Ouagadougou, Burkina Faso (Adeniyi and Radicella, 1998), Jicamarca, Peru (Lee et al., 2008), Wuhan, China (Chuo et al., 2010) Chung-Li, and Taiwan (Chuo, 2012), in which their largest pre-sunrise peaks are about 150 km, 120 km, 106 km, 100 km, respectively. The pre-sunrise peaks of B2bot_Pro at Chumphon station located near the equatorial latitude are the largest in comparison with those of the observed B0 at the other four stations, the B2bot_NeQ, and the B0_ABT. The pre-sunrise peaks of B2bot_Pro are associated with the uplift of the F layer during 03-05 LT. This phenomenon corresponds to the results of Murthy et al. (1990) in which they studied the thermospheric meridional winds over two equatorial latitude stations during nighttime and revealed that the neutral winds turn toward southward at 03 LT and then turn back at 05 LT. These southward neutral winds cause an upward plasma drift in which it does not only elevate the F layer to higher altitudes, but also increase the B0 at the same time during pre-sunrise hours. Likewise, Rishbeth et al. (1987) observed that the thermospheric winds, traveling toward the equator and being driven by auroral heating, also lead to the variations of atmospheric

composition until both the $NmF2$ and the TEC are lower. Furthermore, no plasma replenishments occur in the ionosphere at equatorial latitudes, because the ionosphere in equatorial latitude does not link to the plasmaphere by the magnetic field lines and the chemical recombination occurs continuously at low latitudes during nighttime. Hence, both the $NmF2$ and the TEC at Chumphon station are the lowest during pre-sunrise hours, but the decreases in TEC are slower than those in $NmF2$. These events cause higher slab thickness and B2bot_Pro peaks during pre-sunrise hours. On the other hand, the plasma replenishments occur at the middle latitudes during nighttime, because the ionosphere plasma is furnished from the plasmaphere plasma along magnetic field lines at middle latitudes.

Furthermore, the B2bot_Pro collapses at 07 LT can be observed for all seasons in which they are in good agreement with the observed B0 during solar maximum at Chung-Li, Taiwan (Chuo, 2012). These sunrise collapses during the winters are stronger than those during the summers and equinoxes, respectively. The sunrise collapses in B0_obs can also be found from ground-based measurements at Jicamarca station (Lee et al., 2008), Hainan station (Zhang et al., 2008), and Wuhan station (Chuo et al., 2010) as well as from incoherent scatter radar (ISR) measurements at Millstone Hill station (Lei et al., 2004).

CHAPTER 5

BOTTOMSIDE THICKNESS FOR TOPSIDE IONOSPHERE

Ionospheric modeling is a crucial task of monitoring global space weather and mitigating the undesired influences. Topside ionosphere modeling is a challenging work, while bottomside ionosphere modeling can be made with good accuracy from ionograms recorded by ground-based digisondes or ionosondes. These measurements cannot provide information on the topside ionosphere, hence, some additional instruments are needed to support and model the empirical topside ionosphere. There are several methods to collect such topside information, mostly via incoherent scatter radar and topside sounder. A number of recent publications show endeavors to develop various ionospheric topside models. Different analytical functions (e.g. parabola, exponential, Chapman, or Epstein functions) have been used to model topside electron density profiles (EDPs) at different locations (e.g. Stankov et al., 2003; Reinisch et al., 2004a). At Chumphon station, FMCW ionosonde and dual-frequency GPS system are installed, both the topside EDP are not readily available from these devices. Hence, the computations of topside EDPs using analytical functions based on either the NeQuick 2 model or the IRI model are the interesting issues for FMCW ionosonde. In the past, many studies for the topside modeling have used the data source from in situ measurements (Trisková et al., 2006) or used Chapman function to merge an ionosonde-based model with a plasmaphere model (Reinisch, 2004). However, the topside EDP at Chumphon station has not been examined nor analyzed, hence, another aim of this thesis is to investigate the topside EDP at Chumphon station.

5.1 NeQuick topside formulation

The NeQuick model has been included in the IRI-2012 model under the option “NeQuick” in field “Ne topside” for providing the topside electron density.

The mathematical formulation is an Epstein layer function which describes the topside electron density at height h , $N(h)$, with a height-varying scale height $H(h)$, i.e.,

$$N(h) = \frac{4NmF2}{(1 + \exp(z))^2} \exp(z) \quad (5.1)$$

where

$$z = \frac{h - hmF2}{H(h)} \quad (5.2)$$

and

$$H(h) = H0 \left[1 + \frac{rg(h - hmF2)}{rH0 + g(h - hmF2)} \right] \quad (5.3)$$

where $NmF2$ and $hmF2$ are peak electron density (electron/m³) and peak height of $NmF2$ (km) in F2 layer, respectively, and $r = 100$ and $g = 0.25$ are constant. Here, the $NmF2$ and the $hmF2$ are computed using (2.1) and (2.3), respectively.

Moreover, the $H0$ parameter is the NeQuick topside thickness parameter which can be computed from (Coïsson et al., 2006)

$$H0 = k \cdot B2bot \quad (5.4)$$

where the constant k is called a NeQuick topside shape parameter which can be calculated by

$$k = 3.22 - 0.0538foF2 - 0.00664hmF2 + 0.113 \frac{hmF2}{B2bot} + 0.00257Rz12. \quad (5.5)$$

Here, the $Rz12$ is a 12-month running average relative sunspot number which can be obtained from the IRI-2012 model. The empirical equation of k in (5.5) is the latest updated expression which is based on ISIS 2 TOPIST topside electron density profiles (Coïsson et al., 2006) and it has been included in the NeQuick 2 model (Nava et al., 2008). In addition, the $B2bot$ parameter in this Chapter is computed using both the $NmF2$ and the maximum of electron density derivative with respect to height. This material is reserved for educational use only, not allowed for commercial use.

$(dN/dh)_{\max}$ as described earlier in Section 4.1. In this thesis, the B2bot values for depicting the topside EDPs are computed with the original B2bot expressions of the NeQuick 2 model as shown in (4.2), since the proposed B2bot (B2bot_Pro) in Section 4.2 has not yet verified by other researchers.

In this thesis, the topside electron densities at Chumphon are computed using (4.1). Afterwards, the NeQuick-derived topside EDPs are depicted and the corresponding topside TEC values are computed using the integration of NeQuick-derived topside EDPs from the $hmF2$ to 1,400 km. Furthermore, the topside EDPs of three options of the IRI-2012 model, i.e., NeQuick, IRI01-corr, and IRI2001, are also shown and named as “IRINeQ,” “IRI01cor,” and “IRI2001,” respectively.

In addition to the topside EDPs, the TEC values of topside ionosphere over Chumphon are also studied in this thesis. The amounts of topside TEC values are still equal to 4 which is similar to the amounts of topside EDPs. Here, the NeQuick-derived topside TEC values are named as “tT_CPN,” while other topside TEC values with NeQuick, IRI01-corr, and IRI2001 options are named as “tT_IRINeQ,” “tT_IRI01cor,” and “tT_IRI2001,” respectively.

Furthermore, three differences among the studied parameters are also considered in this thesis. Firstly, the IAD_IRI (unit: TECU) is defined as the integration of absolute difference between two different topside electron density values from the $hmF2$ to 1,400 km with an incremental step $\Delta h = 10$ km, i.e.,

$$IAD_IRI = \sum_{h=hmF2}^{1400} |Ne_IRI_h - Ne_CPN_h| \quad (5.6)$$

where Ne_IRI_h are representatives of Ne_IRINeQ , $Ne_IRI01cor$, or $Ne_IRI2001$, and Ne_CPN_h are NeQuick-derived topside electron density values. The IAD_IRI values are thus named as “IAD_IRINeQ,” “IAD_IRI01cor,” and “IAD_IRI2001.” Since the $hmF2$ values between the IRI-2012 model and the observation are different, the minimum $hmF2$ are thus selected to calculate all of the IAD_IRI values. Although it can be seen that the IAD_IRI errors occur inevitably because of different $hmF2$ values, the IAD_IRI values are only the preliminary results for comparing among the studied topside

This material is reserved for educational use only, not allowed for commercial use.

EDPs in this thesis. The comparison results of topside EDPs, the topside TEC values, and the IAD_IRI are shown and analyzed in Section 5.3.

Secondly, the AD_NeQ is defined as the absolute difference between tT_{CPN} and tT_{IRINeQ} . The AD_NeQ (Unit: TECU) is expressed as

$$AD_NeQ = |tT_{CPN} - tT_{IRINeQ}| \quad (5.7)$$

Finally, the D_{tT} is defined as the difference between IGS_TEC (TEC from the International GNSS service) and any topside TEC values. The D_{tT} (Unit: TECU) is computed by

$$D_{tT} = IGS_TEC - tT \quad (5.8)$$

where “ tT ” represent tT_{CPN} , $tT_{IRI01cor}$, and $tT_{IRI2001}$, and the corresponding D_{tT} values are named as “ D_{CPN} ,” “ $D_{IRI01cor}$,” and “ $D_{IRI2001}$,” respectively. The comparison results of AD_NeQ and D_{tT} parameters are investigated and analyzed in Section 5.4 and 5.5, respectively.

5.2 IRI-2012 model with topside density option

The representation of topside EDP in the IRI model was primarily based on a scheme of Rawer et al. (1978), an improved scheme from analytical model of Bent et al. (1972), and data sources of Alouette 1 topside sounder satellite. The first option of field “Ne topside” was proposed in the IRI-2001 model and named as “IRI2001” option. Afterwards, due to the availability of the Alouette 2, ISIS 1, and ISIS 2 topside sounder data sources, Bilitza (2004) evaluated the topside formula of IRI2001 option in the IRI-2001 model and then proposed a correction term for those formula. This improved option was designated as “IRI01-corr” option and started to be used in the IRI-2007 model till now. In addition, the third topside modeling was the “NeQuick” option (Bilitza et al., 2006) which was also started in the IRI-2007 model. This NeQuick option is based on both the NeQuick topside formulation of the

This material is reserved for educational use only, not allowed for commercial use.

Forbidden to modify the content, and cite the document when use.

NeQuick 2 model and the IRI parameters to compute the topside electron density (Coïsson et al., 2009). Another main parameter to gather other IRI-2012 parameters is the B0 of either Bil-2000 or Gul-1987 option. The related k values in (5.5) have been determined using either the B0 of Bil-2000 or the B0 of Gul-1987 instead of the NeQuick B2bot which are designated by k_{BOT} and k_{BOG} , respectively. Additional descriptions can be read in Coïsson et al. (2009).

In this thesis, the parameters of the IRI-2012 model are selected as follows: the B0 is Gul-1987 option, F peak model is CCIR, foF2 Storm model is off, Ne topside are NeQuick, IRI01-corr, and IRI2001 options, the remaining parameters are default values, and the heights vary from the $hmF2$ to 1,400 km (an upper boundary constant). This largest height is equal to 1,400 km, because the topside experimental data for the IRI and the NeQuick 2 models are obtained from ISIS 2 topside sounder satellite whose height is fixed at about 1,400 km. Moreover, the reason for selecting the B0 with Gul-1987 in this thesis is that the diurnal variations of the B0 with Gul-1987 are generally more similar to those of the observed B0 of Digisondes (B0_obs) than those of the B0 with Bil-2000 (Zhang et al., 2008). The IRI-2012 model is accessible on a web site http://omniweb.gsfc.nasa.gov/vitmo/iri2012_vitmo.html.

5.3 Comparison results of topside EDPs and topside TECs

The NeQuick-derived topside EDPs at Chumphon are compared with those of three Ne topside options of the IRI-2012 model, i.e., NeQuick, IRI01-corr, and IRI2001, in this section. In each figure, the black solid line denotes the Chumphon topside EDPs which is named shortly by “Chumphon.” Moreover, the black dashed line, the black dotted line, and the black dash-dot line denote the topside EDPs of three options of the IRI-2012 model designated by “IRINeQ,” “IRI01cor,” and “IRI2001,” respectively. In Figure 5.1, it can be seen that the Chumphon topside EDPs are closer to the IRI01cor topside EDPs than the others on January 15th, 2007. The Chumphon topside EDPs are at the rightmost positions at the altitudes between the $hmF2$ and 700 km from pre-sunrise to post-sunset hours, except at 03 LT. The IRI2001 topside EDPs are at the rightmost positions, whereas the IRINeQ ones are at the leftmost positions at the altitudes above 700 km.

This material is reserved for educational use only, not allowed for commercial use.

Forbidden to modify the content, and cite the document when use.

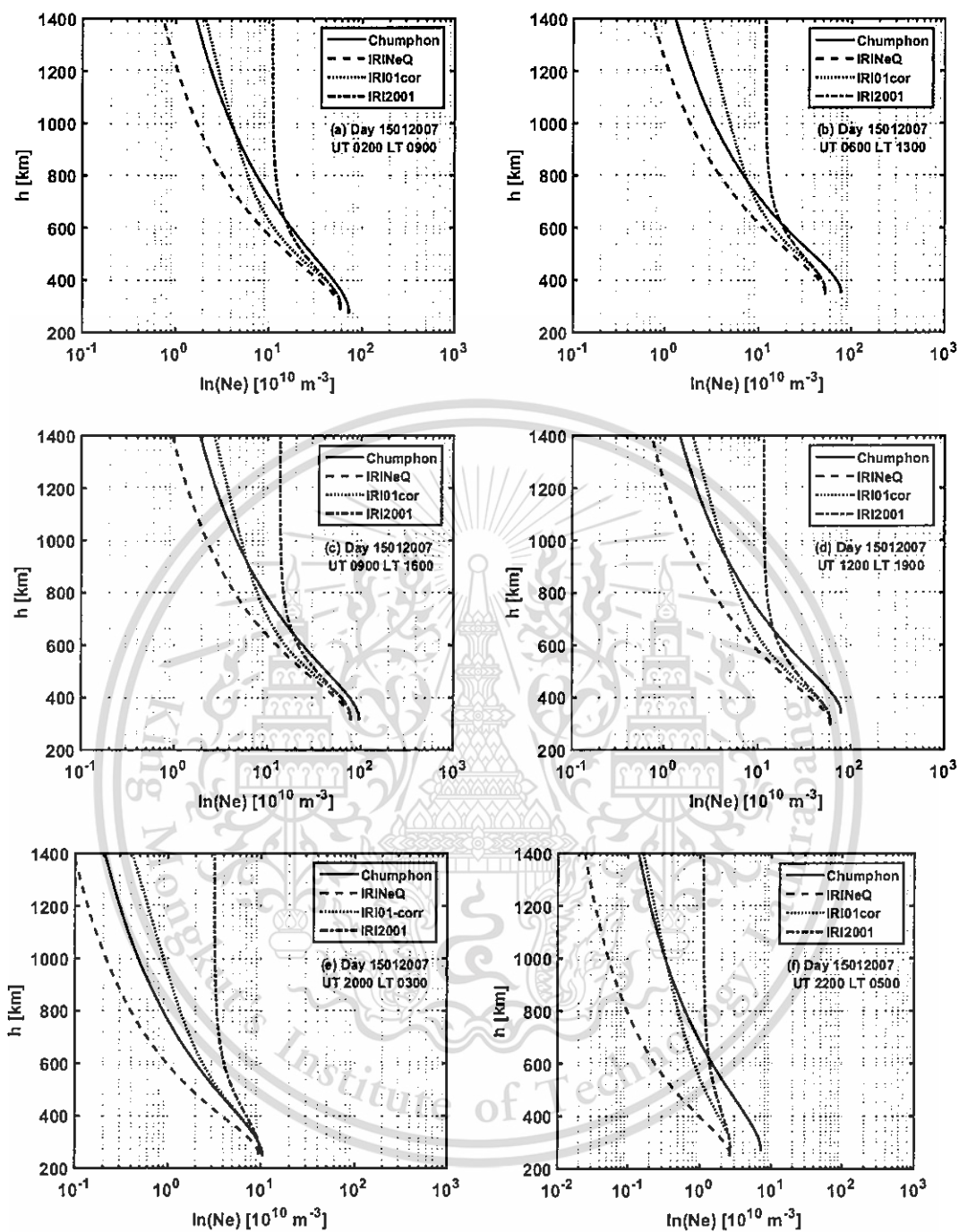


Figure 5.1 Topside Electron density profiles at different local times on January 15th, 2007.

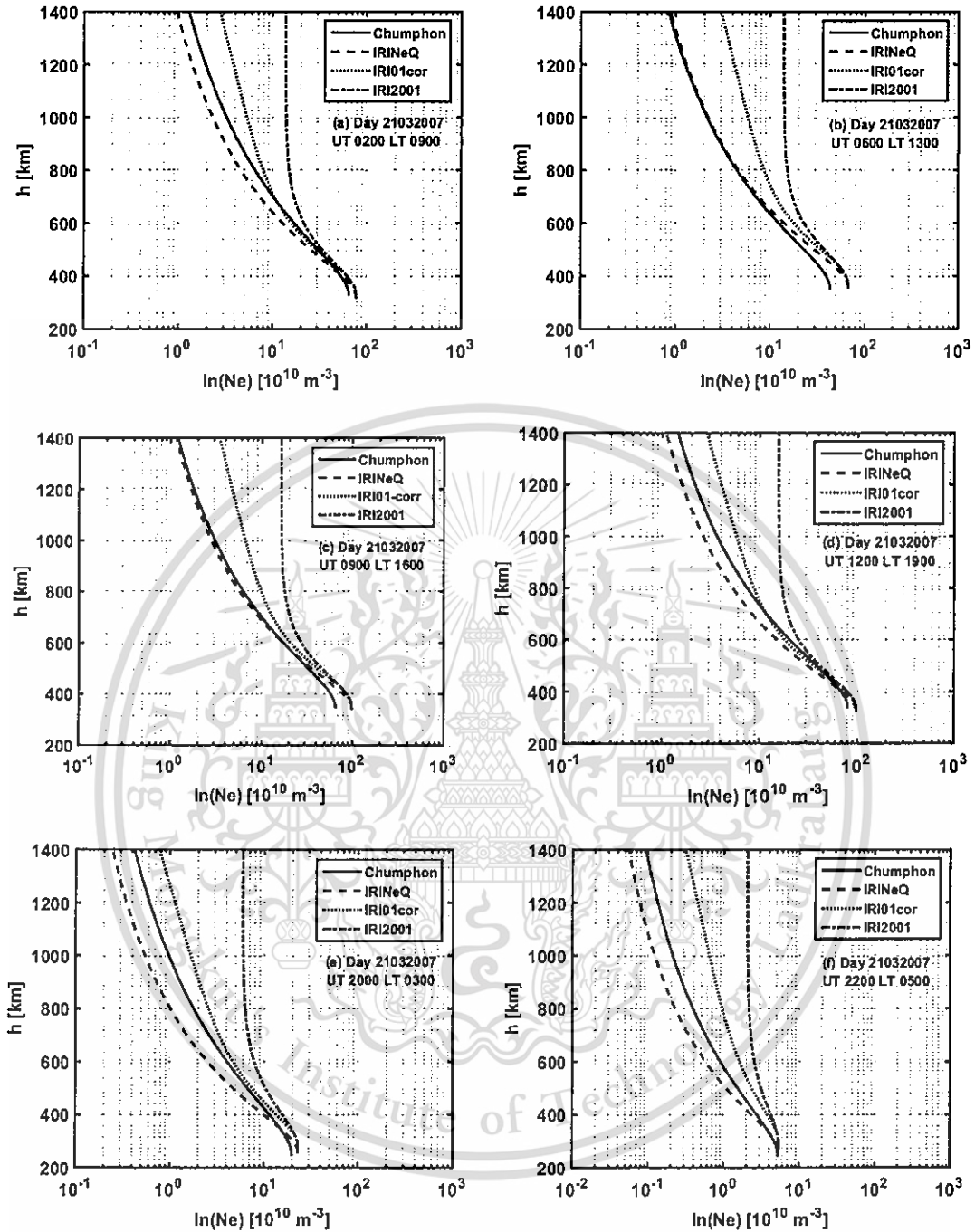


Figure 5.2 Topside Electron density profiles at different local times on March 21st, 2007.

In Figure 5.2, the Chumphon topside EDPs are closer to the IRINeQ topside EDPs than both the IRI01cor and the IRI2001 topside EDPs on 21 March, 2007. The IRI2001 topside EDPs are at the rightmost positions, while the IRINeQ ones always are

at the leftmost positions, except at 13 LT. The Chumphon topside EDP starts to be at the leftmost position at 13 LT and lasts until 16 LT at the altitudes between the $hmF2$ and 550 km.

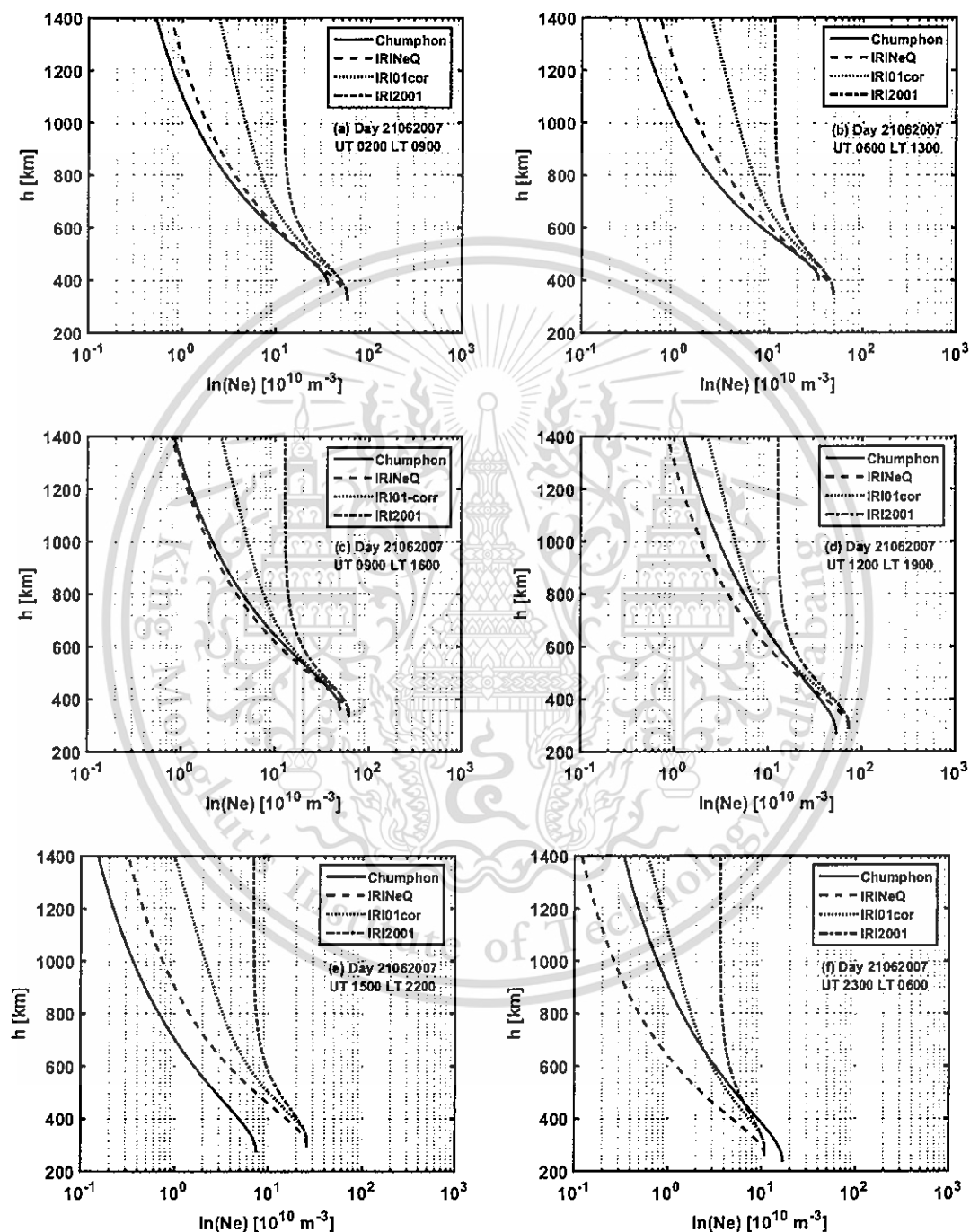


Figure 5.3 Topside Electron density profiles at different local times on June 21st, 2007.

This material is reserved for educational use only, not allowed for commercial use.

Forbidden to modify the content, and cite the document when use.

For the results on June 21st, 2007 in Figure 5.3, it can be seen that the Chumphon topside EDPs are also closer to the IRINeQ topside EDPs than both the IRI01cor and the IRI2001 topside EDPs, except at 06 LT where they are close to IRI01cor ones instead. The IRI2001 topside EDPs always are at the rightmost positions, except at 06 LT where the Chumphon topside EDPs are at the rightmost positions at the altitudes between the *hmF2* and 430 km.

Furthermore, Tables 5.1-5.3 show the integration of absolute differences (IAD_IRI) which are calculated by (5.6) and related directly to Figures 5.1-5.3. In Table 5.1, the IAD_IRI01cor are lower than the others from 0.40–7.07 TECU, because the Chumphon topside EDPs are generally closer to the IRI01-cor ones, especially at the heights higher than 700 km. The IAD_IRI values are lower during 09-13LT than the pre-sunrise hours. Therefore, these results identify that the modeling of topside EDP with the IRI01-corr option needs to be further insisted if it is a prosper profiler over Chumphon station on January 15th, 2007 (winter).

From Table 5.2, the IAD_IRINeQ are lower than others from 0.21-3.19 TECU, because the Chumphon topside EDPs are generally closer to the IRINeQ ones. The IAD_IRI values are the lowest values at 13LT and the highest values at different local times. Hence, these results identify that the modeling of topside EDP with the NeQuick option needs to be further confirmed if it is a prosper profiler over Chumphon station on March 21st, 2007 (equinox).

In Table 5.3, the IAD_IRINeQ are often the lowest values ranging from 1.32-3.38 TECU, because the Chumphon topside EDPs are often closer to the IRINeQ ones. Meanwhile, the IAD_IRI01cor and the IAD_IRI2001 are higher ranging from 0.91-5.62 TECU and 2.73-12.12 TECU, respectively. These three values are the lowest values and the highest values at different local times. Hence, these studied results identify that the topside modeling with the NeQuick option needs to be further confirmed if it is a prosper profiler during at Chumphon station on June 21st, 2007 (summer).

The overall results in Figures 5.1-5.3 show that both the NeQuick-derived and IRI2012-predicted topside electron density values over Chumphon increase during daytime hours and decrease during nighttime hours. The IRI2001, IRI01cor, and IRINeQ topside EDPs are generally at the rightmost, the middle, and leftmost positions for all

This material is reserved for educational use only, not allowed for commercial use.

the studied times with the same *hmF2*, dates, and local times. For the Chumphon topside EDPs, they are clearly at the rightmost positions on January 15th between the *hmF2* and 700 km, while they are often at either the middle or the leftmost positions on March 21st and June 21st. The Chumphon topside EDPs are closer to the IRI01cor ones for all the local times in the winter season. Likewise, the Chumphon topside EDPs are closer to the IRINeQ ones for all the local times in the equinox and summer seasons.

Table 5.1 The results of IAD_IRI values at different local times on January 15th, 2007.

LT	IAD_IRINeQ	IAD_IRI01cor	IAD_IRI2001
9	0.8206	0.3965	2.5876
13	1.4056	0.9475	1.329
16	6.4077	3.7683	6.9954
19	2.4758	2.9928	8.5435
3	7.9658	5.2586	9.4386
5	10.067	7.065	9.581

Table 5.2 The results of IAD_IRI values at different local times on March 21st, 2007.

LT	IAD_IRINeQ	IAD_IRI01cor	IAD_IRI2001
9	1.0579	1.2163	5.3029
13	0.2078	0.6382	1.927
16	2.5355	2.7195	9.8665
19	1.665	5.05	12.152
3	2.769	3.225	11.605
5	3.186	3.12	11.237

Table 5.3 The results of IAD_IRI values at different local times on June 21st, 2007.

LT	IAD_IRINeQ	IAD_IRI01cor	IAD_IRI2001
9	1.8488	0.9095	2.7252
13	2.323	5.623	12.122
16	2.079	5.101	10.95
19	1.317	3.463	10.229
22	3.3849	2.4658	8.9951
6	3.1569	5.1009	9.5828

The results of topside EDPs in this thesis differ from the work of Stankov et al. (2003) in which the average topside EDPs obtained from AE-C satellite in situ measurements during nighttime are best characterized by the Epstein formulas (e.g. the NeQuick 2 model), whereas the ones during daytime are better described by the exponential functions or α -Chapman functions. Furthermore, we also find that the IRI2001 topside EDPs are often at the rightmost positions for all studied dates and months which are in good agreement with those in Rathore et al. (2015). The Chumphon topside EDPs are often above the IRINeQ ones as illustrated in Figures 5.1-5.3. Here, although the Chumphon topside EDPs are the simulated ones which are based on NeQuick topside formulation, they are in good agreement with the results of Coisson et al. (2008a) at low latitudes during high solar activity where the NeQuick 2 model underestimates the topside electron density profiles.

5.4 Comparison results of topside TEC values

The topside TEC values over Chumphon of both NeQuick-derived and the IRI2012-predicted topside EDPs are calculated in conjunction with the AD_NeQ parameter determined by (5.7). Tables 5.4-5.6 demonstrate the topside TEC and AD_NeQ values at different local times on January 15th, March 21st, and June 21st in 2007, respectively. The topside TEC values at Chumphon are the vertical TEC which are determined by the integration on Chumphon topside EDPs from the *hmF2* to

This material is reserved for educational use only, not allowed for commercial use.

1,400 km at each date and time. Moreover, the topside TEC (Unit: TECU) of each option in field “Ne topside” of the IRI-2012 model is calculated using the product between the percentage of TEC top and TEC. For instance, at 13 LT (06 UT) on June 21st, 2007, when considering the height from 347-1,400 km, the percentage of TEC top and TEC of IRI01-corr are equal to 62.6% and 19.5 TECU, respectively. The topside TEC is thus equal to 12.21 TECU as shown in Table 5.6. Other topside TECs of the IRI-2012 model can be computed using the values on a web site http://omniweb.gsfc.nasa.gov/vitmo/iri2012_vitmo.html.

From Table 5.4, the topside TECs of tT_CPN , $tT_IRI2001$, $tT_IRI01cor$, and tT_IRINeQ decrease sequentially at the same local times, except at 03 LT in which the $tT_IRI2001$ is the highest level about 5 TECU. The AD_NeQ are higher than 13 TECU from post-sunrise to post-sunset hours, while they are about 2 TECU during pre-sunrise hours. From the results in Table 5.5, the $tT_IRI2001$ always are the highest levels and the tT_IRINeQ always are the lowest levels. The AD_NeQ on March 21st range from 0.86 to 8.07 TECU. From Table 5.6, the $tT_IRI2001$ always are the highest levels, except at 06 LT where the tT_CPN is the highest level. The remaining topside TECs including tT_CPN , tT_IRINeQ , and $tT_IRI01cor$ are the decreasing values. The AD_NeQ on June 21st, 2007 generally range from 1.04 to 6.94 TECU with the highest value at 19 LT. This highest absolute difference is caused by different $NmF2$ and $hmF2$ values. The observed and IRI-predicted $NmF2$ values are equal to 5.40×10^{11} eV/m³ and 7.40×10^{11} eV/m³, respectively, whereas the observed $hmF2$ and the IRI-predicted $hmF2$ are equal to 273 km and 291 km, respectively.

The concluded results in Tables 5.4-5.6 indicate that the IRI-derived topside TEC, including $tT_IRI2001$, $tT_IRI01cor$, and tT_IRINeQ , often decrease sequentially for all studied dates and months. The tT_CPN are the highest levels, the middle levels, and the lowest levels on January 15th, March 21st, and June 21st, respectively. The diurnal variations of both IRI-derived and computed topside TECs generally have the similar trends one another for all studied dates and months. It can be seen that they are the lowest levels during pre-sunrise hours and the highest levels during 16-19 LT. The IRI-derived topside TEC and tT_CPN values are the highest levels identically at 16 LT on January 15th and at 19 LT on June 21st. Likewise, they are also the highest

This material is reserved for educational use only, not allowed for commercial use.

levels in different local times on March 21st, i.e., at 16 LT and 19 LT, respectively. The tT_CPN are often higher than the $IRINeQ$, especially on January 15th (winter) and on March 21st (equinox) as demonstrated in Tables 5.4 and 5.5. The topside TECs in this thesis are in agreement with the TECs in previous publications (e.g. Rathore et al., 2015; Coïsson et al., 2004). Rathore et al. (2015) investigated and compared the IRI-predicted TECs with GPS TECs over Varanasi, India, during 2012 and 2013. They disclosed that the averaged TECs with IRI2001 option always are higher than the others and the averaged GPS TECs match the TECs with IRI-NeQuick option in summer of year 2012. Furthermore, during 13:30-15:30 LT, GPS TECs match the TECs satisfactorily with IRI-NeQuick and IRI01-corr options. For all seasons, they also inferred that the TECs using the NeQuick and IRI01-corr options are generally closer to the GPS TECs compared with the IRI2001 option. The TEC variations in Rathore et al. (2015) are in good agreement with the topside EDP variations in this thesis. Here, the Chumphon topside EDPs are closer to the IRI01cor ones in the winter season and to the $IRINeQ$ ones in the equinox and summer seasons. Furthermore, Coïsson et al. (2004) revealed that the NeQuick TECs have a tendency to underestimate the observed TECs, therefore, the Chumphon topside EDPs are often above the $IRINeQ$ ones as demonstrated in Figures 5.1-5.3.

Table 5.4 Topped TEC and AD_NeQ values on January 15th, 2007.

LT	tT_CPN	tT_IRINeQ	$tT_IRI01cor$	$tT_IRI2001$	AD_NeQ
9	26.33	10.73	13.73	20.02	15.6
13	22.70	9.79	12.93	19.02	12.91
16	31.43	13.78	17.25	24.74	17.65
19	30.28	11.26	13.96	20.86	19.02
3	3.64	1.61	2.80	5.00	2.03
5	2.45	0.39	0.88	1.58	2.06

Table 5.5 Topside TEC and AD_NeQ values on March 21st, 2007.

LT	tT_CPN	tT_IRINeQ	tT_IRI01cor	tT_IRI2001	AD_NeQ
9	21.23	14	17.41	25.01	7.23
13	13.6	11.89	15.68	22.79	1.71
16	20.25	16.76	21.04	29.66	3.49
19	24.64	16.57	20.26	29.29	8.07
3	7.1	3.95	5.84	9.94	3.15
5	1.73	0.87	1.75	3.05	0.86

Table 5.6 Topside TEC and AD_NeQ values on June 21st, 2007.

LT	tT_CPN	tT_IRINeQ	tT_IRI01cor	tT_IRI2001	AD_NeQ
9	9.5	10.54	13.83	20.31	1.04
13	7.97	9.09	12.21	17.96	1.12
16	14.44	11.01	14.59	21.31	3.43
19	19.9	12.96	16.35	23.95	6.94
22	2.57	4.67	6.66	11.06	2.1
6	5.99	1.95	3.37	5.56	4.04

5.5 Comparison results between IGS TECs and topside TECs

Some topside TECs in Tables 5.4-5.6 are taken to compare with the IGS TEC values and to show the differences (D_{tT}) using (5.8) in this section. The IGS TEC values are retrieved from the International GNSS service on the same dates and local times via the IGS homepage at <ftp://cddis.gsfc.nasa.gov/gps/products/ionex>. The IGS TEC, some topside TECs, and the D_{tT} at different local times on January 15th, March 21st, and June 21st in 2007 are shown in Tables 5.7-5.9, respectively. Here, the tT_{CPN} , the $tT_{IRI01cor}$, and the $tT_{IRI2001}$ from Tables 5.4-5.6 are demonstrated again in order to compare with the IGS TECs. It is well-known that the IGS TECs are computed up to 22,000 km and should be higher than the topside TECs of 3 models (NeQuick topside formulation, IRI01-corr option, and IRI2001 option). However, some

This material is reserved for educational use only, not allowed for commercial use.

negative D_{tT} values appear in these tables. These errors should not take place, because the IGS TEC covers longer distances. The tT_{IRINeQ} always are lower than the IGS TEC for all studied dates and local times, the differences between the IGS TEC and the tT_{IRINeQ} always are positive. Hence, the tT_{IRINeQ} values and their positive differences are not illustrated in Tables 5.7-5.9.

In Table 5.7, the tT_{CPN} are higher than the IGS TEC at 09 LT, 16 LT, and 19 LT, and the $tT_{IRI2001}$ are also higher than the IGS TEC at 09 LT and 19 LT. Hence, the D_{CPN} and the $D_{IRI2001}$ are negative at these local times. In Tables 5.8 and 5.9, the $D_{IRI2001}$ are negative during nighttime from 19 - 03 LT and at 09 LT on March 21st and June 21st. Likewise, the D_{CPN} are negative at 09 LT on March 21st and 19 LT on June 21st. The $tT_{IRI01cor}$ are often lower than the IGS TEC for all studied dates and local times, except at 19 LT on June 21st, as shown in Table 5.9, hence, the $D_{IRI01cor}$ value is only negative at 19 LT on June 21st.

Descriptions for the variation phenomena in topside TECs and IGS TECs are described additionally as follows. Verhulst and Stankov (2014) indicated that the ionospheric characteristics - $NmF2$, $hmF2$, and so on - are associated with the shape of topside EDP and a single parameter are not able to be used as a decision factor for selecting an appropriate topside profiler. Historical topside sounder data are analyzed and taken to indicate that there is a correlation between the shape of topside EDPs and the TECs. Therefore, they advised that the slab thickness and the TEC have to be used along with one or more ionospheric characteristics in order to choose the best profiler for modeling the topside EDPs. Furthermore, we think that the topside TECs with those negative D_{tT} values can be lower than the IGS TEC, if either the slab thickness or the TEC is used possibly as a main parameter in the analytical functions of three models (i.e. NeQuick topside formulation, IRI01cor option, and IRI2001 option) for computing topside TECs as well as modeling topside EDPs.

Table 5.7 IGS TEC, some topside TEC, and D_tT values on January 15th, 2007.

LT	IGS TEC	tT_CPN	tT_IRI01cor	tT_IRI2001	D_CPN	D_IRI01cor	D_IRI2001
9	15.22	26.33	13.73	20.02	-11.11	1.49	-4.8
13	29.11	22.7	12.93	19.02	6.41	16.18	10.09
16	28.19	31.43	17.25	24.74	-3.24	10.94	3.45
19	19.7	30.28	13.96	20.86	-10.58	5.74	-1.16
3	5.38	3.64	2.8	5	1.74	2.58	0.38
5	4.39	2.45	0.88	1.58	1.94	3.51	2.81

Table 5.8 IGS TEC, some topside TEC, and D_tT values on March 21st, 2007.

LT	IGS TEC	tT_CPN	tT_IRI01cor	tT_IRI2001	D_CPN	D_IRI01cor	D_IRI2001
9	17.67	21.23	17.41	25.01	-3.56	0.26	-7.34
13	29.7	13.6	15.68	22.79	16.1	14.02	6.91
16	30.2	20.25	21.04	29.66	9.95	9.16	0.54
19	25.26	24.64	20.26	29.29	0.62	5	-4.03
3	8.69	7.1	5.84	9.94	1.59	2.85	-1.25
5	5.46	1.73	1.75	3.05	3.73	3.71	2.41

Table 5.9 IGS TEC, some topside TEC, and D_tT values on June 21st, 2007.

LT	IGS TEC	tT_CPN	tT_IRI01cor	tT_IRI2001	D_CPN	D_IRI01cor	D_IRI2001
9	16.1	9.5	13.83	20.31	6.6	2.27	-4.21
13	22.15	7.97	12.11	17.96	14.18	10.04	4.19
16	21.37	14.44	14.59	21.31	6.93	6.78	0.06
19	15.55	19.9	16.35	23.95	-4.35	-0.8	-8.4
22	6.74	2.57	6.66	11.06	4.17	0.08	-4.32
6	6.76	5.99	3.37	5.56	0.77	3.39	1.2

CHAPTER 6

SATELLITE DELAY PROFILES

Radio wave from a satellite traveling through the ionosphere suffers refraction and retardation which lead to time delays. These ionospheric delays are closely related to the total electron content (TEC) in ionosphere and should be corrected for any satellite systems, such as, global navigation satellite system (GNSS) and global positioning system (GPS). Furthermore, TEC is also used to study about the variations of electron density in ionosphere. Hence, it is necessary to have accurate TEC models and reliable TEC measurements for both correcting ionospheric delays and knowing the variations in electron density exactly. Most of TEC measurements have employed the Faraday rotation technique, TOPEX (The ocean topography experiment) surface reflection, incoherent scatter radar (ISR), ground-based ionosondes (ionogram-derived TEC or ITEC), and dual-frequency GPS observation (GPS TEC) etc. Here, GPS TEC is described only so as to make research in this work. GPS TEC is measured along a signal ray path between a satellite and a GPS receiver and assumed to combine all the electrons in a column with a cross section of 1 m^2 extending from the GPS receiver to the satellite. TEC is measured in TEC unit (TECU) that $1 \text{ TECU} = 10^{16} \text{ electrons/m}^2$. Computing GPS TEC in ionosphere is based on a relationship between the differences in time delays of 2 carrier frequencies of GPS satellite: $L1 = 1.57542 \text{ GHz}$ and $L2 = 1.22760 \text{ GHz}$. Each data signal is transmitted from a GPS satellite with different two frequencies. They reach to a GPS receiver with different time delays due to different frequencies and they also are effected differently by the ionospheric refractive indices. Moreover, the ionospheric time delays lead to the increased distance and time for reaching to a receiver and the varying phase which is described briefly in the next section. Also, the GPS TEC measured by Chumphon station, Thailand is named by the observed TEC in this chapter which is compared with the other two TEC values, i.e., the IRI TEC and the IGS TEC.

This material is reserved for educational use only, not allowed for commercial use.

Forbidden to modify the content, and cite the document when use.

6.1 Comparison results of TECs

In general, the TEC values have the same diurnal variations for all three methods in winter and equinox seasons, except those in summer season, as shown in Figures 6.1(a) and (c). They begin to increase around pre-sunrise hours (05-07 LT) to the diurnal peaks at a period of 10-19 LT, and then decrease gradually until pre-sunrise hours. It is worthy to note that the IGS TEC have another small peaks at 01 LT, and only the IRI TEC and the IGS TEC encounter bite-out phenomena during their diurnal peaks.

On the other hand, in Figure 6.1(e), the observed TEC in summer season start increasing at 00 LT and achieve a highest peak around 10 LT. Two small peaks can be seen at 04 LT and 15 LT, and two TEC collapses are also found during 04-07 LT and 10-12 LT, respectively. Both the IGS TEC and the IRI TEC in summer season still have the same diurnal variations as those in the other two seasons. The IRI TEC start increasing around 05 LT to reach its maximum values around 09-18 LT (9 hours), and then decrease slowly until pre-sunrise hours. Meanwhile, the IGS TEC begin increase at 07 LT to achieve its maximum values around 17-19 LT, and then decrease gradually until 07 LT. Here, Tables 6.1-6.3 illustrate both Minima and Maxima of TEC values in winter, equinox, and summer seasons, 2015, respectively which corresponds to the descriptions of TEC values. The absolute differences of VTEC (Unit: TECU) for all three seasons in 2015 are shown in Figures 6.1(b), (d) and (f). In Figure 6.1(b), the D_{IGS} values in the winter season are lower than 7.53 TECU during daytime from 07 to 15 LT and 23 LT, while they are higher than 8 TECU at the remaining local times.

Table 6.1 Minima and Maxima of TEC values in winter season, 2015.

Parameters	Observed TEC (TECU)	IRI TEC (TECU)	IGS TEC (TECU)
Times of Minima	06 LT	05 LT	07 LT
Minimum Values	1.32	4.05	10.04
Times of Maxima	14-16 LT	10-16 LT	15-19 LT
Maximum Values	58.25	40.15	60.34

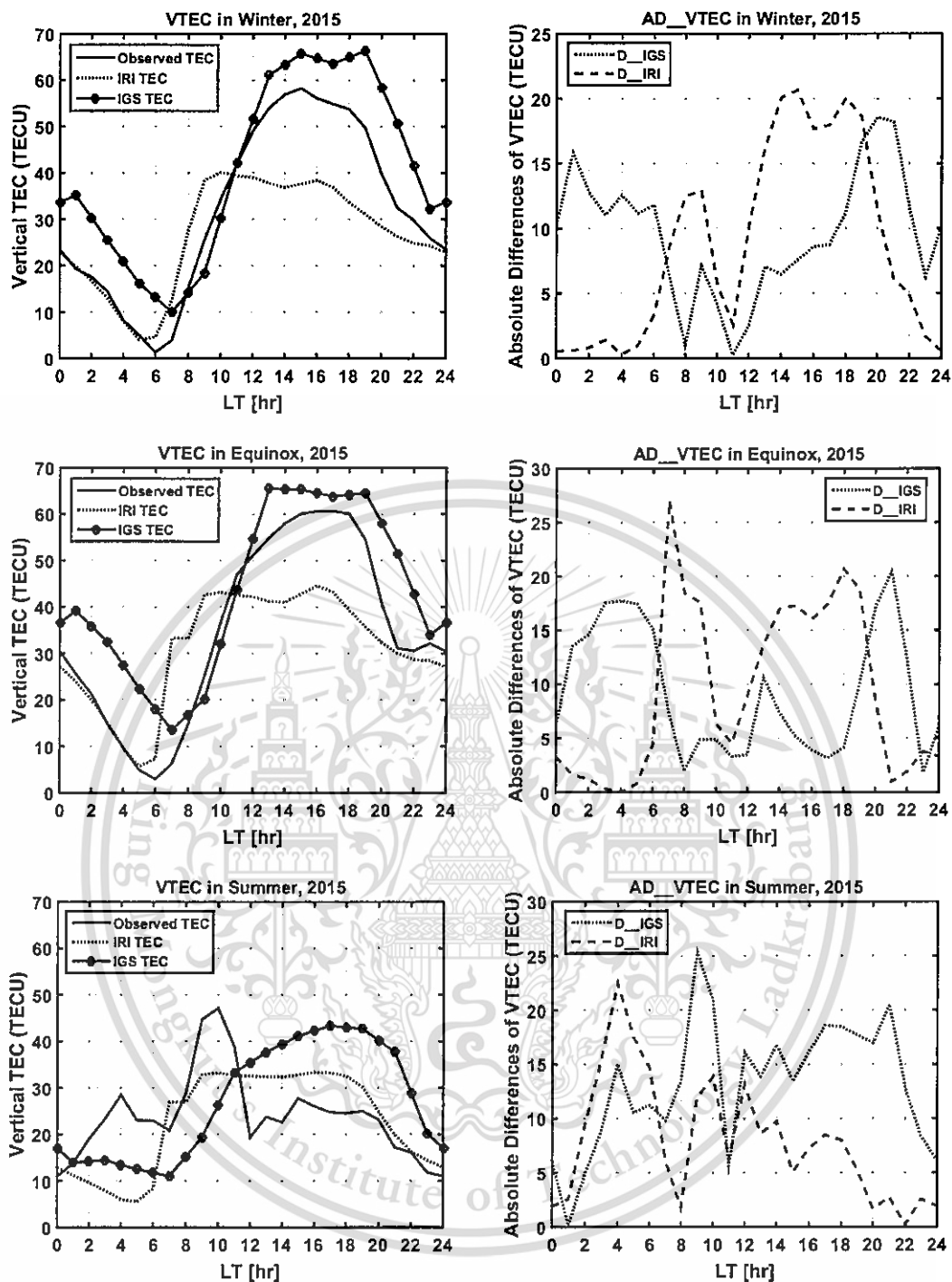


Figure 6.1 Vertical TECs and their absolute differences during three seasons.

Meanwhile, the D_{IRI} values in the winter season are lower than 6.15 TECU from 21 to 06 LT. For the equinox season in Figure 6.1(d), the D_{IGS} values are lower than 7.36 TECU during daytime with a longer duration from 07 to 18 LT and 23 to 24 LT, except 13 LT where they are high of 10.64 TECU. Meanwhile, the D_{IRI} values are

lower than 4.48 TECU during nighttime from 21 to 06 LT. In the summer season in Figure 6.1(f), the D_{IGS} values are lower than 6.05 TECU from 00 to 02 LT and 11 LT (only 4 hours in each day), whereas they are higher than 8 TECU at the remaining local times. The D_{IRI} values are lower than 7.29 TECU during daytime and nighttime hours about half-day variation.

Table 6.2 Minima and Maxima of TEC values in equinox season, 2015.

Parameters	Observed TEC (TECU)	IRI TEC (TECU)	IGS TEC (TECU)
Times of Minima	06 LT	05 LT	07 LT
Minimum Values	2.93	5.70	13.55
Times of Maxima	15-18 LT	10-16 LT	13-19 LT
Maximum Values	60.64	44.60	65.50

Table 6.3 Minima and Maxima of TEC values in summer season, 2015.

Parameters	Observed TEC (TECU)	IRI TEC (TECU)	IGS TEC (TECU)
Times of Minima	00 LT	05 LT	07 LT
Minimum Values	10.98	5.55	11.03
Times of Maxima	10 LT	9-18 LT	17-19 LT
Maximum Values	47.15	33.35	43.35

6.2 Comparison results of ionospheric delays

Since the ionospheric delays are proportional to the TEC values, hence, the diurnal variations in ionospheric delays are the same as those in TEC values for all three methods as illustrated in Figures 6.2(a), (c), and (e). The characteristics of ionospheric delays are not described repeatedly in this part. Note that, for all three studied methods, the diurnal variations of ionospheric delays in the winter season are only the same trends as those in the equinox season as shown in Figures 6.2(a) and (c). Likewise, the variations in two absolute differences of ionospheric delays (Unit: ns) are also the same as those of TEC values for all three methods as shown in Figures 6.2(b), (d), and (f). For the winter season in Figure 6.2(b), the Δ_{IGS} values

are lower than 4.08 ns during daytime from 07 to 15 LT and 23 LT, whereas the Delta_IRI values are lower than 3.33 ns during nighttime from 21 to 06 LT.

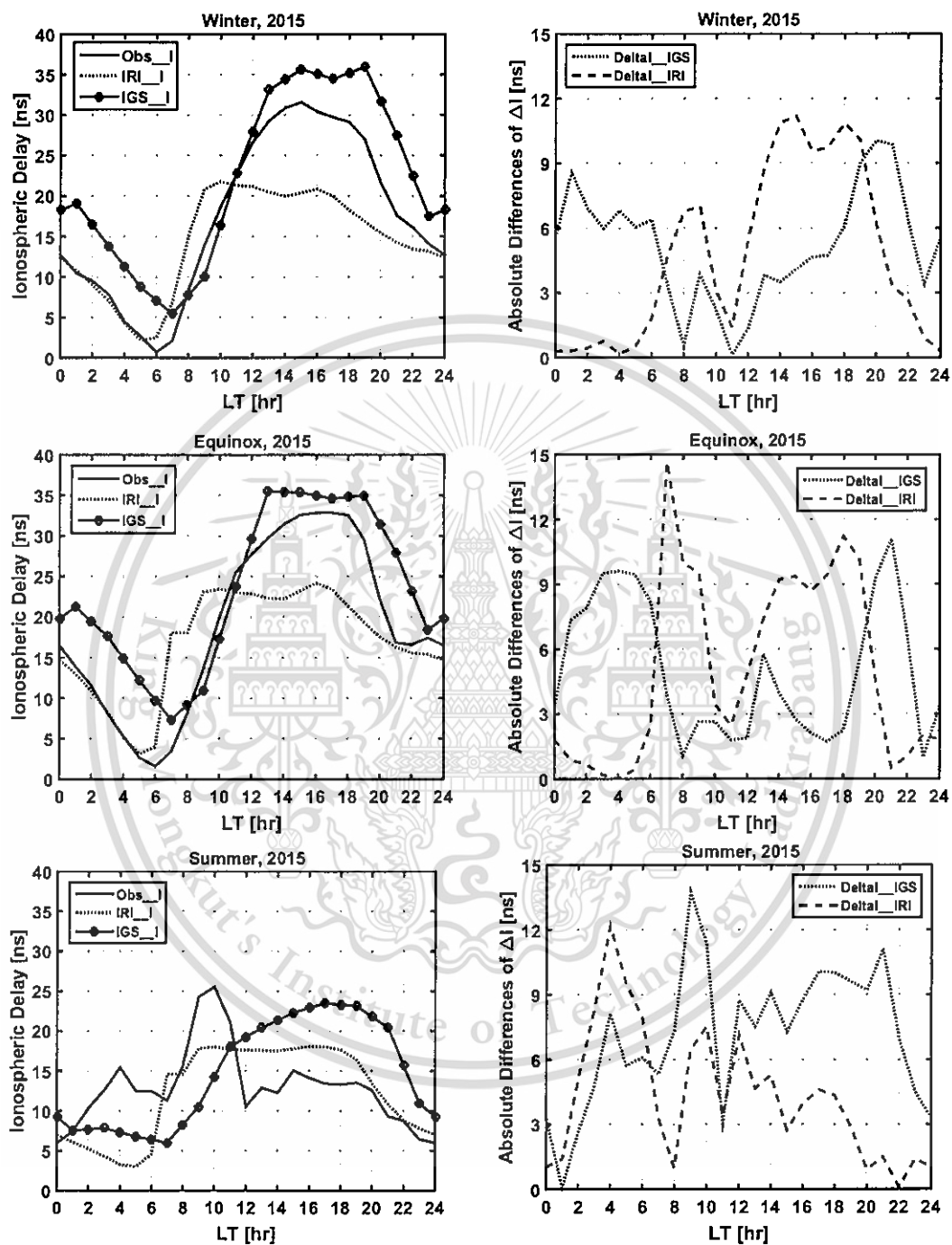


Figure 6.2 Ionospheric delays and their absolute differences for winter, equinox, and summer 2015.

For the equinox season in Figure 6.2(d), the Delta_IGS values are lower than 3.99 ns during daytime with a longer duration from 07 to 18 LT and 23 to 24 LT, except 13 LT where they are high of 5.77 TECU. Meanwhile, the Delta_IRI values are lower than 2.43 ns during nighttime from 21 to 06 LT. In the summer season in Figure 6.2(f), the Delta_IGS values are lower than 3.28 ns from 00 to 02 LT and 11 LT (4 hours) and the Delta_IRI values are lower than 3.95 ns during daytime and nighttime hours (about 12 hours). Tables 6.4-6.6 also show both Minima and Maxima of ionospheric delays for all three seasons in 2015.

Table 6.4 Minima and Maxima of ionospheric delays in winter season, 2015.

Parameters	Observed Delay (ns)	IRI Delay (ns)	IRI Delay (ns)
Times of Minima	06 LT	05 LT	07 LT
Minimum Values	0.72	2.19	5.44
Times of Maxima	14-16 LT	10-16 LT	15-19 LT
Maximum Values	31.57	21.76	35.95

Table 6.5 Minima and Maxima of ionospheric delays in equinox season, 2015.

Parameters	Observed Delay (ns)	IRI Delay (ns)	IRI Delay (ns)
Times of Minima	06 LT	05 LT	07 LT
Minimum Values	1.59	3.09	7.34
Times of Maxima	15-18 LT	10-16 LT	13-19 LT
Maximum Values	32.86	24.17	35.50

Table 6.6 Minima and Maxima of ionospheric delays in summer season, 2015.

Parameters	Observed Delay (ns)	IRI Delay (ns)	IRI Delay (ns)
Times of Minima	00 LT	05 LT	07 LT
Minimum Values	5.95	3.01	5.97
Times of Maxima	10 LT	9-18 LT	17-19 LT
Maximum Values	25.55	18.07	23.49

CHAPTER 7

CONCLUSIONS

7.1 Summary

This thesis proposes three ionospheric research topics over Chumphon station, Thailand. These topics include 1) present a new expression for computing the bottomside thickness parameter of the NeQuick 2 model, 2) depict topside electron density profiles, and 3) compute ionospheric delays.

For first topic, the bottomside thickness parameters of the NeQuick 2 model (B2bot) over Chumphon station are studied and analyzed in Chapter 4. After a new equation for computing the B2bot is derived and named as B2bot_Pro in this thesis, two main ionospheric parameters used to compute the new B2bot_Pro in this thesis are TEC and slab thickness, hence, the well-known results about TEC and slab thickness during 2004-2006 of Kenpankho et al. (2011) is used in this task so as to make the computed B2bot_Pro reliable and acknowledgeable. The diurnal variations of the B2bot_Pro are also compared with those of the B2bot_NeQ (original B2bot of the NeQuick model) and the IRI B0 values (B0_ABT and B0_Bil). The results of a new proposed B2bot (B2bot_Pro) can be summarized as follows.

1. The diurnal variations in both the B2bot_Pro and the B2bot_NeQ are higher during daytime and their diurnal peaks take place during 10-14 LT for all seasons. Both the B2bot_Pro and the B2bot_NeQ show similar diurnal variations, but the B2bot_NeQ are mainly larger than the B2bot_Pro, except during pre-sunrise. The beginning local times of the B2bot_Pro are only the same period as those of the B2bot_NeQ during equinoxes. The pre-sunrise peaks and the sunrise collapses in both the B2bot_Pro and the B2bot_NeQ are also found, but those in the B2bot_NeQ are lower values. The sunrise collapses in B2bot_Pro during the winters are stronger than those during the summers and equinoxes, respectively. The averaged

percentage deviations between the B2bot_NeQ and the B2bot_Pro (PD_B2bot) are mostly greater than 30%, especially during pre-sunrise.

2. For Both the B0_ABT and the B2bot_Pro generally illustrate similar diurnal variations for all seasons. The B0_ABT are mostly larger than the B2bot_Pro, except pre-sunrise. The diurnal peaks in B0_ABT exist during a period of 10-14 LT for all seasons which is the same as those in B2bot_Pro. The B0_ABT begin increasing during nighttime to the diurnal peaks around local noontime, and then decrease slowly till their beginning local times. It is worthy to note that the pre-sunrise peaks in B0_ABT can sometimes be found during the winter and its sunrise collapses do not exist for all seasons. The averaged percentage deviations between the B2bot_Pro and the B0_ABT (PD_B2B0ABT) are mostly lower than 30% which are opposite to the other percentage deviations studied in this thesis.

3. For the B0_Bil, the diurnal variations in B0_Bil differ from those in B2bot_Pro due to its flattened diurnal variation. The B0_Bil start increasing at the midnight to the diurnal peaks around local noontime, and then decrease gradually until the midnight. For all seasons, the beginning times of the B0_Bil differ from those of the B2bot_Pro and the diurnal peaks in B0_Bil occur during 11-13 LT which is the same as those in B2bot_Pro. The pre-sunrise peak and the sunrise collapse in B0_Bil disappear unlike the B2bot_Pro and the B0_ABT. The averaged percentage deviations between the B2bot_Pro and the B0_Bil (PD_B2B0Bil) are mainly higher than 30%, especially during pre-sunrise.

For **Second topic**, the topside electron density values, topside electron density profiles (EDPs), and their topside TEC values using NeQuick topside formulation over Chumphon station are investigated and analyzed in Chapter 5. The duration for this second topic are only in 2007 where has nearly minimum solar activity among 24 solar cycles, and some equinoxes and solstice dates in 2007 are only chosen to study in this thesis. The results can be inferred as follows.

1. For all seasons, the topside EDPs with IRI2001, IRI01-corr, and NeQuick options of the IRI-2012 model are frequently at the rightmost, the middle, and the leftmost positions, respectively.

2. The Chumphon topside EDPs have the same tendencies as the IRINeQ ones, because they are calculated and illustrated using NeQuick topside formulation.

3. The NeQuick-derived topside EDPs at Chumphon on January 15th could be modelled properly by the IRI01-corr option of the IRI-2012 model. Likewise, the NeQuick-derived topside EDPs could be modelled properly by the NeQuick option of the IRI-2102 model at Chumphon for both March 21st and June 21st.

4. These results are in agreement with those of Verhulst and Stankov (2014; 2015) where the topside electron density distributions do not necessarily follow the Chapman profile, and they might be better modelled by other profile functions.

5. For the results of topside TEC values, the tT_{CPN} values are the highest levels, the middle levels, and the lowest levels on January 15th, March 21st, and June 21st, respectively.

6. The diurnal variations of both the IRI-derived and computed topside TEC values generally have the similar tendencies for all studied durations. The values of $tT_{IRI2001}$, $tT_{IRI01cor}$, and tT_{IRINeQ} frequently decrease sequentially.

7. The tT_{IRINeQ} are always lower than the IGS TEC observed at Chumphon, the differences between the IGS TEC and the tT_{IRINeQ} are always positive. The $tT_{IRI01cor}$ and the $tT_{IRI2001}$ are sometimes larger than the IGS TEC at Chumphon. Actually, any topside TECs should be lower than the (total) TECs <IGS TECs>. Therefore, to ensure that the computed topside TEC and the IRI topside TEC should be lower than the (total) TEC, the (total) TEC or the slab thickness might be possibly used to model the topside EDPs and compute the topside TECs for the NeQuick 2 and the IRI-2012 models.

For the last topic, the satellite delay profiles are explained in Chapter 6 where the TEC values as well as the ionosphere delays of GPS signal over Chumphon station in 2015 are only studied. Year 2015 is selected in this study, because the TECs are not available in several days and months in 2016, and year 2017 does not reach the end of year. The studied results of TEC values can be described as follows.

1. They have mostly the same diurnal variations for all three methods in winter and equinox seasons, except those in summer season. They start increasing around pre-sunrise to the diurnal peaks during 10-19 LT, and then decrease gradually

This material is reserved for educational use only, not allowed for commercial use.

until pre-sunrise. Note that the IGS TEC have another small peaks at 01 LT, and only the IRI TEC as well as the IGS TEC encounter bite-out phenomena during their diurnal peaks.

2. On the other hand, the observed TEC in summer season start increasing at 00 LT and achieve a highest peak around 10 LT. Two small peaks can be seen at 04 LT and 15 LT, and two TEC collapses are also found during 04-07 LT and 10-12 LT, respectively.

3. Both the IGS TEC and the IRI TEC in summer season still have the same diurnal variations as those in the other two seasons. They begin increasing during 05-07 LT to reach its maximum values around 09-19 LT, and then decrease slowly until pre-sunrise.

The diurnal variations in two absolute differences of TEC values for all three methods can be concluded as follows.

1. For winter and equinox seasons, it can be seen that the D_{IGS} values are lower than about 7.6 TECU during daytime, whereas the D_{IRI} values in the winter season are lower than about 6.2 TECU during nighttime.

2. For summer season, both the D_{IGS} and the D_{IRI} values are mostly higher than about 8 TECU during daytime and nighttime.

3. Moreover, since the ionospheric delays are proportional to the TEC values, hence, the diurnal variations in ionospheric delays are the same as those in TEC values for all three methods.

4. The diurnal variations of ionospheric delays in the winter season are only the same trends as ones in the equinox season.

5. Meanwhile, the variations in two absolute differences of ionospheric delays are also the same trends as those of TEC values for all three methods are summarized as follows.

6. For winter and equinox seasons, the Δ_{IGS} values are lower than about 4.1 ns during daytime, while the Δ_{IRI} values are lower than 3.4 ns during nighttime.

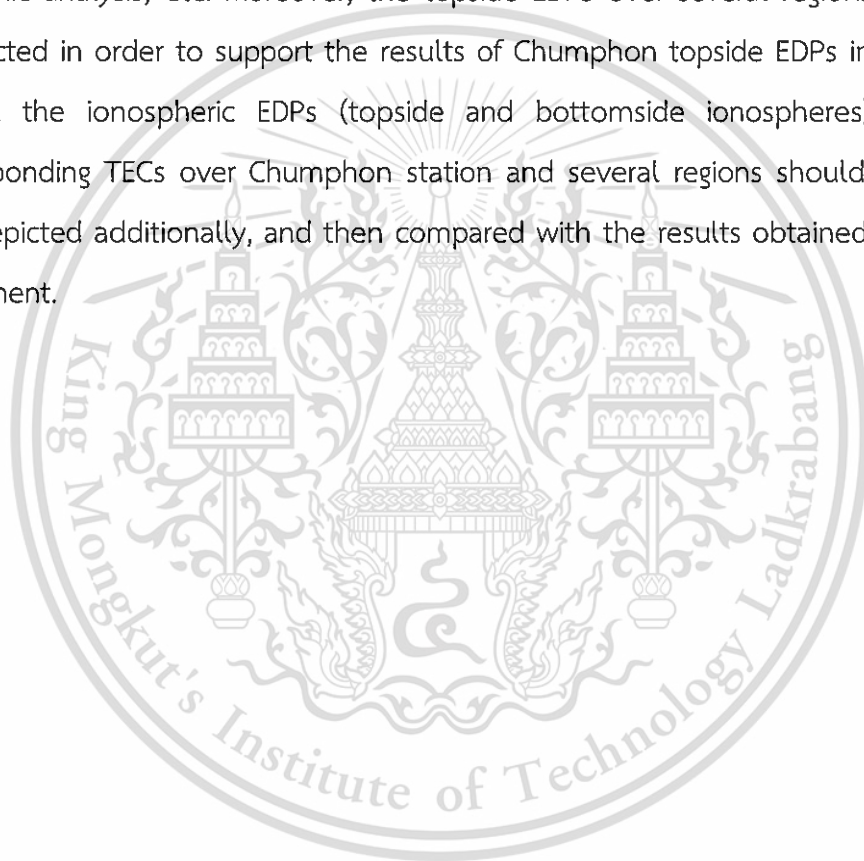
7. For summer season, both the Δ_{IGS} and Δ_{IRI} values are lower than about 4 ns during daytime and nighttime.

This material is reserved for educational use only, not allowed for commercial use.

Forbidden to modify the content, and cite the document when use.

7.2 Suggestions for future works

Although a new proposed B2bot (B2bot_Pro) show the same trends to the observed B0 of digisonde compared with the IRI-predicted B0 values and the original B2bot of the NeQuick 2 model (B2bot_NeQ), however, the differences between the B2bot_Pro and the observed B0 exist. Therefore, a correction factor for B2bot_Pro should be figured out so as to make the B2bot_Pro close to this gap. There exist several approaches for computing the correction factor such as using the averages of absolute differences (Jamjareegulgarn et al., 2017), the curve fitting, and the spherical harmonic analysis, etc. Moreover, the topside EDPs over several regions should be conducted in order to support the results of Chumphon topside EDPs in this thesis. Finally, the ionospheric EDPs (topside and bottomside ionospheres) and their corresponding TECs over Chumphon station and several regions should be studied and depicted additionally, and then compared with the results obtained from other equipment.



LIST OF REFERENCES

- Adeniyi, J.O., Radicella, S.M., 1998. "Variation of bottomside profile parameters and B1 at high solar activity for an equatorial station." *J. Atmos. Sol. Terr. Phys.* 60 (11), 1123-1127.
- Altadill, D., Torta, J.M., Blanch, E., 2009. "Proposal of new models of the bottomside B0 and B1 parameters for IRI." *Adv. Space Res.* 43 (11), 1825-1834.
- Bent, R.B., Llewellyn, S.K., Walloch, M.K., 1972. Description and evaluation of the Bent ionospheric model. DBA Systems, Melbourne, Florida, B26740.
- Bilitza, D., 1990. "The International reference ionosphere 1990. National Space Science Data Center." NSSDC/WDC-A-R&S Reports 90-22, Green Belt, Maryland.
- Bilitza, D., 2001. "International reference ionosphere 2000." *Radio Sci.* 36 (2), 261-275.
- Bilitza, D., 2004. A correction for the IRI topside electron density model based on Alouette/ISIS topside sounder data. *Adv. Space Res.* 33, 838-843.
- Bilitza, D., Altadill, D., Zhang, Y., Mertens, C., Truhlik, V., Richards, P., McKinnell, L.A., Reinisch, B.W., 2014. The International Reference Ionosphere 2012—a model of international collaboration. *J. Space Weather Space Clim.* 4 (A07).
- Bilitza, D., Radicella, S.M., Reinisch, B.W., Adeniyi, J.O., Mosert Gonzalez, M.E., Zhang, S.R., Obrou, O., 2000. New B0 and B1 models for IRI. *Adv. Space Res.* 25 (1), 89-95.
- Bilitza, D., Reinisch, B.W., Radicella, S.M., Pulnits, S., Gulyaeva, T., Trisková, L., 2006. Improvements of the International Reference Ionosphere model for the topside electron density profile. *Radio Sci.* 41, RS5S15.
- Bilitza, D., Sheik, N., Eyfrig, R., 1979. A global model for the height of the F2-peak using M3000 values from the CCIR numerical map. *Telecomm. J.* 46, 549-553.
- Blewitt, G., 1990. An automatic editing algorithm for GPS data. *Geophys. Res. Lett.* 17, 199-202.
- Chapman, S., 1931. The absorption and dissociative or ionizing effect of monochromatic radiation in an atmosphere on a rotating earth. *Proc. Phys. Soc.* 43, 26-45.

- Chauhan, V., Singh, O.P., 2010. A morphological study of GPS-TEC data at Agra and the comparison with the IRI model. *Adv. Space Res.* 46, 280-290.
- Chen, H., Liu, L., Wan, W., Ning, B., Lei, J., 2006. A comparative study of the bottomside profile parameters over Wuhan with IRI-2001 for 1999–2004. *Earth Planets Space* 58, 601–605.
- Chuo, Y.J., 2012. Variations of ionospheric profile parameters during solar maximum and comparison with IRI-2007 over Chung-Li, Taiwan. *Ann. Geophys.* 30, 1249-1257.
- Chuo, Y.J., Lee, C.C., Chen, W.S., 2010. Comparison of ionospheric equivalent slab thickness with bottomside digisonde profile over Wuhan. *J. Atmos. Sol. Terr. Phys.* 72, 528-533.
- Chuo, Y.J., 2014. Variations of Scale Height at F-Region Peak Based on Ionosonde Measurements during Solar Maximum over the Crest of Equatorial Ionization Anomaly Region. *Sci. World J.*, 1-9.
- Cooksey D., Understanding the Global Positioning System (GPS). MSU GPS Laboratory, <http://www.montana.edu/gps>.
- Coïsson, P., Nava, B., Radicella, S.M., 2009. On the use of NeQuick topside option in IRI-2007. *Adv. Space Res.* 43, 1688-1693.
- Coïsson, P., Nava, B., Radicella, S.M., Oladipo, O.A., Adeniyi, J.O., Gopi Krishna, Rama Rao, P.V.S., Ravindran, S., 2008. NeQuick bottomside analysis at low latitudes. *J. Atmos. Sol. Terr. Phys.* 70, 1911-1918.
- Coïsson, P., Radicella, S.M., Leitinger, R., Ciraolo, L., 2004. Are models predicting a realistic picture of vertical total electron content? *Radio Sci.* 39, RS1S14.
- Coïsson, P., Radicella, S.M., Leitinger, R., Nava, B., 2006. Topside electron density in IRI and NeQuick: features and limitations. *Adv. Space Res.* 37, 937-942.
- Coïsson, P., Radicella, S.M., Nava, B., Leitinger, R., 2008a. Low and equatorial latitudes topside in NeQuick. *J. Atmos. Sol. Terr. Phys.* 70, 901-906.
- Davies, K., Liu, X.M., 1991. Ionospheric slab thickness in middle and low latitudes. *Radio Sci.* 26 (4), 997–1005.
- Dessler, J.A., Houghton, J.T., Rycroft, M.J., *Cambridge Atmospheric and Space Science Series*. Cambridge University Press, Cambridge, UK, 335–375.

Di Giovanni, G., Radicella, S.M., 1990. An analytical model of the electron density profile in the ionosphere. *Adv. Space Res.* 10 (11), 27-30.

Farley, D.T., Bonelli, E., Fejer, B.G., 1986. The pre-reversal enhancement of the zonal electric field in the equatorial ionosphere. *J. Geophys. Res.* 91, 13723–13728.

Fejer, B.G., De Paula, E.R., Heelis, R.A., Hanson, W.B., 1995. Global equatorial ionosphere vertical plasma drifts measured by the AE-E satellite. *J. Geophys. Res.* 100, 5769-5776.

<ftp://cdis.gsfc.nasa.gov/gps/products/ionex>.

Goodwin, G.L., Silby, J.H., Lynn, K.J.W., Breed, A.M., Essex, E.A., 1995. GPS satellite measurements: ionospheric slab thickness and total electron content. *J. Atmos. Terr. Phys.* 57, 1723–1732.

Gulyaeva, T.L., 1987. Progress in ionospheric information based on electron density profile analysis of ionograms. *Adv. Space Res.* 7 (6), 39-48.

Gulyaeva, T.L., 2007. Variable coupling between the bottomside and topside thickness of the ionosphere. *J. Atmos. Sol. Terr. Phys.* 69 (4-5), 528-536.

Gurtner, W., Beutler, G., Botton, S., Rothacher, M., Geiger, A., Kahle, H.G., Schneider, D., Wiget, A., 1989. The use of the global positioning system in mountainous areas. *Manuscripta Geodaetica.* 14, 53-60.

<http://digisonde.com/>.

<http://igscb.jpl.nasa.gov/igscb/data/format/rinex2.txt>.

http://omniweb.gsfc.nasa.gov/vitmo/iri2012_vitmo.html.

<http://physics.weber.edu/schroeder/ua/sunandseasons.html>.

<http://utd500.utdallas.edu/ionosphere.htm>.

http://wdc.nict.go.jp/IONO/contents/Ionogram_J.html.

<http://www.gps.gov/technical/ps/2008-SPS-performance-standard.pdf>

<http://www.montana.edu/gps/understd.html>.

https://en.wikipedia.org/wiki/Global_Positioning_System.

<https://en.wikipedia.org/wiki/Ionosphere>.

<https://www.slideshare.net/wasim1akram000/>.

International Telecommunication Union. 1966. **CCIR: Comité Consultatif International des Radio Communications**. Reports, 340-1 and 340-6, Geneva, Switzerland.

This material is reserved for educational use only, not allowed for commercial use.

Forbidden to modify the content, and cite the document when use.

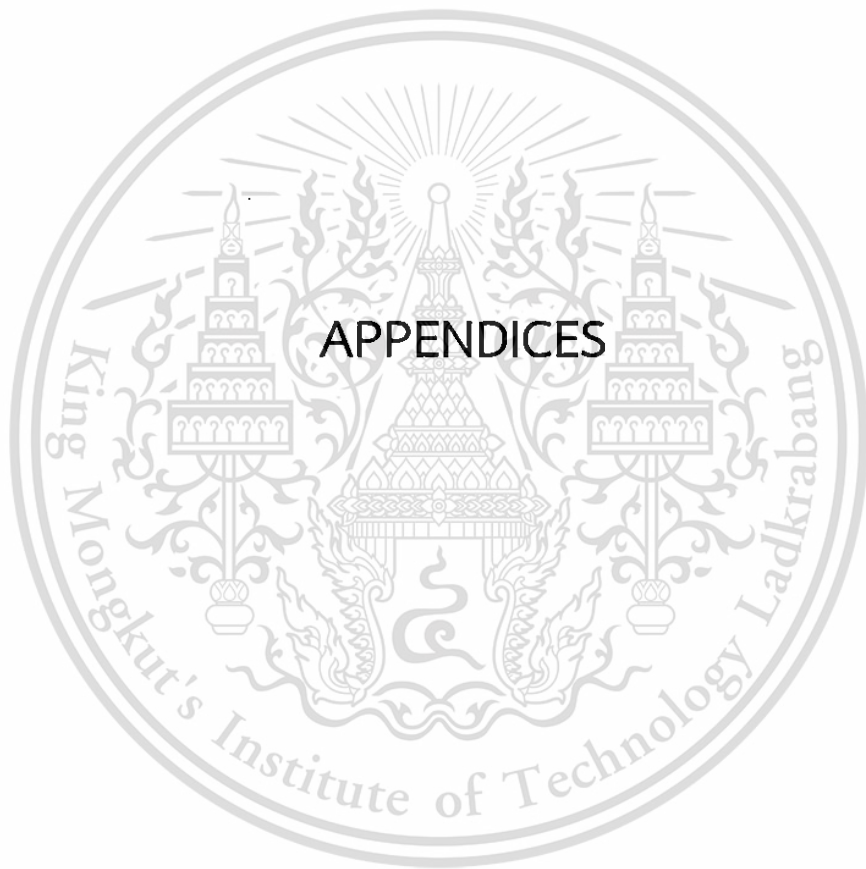
- Hochegger, G., Nava, B., Radicella, S.M., Leitinger, R., 2000. **A family of ionospheric models for different uses.** *Physics and Chemistry of the Earth, Part C: Solar, Terrestrial & Planetary Science* 25 (4), 307-310.
- Huang, X., Reinisch, B.W., 1996. **Vertical electron density profiles from Digisonde ionograms: The average representative profile.** *Annali di Geofisica* XXXIX (4), 751–756.
- Huang, X., Reinisch, B.W., 2001. **Vertical electron content from ionograms in Real Time.** *Radio Sci.* 36 (2), 335–342.
- Jamjareegulgarn, P., Supnithi, P., Hozumi, K., Tsugawa, T., 2017. **A correction factor of Bottomside Thickness Parameter for Computing TEC in Global Navigation Satellite Systems.** *iEECON 2017*, 8-10 March, Pattaya, Thailand.
- Jamjareegulgarn, P., Supnithi, P., Ishii, M., Maruyama, T., Wichaipanich, N., 2015. **A comparative study of ionospheric profile parameters B0 and B1 over Chumphon with IRI-2012.** *ECTI-CON 2015*, 24-27 June, Hua-Hin, Thailand.
- Kakinami, Y., Chen, C.H., Liu, J.Y., Oyama, K.I., Yang, W.H., Abe, S., 2009. **Empirical models of Total Electron Content based on functional fitting over Taiwan during geomagnetic quiet condition.** *Ann. Geophys.* 27, 3321–3333.
- Kenpankho, P., Supnithi, P., Tsugawa, T., Maruyama, T., 2011. **Variation of ionospheric slab thickness observations at Chumphon equatorial magnetic location.** *Earth Planets Space* 63, 359-364.
- Kenro, N., 2009. **FMCW ionosonde for the SEALION project.** *Journal of the National Institute of Information and Communications Technology* 56 (1-4).
- Kumar, S., Tan, E.L., Razul, S.G., See, C.M.S., Siingh, D., 2014. **Validation of the IRI-2012 model with GPS-based ground observation over a low-latitude Singapore station.** *Earth, Planets and Space* 66 (17), 1-10.
- Kutiev, I., Marinov, P., 2007. **Topside sounder model of scale height and transition height characteristics of the ionosphere.** *Adv. Space Res.* 39, 759-766.
- Kutiev, I., Marinov, P., Belehaki, A., Reinisch, B.W., Jakowski, N., 2009. **Reconstruction of topside density profile by using the topside sounder model profiler and digisonde data.** *Adv. Space Res.* 43, 1683–1687.

- Lee, C.C., Reinisch, B.W., 2007. Quiet-condition variations in the scale height at the F2-layer peak at Jicamarca during solar minimum and maximum. *Ann. Geophys.* 25 (12), 2541–2550.
- Lee, C.C., Reinisch, B.W., Su, S.Y., Chen, W.S., 2008. Quiet-time variations of F2-layer parameters at Jicamarca and comparison with IRI-2001 during solar minimum. *J. Atmos. Sol. Terr. Phys.* 70, 184-192.
- Lei, J., Liu, L., Wan, W., Zhang, S.R., Holt, J.M., 2004. A statistical study of ionospheric profile parameters derived from Millstone Hill incoherent scatter radar measurements. *Geophys. Res. Lett.* 31, L14804.
- Liu, J.Y., Tsai, H.F., Wu, C.C., Tseng, C.L., Tsai, L.C., Tsai, W.H., Liou, K., Chao, J.K., 1999. The effect of geomagnetic storm on ionospheric total electron content at the equatorial anomaly region. *Adv. Space Res.* 24 (11), 1491-1494.
- Liu, L., Wan, W., Ning, B., 2006. A study of the ionogram derived effective scale height around the ionospheric hmF2. *Ann. Geophys.* 24 (3), 851–860.
- Lowe S. and ÓLaighin, G., 2013. Monitoring human health behaviour in one's living environment: A technological review. *Medical Engineering & Physics* 36 (2).
- Ma, G., Maruyama, T., 2003. Derivation of TEC and estimation of instrumental biases from GEONET in Japan. *Ann. Geophys.* 21, 2083-2093.
- Maruyama, T., 2010. Ionosphere study. Science of space Environment course, KMITL, Thailand.
- Maruyama, T., 2012. Ionospheric Space Weather and its Effect on Radio Systems. The 1st AOSWA Workshop, Chiang Mai 22-24 February 2012.
- Maruyama, T., Kawamura, M., Saito, S., Nozaki, K., Kato, H., Hemmakorn, N., Boonchuk, T., Komolmis, T., Ha Duyen, C., 2007. Low latitude ionosphere-thermosphere dynamics studies with ionosonde chain in Southeast Asia. *Ann. Geophys.* 25, 1569-1577.
- Mosert, M., Buresova, D., Magdaleno, S., de la Morena, B., Altadill, D., Ezquer, R.G., Scida, L., 2012. An analysis of the scale height at the F2-layer peak over three middle-latitude stations in the European sector. *Earth Planets Space* 64, 493–503.
- Mosert de Gonzalez, M., Radicella, S.M., 1990. On a characteristic point at the base of F2 layer in the ionosphere. *Adv. Space Res.* 10 (11), 17-20.

- Murthy, B.V.K., Hari, S.S., Somayajulu, V.V., 1990. Nighttime equatorial thermospheric meridional winds from ionospheric $h' F$ data. *J. Geophys. Res.* 95 (A4), 4307–4310.
- Nambala, F., McKinnell, L.A., Oyeyemi, E., 2008. Variations in the ionospheric scale height parameter at the F2 peak over Grahamstown, South Africa. *Adv. Space Res.* 42 (4), 707–711.
- Nakamura, M., 2003. Quick reference of manual scaling for special scaling from manual of ionogram scaling. Communications Research Laboratory. Tokyo, Japan.
- Nava, B., Coïsson, P., Radicella, S.M., 2008. A new version of the NeQuick ionosphere electron density model. *J. Atmos. Sol. Terr. Phys.* 70, 1856-1862.
- Oryema, B., Jurua, E., D'ujanga, F.M., Ssebiyonga, N. 2015. Investigation of TEC variations over the magnetic equatorial and equatorial anomaly regions of the African sector. *Adv. Space Res.* 56 (9), 1939–1950.
- Pandey, V.K., Sethi, N.K., 1996. Comparison of hmF2 and ionospheric bottomside electron density profile obtained from IRI and incoherent scatter measurements. *Adv. Space Res.* 18 (6), 33–37.
- Prölss, G.W., 1987. Storm-induced changes in the thermospheric composition at middle latitudes. *Planet Space Sci.* 35 (6), 807–811.
- Radicella, S.M., Leitinger, R., 2001. The evolution of the DGR approach to model electron density profiles. *Adv. Space Res.* 27 (1). 35-40.
- Radicella, S.M., Zhang, M.L., 1995. The improved DGR analytical model of electron density height profile and total electron content in the ionosphere. *Annali di Geofisica XXXVIII* (1), 35-41.
- Ramakrishnan, S., Rawer, K., 1972. Model electron density profiles obtained by empirical procedures. *Space Res. XII. Akademie-Verlag, Berlin*, 1253-1261.
- Rathore, V.S., Kumar, S., Singh, A.K., 2015. A statistical comparison of IRI TEC prediction with GPS TEC measurement over Varanasi, India. *J. Atmos. Terr. Phys.* 124, 1-9.
- Rawer, K., 1982. Replacement of the present sub-peak plasma density profile by a unique expression. *Adv. Space Res.* 2 (10). 183-190.
- Rawer, K., Bilitza, D., Ramakrishnan, S., Sheikh, N., 1978. Intentions and build-up of the International Reference Ionosphere, in *Operational Modeling of the Aerospace Propagation Environment. AGARD Conf. Proc.*, 238, 6.1-6.9.

- Rawer, K., Lincoln, J., Conkright, R., 1978. *International Reference Ionosphere*. URSI, Brussels.
- Reinisch, B.W., 2004. Tenth International Digisonde Training Seminar at UMass Lowell reviews state of real time mapping of the ionosphere. *IEEE Antennas Propag. Mag.* 45 (5), 110-117.
- Reinisch, B.W., Huang, X.Q., Belehaki, A., Shi, J.K., Zhang, M.L., Ilma, R., 2004a. Modeling the IRI topside profile using scale heights from ground-based ionosonde measurements. *Adv. Space Res.* 34, 2026-2031.
- Reinisch, B.W., Nsumei, P., Huang, X., Song, P., Tu, J., 2004b. Connecting the IMAGE/RPI plasmasphere profile to the IRI ionosphere profile, Stanford Univ., 9-10 December, 2004.
- Rishbeth, H.T., Fuller-Rowell, T.J., Rees, D., 1987. Diffusive equilibrium and vertical motion in the thermosphere during a severe magnetic storm: a computational study. *Planet. Space Sci.* 35, 1157-1165.
- Rishbeth, H., Ganguly, S., and Walker, J.C.G., 1978. Field-aligned and field-perpendicular velocities in the ionospheric F2-layer. *J. Atmos. Terr. Phys.* 40, 767-784.
- Rush, C., Fox, M., Bilitza, D., Davies, K., Mcnamara, L., Stewart, F., Pokempner, M., 1989. Ionospheric mapping-an update of foF2 coefficients. *Telecomm. J.* 56, 179-182.
- Sajedi, S.A. and Abdollahi, F., 2012. Geomagnetic disturbances may be environmental risk factor for multiple sclerosis: An ecological study of 111 locations in 24 countries, *BMC Neurology*, 12 (100).
- Schunk, R.W., Nagy, A.F., 2000. In *Ionospheres: Physics, Plasma Physics, and Chemistry*.
- Sethi, N.K., Mahajan, K.K., 2002. The bottomside parameters B0, B1 obtained from incoherent scatter measurements during a solar maximum and their comparisons with the IRI-2001 model. *Ann. Geophys.* 20, 817-822.
- Stankov, S.M., Jakowski, N., Heise, S., Muhtarov, P., Kutiev, I., Warnant, R., 2003. A new method for reconstruction of the vertical electron density distribution in the upper ionosphere and plasmasphere. *J. Geophys. Res.* 108 (A5), 1164.
- Stankov, S.M., Stegen, K., Muhtarov, P., Warnant, R., 2011. Local ionospheric electron density profile reconstruction in real time from simultaneous ground-based GNSS and ionosonde measurements. *Adv. Space Res.* 47, 1172-1180.

- Titheridge, J. E., 1985. Ionogram analysis with the generalised program POLAN. Report UAG-93, University of Auckland, New Zealand.
- Trisková, L., Truhlik, V., Smilauer, J., 2006. An empirical topside electron density model for calculation of absolute ion densities in IRI. *Adv. Space Res.* 37 (5), 928-934.
- Tulasi Ram, S., Su, S.Y., Liu, C.H., Reinisch, B.W., McKinnell, L.A., 2009. Topside ionospheric effective scale heights (HT) derived with ROCSAT-1 and ground-based ionosonde observations at equatorial and midlatitude stations. *J. Geophys. Res.* 114 (A10309), doi:10.1029/2009JA014485.
- Verhulst, T., Stankov, S.M., 2014. Evaluation of ionospheric profilers using topside sounding data. *Radio Sci.* 49 (3), 181-195.
- Verhulst, T., Stankov, S.M., 2015. Ionospheric specification with analytical profilers: Evidences of non-Chapman electron density distribution in the upper ionosphere. *Adv. Space Res.* 55, 2058-2069.
- Wakai, N., Ohyaama, H., Koizumi, T., 1987. Example of typical ionogram. Manual of Ionogram Scaling, Third Version.
- Wang, S.G., Shi, J.K., Wang, X., Wang, G.J., 2010. Validation of B2bot in the NeQuick model during High solar activity at Hainan station. *Adv. Space Res.* 46, 1094-1101.
- Yonezawa, T., 1966. Theory of formation of the ionosphere. *Space Sci. Rev.* 5, 3-56.
- Zhang, M.L., Radicella, S.M., Spalla, P., 1991. The use of simultaneous observations of TEC and ground vertical ionospheric soundings to improve the modeling of the ionosphere. IRI Workshop, Athens, Greece.
- Zhang, M.L., Reinisch, B.W., Shi, J.K., Wu, S.Z., Wang, X., 2006. Diurnal and seasonal variation of the ionogram-derived scale height at the F2 peak. *Adv. Space Res.*, 37, 967-971.
- Zhang, M.L., Wan, W., Liu, L., Shi, J.K., 2008. Variability of the behavior of the bottomside (B0, B1) parameters obtained from the ground-based ionograms at China's low latitude station. *Adv. Space Res.* 42, 695-702.



This material is reserved for educational use only, not allowed for commercial use.

Forbidden to modify the content, and cite the document when use.

APPENDIX A

LIST OF PUBLICATIONS

Journal

1. Jamjareegulgarn, P., Supnithi, P., Watthanasangmechai, K., Yokoyama, T., Tsugawa, T., Ishii, M., 2016. A new expression for computing the bottomside thickness parameter and comparisons with the NeQuick and IRI-2012 models during declining phase of solar cycle 23 at equatorial latitude station, Chumphon, Thailand. *Adv. Space Res.* doi: <http://dx.doi.org/10.1016/j.asr.2016.11.003>.
2. Jamjareegulgarn, P., Supnithi, P., Hozumi, K., Tsugawa, T., 2017. Study of ionospheric topside variations based on NeQuick topside formulation and comparisons with the IRI-2012 model at equatorial latitude station, Chumphon, Thailand. *Adv. Space Res.* doi: <http://dx.doi.org/10.1016/j.asr.2017.03.025>.

Conference Proceedings

1. Jamjareegulgarn, P., Supnithi, P., Wichaipanich, N., Ishii, M., Maruyama, T., 2015. A comparative study of ionospheric profile parameters B0 and B1 over Chumphon with IRI-2012. The 12th International Conference on Electrical Engineering/Electronics, Computer, Telecommunications and Information Technology (ECTI-CON 2015), 24-27 June, 2015, Hua-Hin, Thailand.
2. Jamjareegulgarn, P., Supnithi, P., Watthanasangmechai, K., Yokoyama, T., Tsugawa, T., Ishii, M., Nayak, C., 2016. Variations of ionospheric slab thickness over the magnetic equator of Southeast Asia. The 13th International Conference on Electrical Engineering/Electronics, Computer, Telecommunications and Information Technology (ECTI-CON 2016), 28 June-1 July, 2016, Chiang Mai, Thailand.

AUTHOR BIOGRAPHY

Author: Mr. Punyawit Jamjareegulgarn
Date of Birth: November 29th, 1973
Place of Birth: Bangkok
Bachelor Degree: B. Eng.
Department: Telecommunication Engineering
Faculty of Engineering
King Mongkut's Institute of Technology Ladkrabang (KMITL)
Year of Graduation: 1995
Master Degree: M. Eng.
Department: Electrical Engineering (Major: Telecommunication System)
Faculty of Engineering
King Mongkut's Institute of Technology Ladkrabang (KMITL)
Year of Graduation: 1998
Research Interests: Ionospheric monitoring and prediction, embedded systems.

Related Publications/Conferences:

1. Jamjareegulgarn, P., Supnithi, P., Wichaipanich, N., Ishii, M., Maruyama, T., 2015. A comparative study of ionospheric profile parameters B0 and B1 over Chumphon with IRI-2012. The 12th International Conference on Electrical Engineering/Electronics, Computer, Telecommunications and Information Technology (ECTI-CON 2015), 24-27 June, 2015, Hua-Hin, Thailand.
2. Jamjareegulgarn, P., Supnithi, P., Watthanasangmechai, K., Yokoyama, T., Tsugawa, T., Ishii, M., Nayak, C., 2016. Variations of ionospheric slab thickness over the magnetic equator of Southeast Asia. The 13th International Conference on Electrical Engineering/Electronics, Computer, Telecommunications and Information Technology (ECTI-CON 2016), 28 June-1 July, 2016, Chiang Mai, Thailand.

3. Nayak, C., Tsai, L., Su, S., Galkin, I., Tan, A., Nofri, E., Jamjareegulgarn, P., 2016. Peculiar features of the low-latitude and midlatitude ionospheric response to the St. Patrick's Day geomagnetic storm of 17 March 2015. *Journal of Geophysical Research: Space Physics*. 121 (8), 7941–7960. doi: 10.1002/2016JA022489.
4. Jamjareegulgarn, P., P., Supnithi, P., Watthanasangmechai, K., Yokoyama, T., Tsugawa, T., Ishii, M., 2016. A new expression for computing the bottomside thickness parameter and comparisons with the NeQuick and IRI-2012 models during declining phase of solar cycle 23 at equatorial latitude station, Chumphon, Thailand. *Adv. Space Res.* doi: <http://dx.doi.org/10.1016/j.asr.2016.11.003>.
5. Jamjareegulgarn, P., Supnithi, P., Hozumi, K., Tsugawa, T., 2017. Study of ionospheric topside variations based on NeQuick topside formulation and comparisons with the IRI-2012 model at equatorial latitude station, Chumphon, Thailand. *Adv. Space Res.* doi: <http://dx.doi.org/10.1016/j.asr.2017.03.025>.
6. Jamjareegulgarn, P., Supnithi, P., Hozumi, K., Tsugawa, T., 2017. A correction factor of Bottomside Thickness Parameter for Computing TEC in Global Navigation Satellite Systems. The 2017 International Electrical Engineering Congress (iEECON 2017), 8-10 March, 2017, Pattaya, Thailand.
7. Jamjareegulgarn, P., Supnithi, P., Hozumi, K., Tsugawa, T., 2017. A New Expression for Computing Topside Scale Height for Satellite-Based Communications. The 2017 International Electrical Engineering Congress (iEECON 2017), 8-10 March, 2017, Pattaya, Thailand.